Habitable Environments in Late Stellar Evolution

Conditions for Abiogenesis in the Planetary Systems of White Dwarfs

Author: **Dewy Peters**
Supervisor: **Prof. dr. F.F.S. van der Tak**

A thesis submitted in fulfillment of the requirements for the degree BSc in Astronomy

Faculty of Science and Engineering
University of Groningen
The Netherlands
March 2021

Abstract

With very high potential transit-depths and an absence of stellar flare activity, the planets of White Dwarfs (WDs) are some of the most promising in the search for detectable life. Whilst planets with Earth-like masses and radii have yet to be detected around WDs, there is considerable evidence from spectroscopic and photometric observations that both terrestrial and gas-giant planets are capable of surviving post-main sequence evolution and migrating into the WD phase. WDs are also capable of hosting stable Habitable Zones outside orbital distances at which Earth-mass planets would be disintegrated by tidal forces. Whilst transitioning to the WD Phase, a main-sequence star has to progress along the Asymptotic Giant Branch (AGB), whereby orbiting planets would be subjected to atmospheric erosion by its harsh stellar winds. As a trade-off, the Circumstellar Envelope (CSE) of an AGB star is found to be rich in organics and some of the simple molecules from which more complex prebiotic molecules such as amino acids and simple sugars can be synthesised. It is found that planets with initial orbital distances equivalent to those of Saturn and the Kuiper Belt would be capable of accreting a mass between 1 and 20 times that of the Earth's atmosphere from the CSE and as a result, could obtain much of the material necessary to sustain life after the AGB and also experience minimal atmospheric erosion. However, the orbital distance evolution of these planets also presents an obstacle to their habitability in that they would have to migrate from $\sim 100\,\mathrm{AU}$ to $\sim 0.01\,\mathrm{AU}$ to dignify their prebiotic chemistries with the warmer conditions necessary to sustain life at stable WD HZs. In this regard, more work is required to model extreme inward orbital migration or the accretion of a secondary or tertiary atmosphere from the CSE of an AGB star.

Contents

1. Introduction

Since the discovery of a planet orbiting the Main Sequence (MS) star 51-Pegasi (Mayor & Queloz 1995), exoplanetology has very rapidly grown as a sub-field of astronomy and in part has been driven by the search for extraterrestrial life. As of the 17th of February 2021, 4341 exoplanets have been confirmed (Akeson et al. 2013; NASA 2021), and it has become increasingly evident that Earth is by no means unique in being a terrestrial planet (see Fig. 1). It has also become increasingly clear that Earth is by no means unique in occupying the Habitable Zone (HZ) of its host star (eg. Anglada-Escudé et al. (2016)): that is, the distance at which a planet is able to sustain liquid water on its surface[1] given sufficient atmospheric pressure (Kasting et al. 1993). Interestingly, evidence for exoplanets orbiting stellar remnants predates that of MS stars: Wolszczan & Frail (1992) confirmed two planets orbiting the pulsar PSR 1257+12 and observational evidence for a planet(esimal) having been accreted onto the photosphere of a White Dwarf (WD) was recorded as far back as 1917. The planets of stellar remnants have seldom been targets in the search for habitable worlds, owing to former-HZ planets being engulfed in late stellar evolution or subjected to harsh radiation fields (Villaver & Livio 2007). In spite of this, recent theoretical work has suggested that if the planets of WD undergo tidal migration, they may indeed be capable of sustaining life (Kaltenegger et al. 2020). The first transit detection of a giant intact[2] planet (WD 1856b) orbiting a WD has also demonstrated that planetary migration is possible beyond the MS (Vanderburg et al. 2020).

The appeal of habitable WD planets is rooted in their very high potential transit depths. These would be conducive to the in-depth scrutiny of their atmospheric constituents including possible biosignatures (Agol 2011; Loeb & Maoz 2013; Kaltenegger et al. 2020). Since WDs are expected to be the evolutionary end-point for 97% of stars in the Milky Way (Fontaine et al. 2001), studying their planets also allows us to infer the future of the vast majority of planetary systems, including the Solar System. However, the lowest mass progenitors (with spectral classes K and M) both have lifetimes greater than the current age of the Universe. Higher mass progenitors which have bequeathed their remnant cores as WDs ($0.68\,M_\odot < M < 8\,M_\odot$ (Dobbie et al. 2006)) have likely all done so by shedding their circumstellar envelopes on the Asymptotic Giant Branch (AGB): that is the phase of stellar evolution whereby a MS star has already become a red giant, reached its maximum luminosity and is losing a considerable amount of mass ($\sim\ 10^{-8} - 10^{-5}\,M_\odot\,\mathrm{yr}^{-1}$). The mass that is lost forms a Circumstellar Envelope (CSE), capable of exhibiting diverse chemistries including molecules comprised of the six main atomic constituents of life: carbon, hydrogen, nitrogen, oxygen, phosphorous and sulphur (Schmidt & Ziurys 2016, 2019). This is in part due to the lower temperatures and pressures found in the outer regions of CSEs, permitting the condensation of carbonaceous dust and the synthesis of organic molecules seeded by carbon

atoms fused in and convected from the the interiors of the AGB stars (Habing & Olofsson 2013). Juxtaposing this biologically relevant molecular diversity with the prospect of WDs facilitating habitable planetary environments warrants an investigation into whether life could evolve on the planet of a WD and how it could do so.

In light of the points discussed above, the central objective of this thesis is to determine the extent to which carbon-based life is likely to arise on the planet of a WD from material contained within the circumstellar envelope of its AGB progenitor through the PN phase. In order to do so, Section 2 examines the demographics of WDs and current constraints on the compositions of their planets; Section 3 then investigates the whether WDs are capable of exhibiting continuous habitable zones beyond the orbital distances at which an Earth-like planet would be destroyed by tidal forces; Section 4 probes the prebiotic molecular content of Circumstellar Envelopes (CSEs) and Section 5 treats both how the molecules found in CSEs could be used in synthesising those uniquely found in living organisms and how this material could be delivered to a nearby planet surviving through to the WD phase. Bringing findings from all these disparate investigations together, in Section 7, a conclusion is sought on the likelihood of life arising on a WD planet and what constraints it would be subjected to. Finally, the implications of these findings and possible improvements are discussed in Section 6.
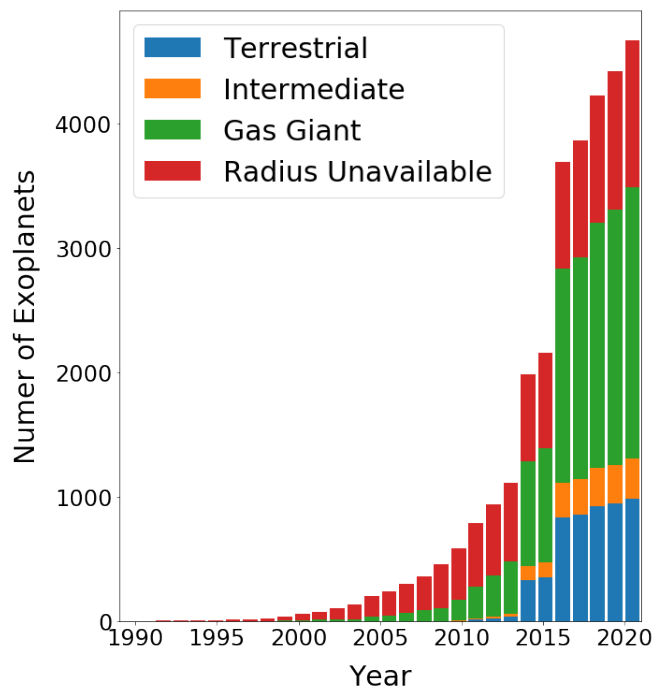
Fig. 1. The cumulative number of exoplanets found each year since 1989. Here, the planets types are distinguished according to their radii: that is, Gas Giants with $R > 2\,\mathrm{R}_\oplus$ and Terrestrial planets with $R < 1.7\,\mathrm{R}_\oplus$ (Lee & Connors 2021).

---

[1]Sub-surface oceans such as those thought to be present on Europa will not be considered in this thesis.

[2]Earlier transits were consistent with planetary debris as opposed to fully intact planets (Vanderburg et al. 2015).

2. The Planets of White Dwarfs

Given that a habitable planet is widely deemed to be a prerequisite for the occurrence of life, this section discusses White Dwarf (WD) planets and what is or can be known about them. Specifically, Section 2.1 describes the three main lines of evidence for WD planets; Section 2.2 treats the implications of WD demographics on their planetary environments and Section 2.3 investigates the metallicities and abundances of elements within polluted WDs, to facilitate a comparison with those of objects found in the Solar System: the only planetary system currently known to host life. The eventual goal of Section 2 is therefore to infer how comparable the planetary systems of WDs are to the Solar System and whether in terms of the elements present, they may be conducive to hosting terrestrial planets which life needs to evolve.

Before proceeding to discussion of WD planets, the basic observational and theoretical properties of WDs need to be established. The properties of WD planets and those of Main-Sequence (MS) stars may be confused. Therefore, it is important to discuss the basis of they differ observationally and theoretically. WDs have been observed at least since the discovery of 40 Eridani B by William Herschel in 1783, published in 1785. They can be identified by a comparison of their colour and intrinsic luminosity on a Hertzsprung-Russell diagram, wherein they are typically plotted below and to the left of the MS. Specifically, WDs have a low intrinsic luminosity (absolute magnitude, $10 \lesssim M_v \lesssim 15$), with respect to their B-V Colour index, generally varying between 0 and +1.5 depending on the WD's Cooling Age (time elapsed since becoming a WD). These low luminosities ($\sim 10^{-4} \, \mathrm{L_\odot}$) are a consequence of WDs having very small radii ($\sim 0.013 \, \mathrm{R_\odot}$) compared to MS stars (Gaia Collaboration et al. 2018). Since WDs are the remnant degenerate cores of MS stars, they are not powered by nucleosynthesis; rather, they radiate the residual energy generated by that of their progenitors and cool exponentially with time. As a result, their Spectral Energy Distributions (SEDs) are redshifted with age. As not enough time has elapsed since the first $M \lesssim 8 \, \mathrm{M_\odot}$ stars shed their mass envelopes, the coolest WDs have $T_{\mathrm{eff}} \sim 3000 \, \mathrm{K}$ and Cooling Ages, $\sim 10 \, \mathrm{Gyr}$ (Kaplan et al. 2014). Their core compositions reflect the products of the final nuclear fusion reactions in the central cores of their progenitors: helium for the lowest masses (Liebert et al. 2004), and oxygen-neon[3] for the highest ones (Werner et al. 2004). Their photospheric compositions, however, are dominated either by hydrogen or helium. This is owing to their high surface gravities which stratify elements by mass so that usually only the lightest can be observed. The masses of WDs are limited by the Chandrasekhar Limit ($M_{\mathrm{WD}} \lesssim 1.44 \, \mathrm{M_\odot}$), beyond which their characteristic electron degeneracy pressure can be overcome by self-gravity. This facilitates further collapse into a neutron star or a black hole if the Tolman-Oppenheimer-Volkoff Limit is exceeded. Now that the fundamental theoretical and observational properties of WDs have been established, the evidence for and properties of their planets can be explored.

---

[3]This is because oxygen is formed when carbon-12 fuses with helium-4, and neon is formed when carbon-12 fuses with another carbon-12 nucleus.

2.1. Evidence for Planets

At the time of writing[4], there are three main lines of evidence for WDs hosting planets. These are WD pollution: the presence of metallic spectral lines in the otherwise hydrogen or helium-dominated photospheres of WDs, treated in Section 2.1.1; infrared excesses corresponding to circumstellar disks forming as a result of the tidal disintegration of planetesimals closely orbiting WDs, treated in Section 2.1.2 and most recently, the transit detection of planetesimals in the process of tidal destruction and that of a giant planet orbiting WD 1856+324, both treated in Section 2.1.3. Although theoretically other detection methods such as direct imaging may be used to detect planets around WDs (Burleigh et al. 2005), they will not be treated here as to date, they have not provided any information on the nature of WD planetary systems. The lines of evidence for WD planets will be reviewed in this section because an understanding of them and how they differ from those for planets around main-sequence stars is necessary for any analysis of the nature of WD planetary systems.

2.1.1. White Dwarf Pollution

Polluted WDs are those with metallic spectral features in their atmospheres. They are indicated by a 'Z' in their spectral classification, following 'D' indicating degeneracy (ie. that the object is a WD) and often either an 'A', indicating their dominant constituent being H, or a B, indicating their dominant constituent being He (McCook & Sion 1999). For instance, a He dominated WD with metallic absorption lines would have the spectral classification 'DBZ'. The metallic absorption features can be relatively easy to identify and emanate from the accretion of planetary debris. Consequently, most of what is currently known about the bulk compositions of planet(esimals) around WDs has been inferred from the spectral features in polluted WDs. Therefore, it is important to explain how this phenomenon is of planetary origin before the compositions of WD planetary systems are inferred in Section 2.3. Because the observation of WD pollution has a long history dating back to 1917, this section will present the evidence for its planetary origin by sequentially describing how such a consensus emerged over the last century.

In 1917, a WD was falsely identified as an F0 star. This was owing to prominent Ca II H and K spectral features in the atmosphere of Van Maanen 2 (vMa 2). In the subsequent decades, significant observational advancements were made made in determining the distinct compact nature of WDs, and significant theoretical advancements were made in identifying them as stellar remnants composed of degenerate matter. By 1949, vMa 2 was understood to be a WD. However, it also became clear that WDs in general had low metallicities, several orders of magnitude below that of the Sun, (Wegner 1972; Wehrse 1975) and that apart from the prominent Ca II lines, this also applied for vMa 2 (Weidemann 1960). Thus, the metallic spectral features found in some WDs had to be reconciled with the emerging consensus of WDs being metal-poor objects.

---

[4]27th of February 2021

Early explanations of metallic absorption lines in WD spectra referred to the short sedimentation timescales of their concomitant atomic species and attributed their absence in most other WDs to mechanisms such as convection, and removal via molecule formation (Weidemann 1960). By 1979, these mechanisms were demonstrated unlikely (Vauclair et al. 1979), and a consensus began to emerge that the material must have been accreted from the Interstellar Medium (ISM) (Farihi 2016). However, that too fell out of favour and was debunked by 2010 wherein the abundances of 146 polluted WDs were found to be incongruent with those of their local ISM (Farihi et al. 2010). Instead, it is now widely accepted that these features emanate from accreted circumstellar material (Stone et al. 2015; Farihi et al. 2010).

The main reason for these metallic absorption lines being extrinsic in the context of WDs is that for $T_{\mathrm{eff}} < 25\,000\,\mathrm{K}$, elements heavier than He are expected to sink (Chayer et al. 1995; Barstow et al. 2014). For example, $^{40}\mathrm{Ca}$ is predicted to take $\tau_{\mathrm{diff}} \approx 1000\,\mathrm{yr}$ to diffuse at $T_{\mathrm{eff}} = 8000\,\mathrm{K}$ and for typically younger WDs at $T_{\mathrm{eff}} = 20\,000\,\mathrm{K}$, this timescale is as short as $\approx 1.48\,\mathrm{d}$ (See Table 2, Bauer & Bildsten (2019)). Therefore, the metallic spectral features recorded in 1917 must have had a planetary origin: unbeknownst evidence for a planetary system predating the first exoplanet discoveries of Campbell et al. (1988), (confirmed Hatzes et al. (2003)), Wolszczan & Frail (1992) and Mayor & Queloz (1995) by approximately 70 years.

2.1.2. Circumstellar Disks

Before the remains of a planet(esimal) are accreted onto a WD and give rise to pollution, the planet(esimal) drifts within its Roche Limit (RL) with respect to the WD: the distance it has to be from the WD in order for tidal forces to overcome its self-gravity. After the tidal forces dismember the planet(esimal), it forms a circumstellar disk. The particulate matter (dust) comprising this disk is heated by radiation from the WD, thereby giving rise to an infrared excess that can be identified in its spectrum. The coincidence of an infrared excess with metallic absorption lines, notably in GD 362 and G29-38 helped cement the emerging consensus on the planetary origin of WD pollution and introduced a new method of probing the presence and composition of WD planets (Farihi 2011). Thus the discussion of this detection method mainly serves the purpose of corroborating and providing more context to that discussed in Section 2.1.1. In addition, it will bridge the gap to Section 2.1.3 in that circumstellar disks, like transiting planet(esimal)s are exterior to WDs as opposed to within their photospheres.

The Asteroid Accretion Model is currently the favoured mechanism for explaining the infrared excess. Specifically, this posits that tidally disrupted asteroids are the principal progenitors for infrared excesses and by extension, the main source of pollutants in WDs (Farihi 2011). Asteroids are favoured over comets due to the very short metal diffusion timescales: in cases such as EG 102, on-going accretion would be necessary to explain the presence of heavy metals in its spectra (Holberg et al. 1997). Comets (as well as ISM material) typically exhibit hydrocarbon features and their

dearth in the spectra of polluted WDs also disfavours these other sources of accreted matter (Farihi et al. 2008; Farihi 2011). The negative correlation of infrared excess frequency with cooling age (Farihi et al. 2009), and higher metal accretion rates for hotter WDs (Zuckerman et al. 2010), reinforce the asteroid model. The post-MS evolution and mass loss of the WD's progenitor eventuate in dynamical perturbations of its planetary system (Debes & Sigurdsson 2002). Therefore, the tidal disruption of planetesimals within the RL is expected to occur more frequently for younger, hotter WDs. Finally, it should be noted that the alternative possibility of infrared excesses arising from unresolved brown dwarfs was discounted early on in this sub-field: Becklin et al. (2005) found that for GD 362, the first WDs found to have an infrared excess, the emitting surface area corresponding to the SEDs was too large to be anything other than a disk. This became especially clear with the advent of the *Spitzer Space Telescope* which had a sufficient sensitivity in the mid-infrared to detect such features.

Whilst the majority of circumstellar disks around WDs have been found to be comprised of particulate matter, gaseous debris has also been detected. Unlike dust emission which mainly emanates from the mid-IR, gaseous debris is found to emit in the near-IR; specifically, it is identified by the distinct double-peaked Ca II $850 - 866\,\mathrm{nm}$ triplet (Young et al. 1981; Horne & Marsh 1986). The first such system of this type was SDSS 1228+1040 (Gänsicke et al. 2006). At the time, Gänsicke et al. (2006) argued that this emanated from the sublimation of particulate matter in the accretion disk. However, the same object was later also found to exhibit infrared emission corresponding to a spatially coincident dust disk, indicative of the gas having a collisional origin rather than a sublimational one (Melis et al. 2010). If the gas were sublimated dust, it should have been found closer to the WD, where disk temperatures are higher.

Whilst the detection of gas in circumstellar disks such as those analysed by Melis et al. (2010) is of particulate origin, that recently found around WD J0914+1914 exhibits a very different composition. Specifically, Gänsicke et al. (2019) report the optical and near-IR detection of water (H_2O) and hydrogen sulphide (H_2S) around WD J0914+1914 and argue that the material arises from the accretion of the atmosphere of a giant planet. Unlike all other suspected gaseous debris disks, the Ca II triplet is not found in the spectrum of WD J0914+1914. Instead, its gaseous composition is inferred by the double-peaked Hα and OI ($844.6\,\mathrm{nm}$) emission lines. Unlike those with prevalent WD pollution, the debris is found to be depleted in heavy elements such as iron and the disk is found to extend beyond the canonical RL for terrestrial bodies.

Given that the WD has a high effective temperature of $27\,742\,\mathrm{K}$, the authors propose photo-ionisation driven by intense ultraviolet flux as the key mechanism underlying this gaseous emission. Using the absence of significant radial velocity variations in WD J0914+1914's spectral features [5] and the absence of a characteristic infrared excess, they

---

[5]Relatively speaking, WDs have few spectral features. However, a hydrogen-dominated atmosphere (as in this case) often results in strong Balmer lines. In this specific case, sharp absorption lines of oxygen and sulphur are also present.

rule out a companion with $M \geqslant 30\,\mathrm{M_{Jup}}$ and with it, the possibility of a mass-donating brown dwarf at the inferred orbital distances. However, the liberality of the mass constraint permits the planet to be anything from a Neptune-analogue to a super-Jupiter. In the former case, the authors attribute its orbital position to post-MS planet-planet scattering. In the latter, they propose common envelope evolution as a mechanism. This constitutes the transfer of mass from the WD's progenitor to the giant planet during the former's Asymptotic Giant Branch (AGB) evolution. In this scenario, the WD and giant planet temporarily come to share a common envelope. When this is eventually ejected, the giant planet loses orbital energy and reaches an orbit closer to the WD than would otherwise be expected.

In any case, Gänsicke et al. (2019) are confident that their observations are the result of a gaseous planet. If this is indeed true, it would constitute the earliest published evidence for gas giants in WD planetary systems and the first time the atmosphere of a WD planet has been inferred. Both have implications for the presence of life: the shielding effect of gas giants may be required to ensure safety of habitable planets or moons (Quintana & Barclay 2016; Kohler 2018), whilst atmospheric characterisation is a necessary pre-requisite for detecting biosignatures, which other than advanced technosignatures (Wright et al. 2019), are the only possible way of remotely inferring life beyond the Solar System. Now that tentative evidence has been presented for the presence of gas giants in WD planetary systems, a more direct line of evidence will be discussed: transit photometry.

2.1.3. Transit Photometry

Since 2015, the indirect detections of atmospheric pollutants and circumstellar disks have been augmented by direct transit observations: firstly, the shallow transits of planetary debris around WD 1145+017 (Vanderburg et al. 2015; Xu et al. 2019), and J013906.17+524536.89 (Vanderbosch et al. 2020); secondly, the transit of a giant planet candidate around WD 1856+534 (Vanderburg et al. 2020). Short of direct imaging, these discoveries are perhaps the ultimate confirmation that white dwarfs are capable of hosting planetary systems. Moreover, the discovery of the planet orbiting WD 1856+534, known as WD 1856b, inaugurates the detection of intact planets as opposed to their remnants. This is arguably the most important leap when it comes to characterising such systems in light of their similarity to the Solar System wherein gas giants such as Jupiter are present, and also for characterising WD planetary systems in terms habitability as transiting planets present excellent candidates for atmospheric characterisation (and the search for biosignatures) via transit spectroscopy.

The shallow transits of planetary debris are perhaps the final corroboration of the hypothesis that metallic spectral features and infrared excesses in the SEDs of WDs are of planetary origin. This is because WDs 1145+017 and J013906.17+524536.89 both exhibit these qualities in addition to transiting material. The former likely comprises six planet(esimal)s in the process of disintegration: the transits occur every 4.5 to 4.9 hr with varying depths (max

40%) and an asymmetric profile (Vanderburg et al. 2015). The authors posit the six bodies to be the remnants of a close-in, tidally-disrupted planet of which the fragments are too dense ($\rho \geqslant 2\,\mathrm{g\,cm^{-3}}$) to undergo further tidal disruption. Instead, their ongoing disintegration implied by ground-based observations of dust tails is thought to be facilitated by heating from the WD. The material transiting J013906.17+524536.89, on the other hand, exhibits much longer periodicity with transits occuring every 107.2 d and a transit depth varying between 20 and 40% (Vanderbosch et al. 2020). This implies that the transiting material lies far outside the RL and experiences less irradiation than the material encircling WD 1145+017. That said, the material still lies within the region engulfed during the post-MS evolution of the WD's progenitor. Therefore, the authors propose that the debris lies on an eccentric orbit with a periastron within the RL of the previously intact planet(esimal). At the time of writing, this model awaits observational confirmation.

Nearly all of the aforementioned observational evidence for WD planetary systems has required the destruction of planetary bodies. Though authors such as Frewen & Hansen (2014) have envoked massive, intact planets on eccentric orbits to facilitate the dynamical instabilities that propel lighter planet(esimal)s within their RLs, the giant planet, WD 1856b discovered by Vanderburg et al. (2020) is the first direct evidence of an intact planet. The body was found to have a phenomenally high transit-depth: 56.65 % at optical and 56.3 % at infrared wavelengths on a grazing transit. For reference, the transit of gas giant HD 209458b around its host star is $\sim 1.7\%$ (Charbonneau et al. 1999). WD 1856b is found to have a radius 7.28 ± 0.65 as large as its host WD and $10.8^{+3.5}_{-2.5}$ when fitted for an eccentric orbit. On the other hand, the pristine, near-blackbody[6] spectrum of the WD provides a lack of absorption lines for constraining the mass using radial velocity measurements. Instead, the lack of thermal emission detectable to the *Spitzer Space Telescope* is used to impose an upper limit of $13\,\mathrm{M_J}$. In other words, to discount the possibility of WD 1856b being a Brown Dwarf to within a 95% confidence interval. This is a really important finding as it has lead the authors to propose planetary migration as the principal explanation for its 1.408 d orbital period and $0.198 - 0.0204\,\mathrm{AU}$ semi-major axis. Crucially, Vanderburg et al. (2020) argues that the migration of WD 1856b may demonstrate a mechanism by which planets can become habitable despite the likely engulfment of previously habitable planets during the post-MS evolution of the WD's progenitor. Several follow-up studies have noted that WD 1856b likely migrated to its current semi-major axis (0.0204(12) AU) via the Zaipei-Lidov-Kozai mechanism[7] from further orbital distances ($\sim 2.5\,\mathrm{AU}$) (Muñoz & Petrovich 2020; Stephan et al. 2020; Lagos et al. 2021; O'Connor et al. 2021). However, given that WD 1856b is a giant planet, Lagos et al. (2021) have argued that its likely atmospheric retention

---

[6]Unless the WD is polluted, only a few hydrogen and helium lines are present, depending on which is the dominant photospheric constituent.

[7]The nearby binary system G 229-20 inducing oscillations in WD 1856b's orbit and causing it to decay. See Muñoz & Petrovich (2020) for a full analysis.

results from common envelope evolution[8]. As Earth-mass planets would not be able to experience common envelope evolution, they may be more inclined to lose their atmospheres due to extreme ultraviolet photons at such close orbital distances. This obstacle to their habitability will be treated in more detail in Section 5.1.

The high transit-depths are perhaps the principal reason for WD planets being excellent targets to characterise for habitability: the NIRSpec Instrument James Webb Space Telescope (JWST) should be sufficiently powerful to detect biosignatures in the atmospheres of planets with such high transit-depths (Batalha et al. 2018; Kozakis et al. 2020). Though no such observations have been conducted to date, the near future should see a wealth of incoming data on the atmospheres of WD planets, including WD 1856b itself. Now that it has been established what characteristics of WD planets can be inferred from transit observations, the demographics of WDs within 100 pc will be discussed to establish whether they are likely to be good targets for transit photometry searches. This upcoming subsection will also explore the demographics of polluted WDs to facilitate an analysis of the compositions of their planetary systems.

2.2. White Dwarf Demographics

All of the aforementioned detection methods have currently been employed to estimate the abundances of WD planets. However, with WD transit observations in their infancy and circumstellar disk detections in a somewhat early stage of development, pollution is currently the best metric for probing populations of WD planets. Indeed, even detecting pollution has physical limitations. Therefore, any analysis of the composition and habitability of WD planetary systems necessitates a review of the available data, which is grounded on the demographics of known WDs in local regions of the Milky Way. Specifically; the total quantity within a given distance, their mass and effective temperature distribution and what metals are most commonly found in polluted WDs. To this end, Section 2.2.1 analyses the demographics of local WDs in light of the findings of Jiménez-Esteban et al. (2018) to inform an estimate of the upper bound on the number of Earth-size planets transiting WDs within 100 pc in Section 2.2.2, and Section 2.2.3 discusses WD data from the Montreal White Dwarf Database (Dufour et al. 2017), in order to motivate an analysis of the compositions of polluted WDs in Section 2.3 and the Habitable Zones of WDs in Section 3. That said, there will be a greater emphasis on WD pollution data in Section 2.2.3, as this will be directly analysed in the following Section (2.3).

2.2.1. Gaia Data Release 2: White Dwarfs within 100 pc.

The *Gaia* Data Release 2 catalogue of white dwarfs appears to provide the most complete and comprehensive review of local WDs to date (Jiménez-Esteban et al. 2018). In total, 73 221 WDs candidates were extracted from as-

---

[8]Recall the discussion of the giant planet being accreted from a circumstellar disk in Section 2.1.2.

trometric and photometric data of the *Gaia* DR2 catalogue and compared with Monte-Carlo based population synthesis models wich were used to estimate the likely abundances and distributions of WDs. From this, Jiménez-Esteban et al. (2018) conclude that 97% of the expected WDs with $T_{\text{eff}} = 6000 - 8000$ K within 100 pc have been identified: a total of 8555 WDs. This fraction falls below 60% within 250 pc and 22% within 500 pc. An analysis of the mass and effective temperature distributions of WDs within 100 pc motivates a brief discussion of whether their planetary systems are likely to be habitable, justifying an estimation of an upper bound on the number of WDs likely to have transiting Earth-size planets in the Habitable Zone in Section 2.2.2.

Naturally, the 100 pc sample was chosen to be characterised by Jiménez-Esteban et al. (2018). This selection was further reduced to 94% by firstly filtering out stars with a parallax error > 10% and further reduced to 44% by imposing the criterion 6000 K $\lesssim T_{\text{eff}} \lesssim 80\,000$ K. This latter cut was taken due to the large expected contamination at the corresponding colours, which would inhibit reliable characterisation of the sample. After applying these conditions, they find a concentration of WDs at $T_{\text{eff}} \approx 8000$ K with an exponential decline at higher temperatures and a very sharp drop in available data at lower ones, Whilst the former property is intrinsic to WDs and results from their exponential cooling, the latter is due to the effects of filters that eliminate data with a high photometric error. Additionally the data exhibit an interesting bimodality in their mass distribution (see Fig. 2), indicating that there is a significant local population of massive WDs ($M \sim 0.8\,M_{\odot}$) alongside the majority that exhibit canonical WD masses ($0.6\,M_{\odot}$). Explanations for this massive population include binary mergers (Kilic et al. 2018), and a recent bout of star formation (Torres & García-Berro 2016). As massive WDs have smaller radii (Provencal et al. 1998; Miller Bertolami et al. 2014; Parsons et al. 2017), this bifurcation carries through to the radius and surface gravity distributions as well (see Jiménez-Esteban et al. (2018) for a full analysis).
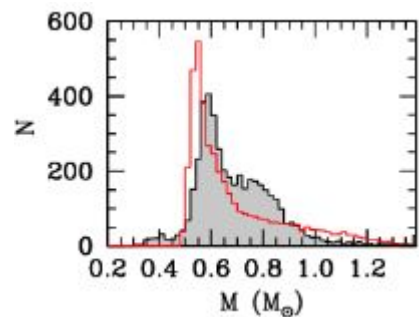
Fig. 2. The mass distribution in the sample of WDs within 100 pc. The grey signifies the *Gaia* WDs whilst the red signifies the synthetic population models (Jiménez-Esteban et al. 2018).

The implication of the 8000 K peak is that the majority of WDs within 100 pc of the Solar System are cool and have therefore long passed the planetary nebula phase at which the central star (that eventually becomes the WD) has a temperature of $\sim 30\,000$ K. This provides an optimistic outlook for the habitability of local WD planetary systems: as WDs cool exponentially, the Habitable Zones

(HZs) are likely to have stabilised in many of them. The habitability of (younger) systems with higher temperature would depend strongly on the interplay between planetary migration and HZ evolution. Given that for the history of life on Earth, $T_{\mathrm{eff},\odot} \lesssim 5800\,\mathrm{K}$, the higher contamination at lower T_{eff} presents an obstacle to the detection of habitable WD planets *if* Earth-like conditions are imposed as a prerequisite for life. Whether it seems necessary to impose such conservative criteria will be further discussed in Section 3.

The local mass bimodality should also be taken into account when considering habitability. $0.8\,\mathrm{M}_\odot$ and $0.6\,\mathrm{M}_\odot$ WDs exhibit different cooling tracks which in turn should effect the radiative environments. To illustrate this point, publicly available cooling models for $0.6\,\mathrm{M}_\odot$ and $0.8\,\mathrm{M}_\odot$ WDs have been plotted in Fig. 3 (Bédard et al. 2020). In Fig. 3, it can be seen that the cooling tracks for $0.6\,\mathrm{M}_\odot$ and $0.8\,\mathrm{M}_\odot$ both appear to cool rapidly with the same form and then branch off from each other. The $0.6\,\mathrm{M}_\odot$ WDs cool more rapidly and reach lower temperatures quicker than their $0.8\,\mathrm{M}_\odot$ counterparts. This makes intuitive sense as the massive population would experience greater self-gravity and would require greater electron degeneracy pressure to resist further collapse. As a result, they would have higher temperatures to begin with and take longer to cool down. At $log(T) \approx 3.90$ (corresponding to the aforementioned $T_{\mathrm{eff}} = 8000\,\mathrm{K}$ peak), the $0.6\,\mathrm{M}_\odot$ population exhibit a faster exponential decline in T_{eff}. Likewise, the $0.6\,\mathrm{M}_\odot$ model exhibits a faster decline in luminosity. Since HZ boundaries are proportional to the square root of luminosity, $d \propto L^{\frac{1}{2}}$ (see Section 3), the $0.8\,\mathrm{M}_\odot$ population may have stable HZs sooner than their lighter counterparts. However, the higher T_{eff} of the $0.8\,\mathrm{M}_\odot$ WDs would correspond to shorter λ peaks in their (near-blackbody) light curves. This is likely to increase the UV flux experienced by planets orbiting in the HZ which would have direct implications for sensitive photochemical reactions such as Ozone production in their atmospheres (Kozakis & Kaltenegger 2019). That said, this latter consideration is more important for surface organisms. If it is assumed that life has to originate deep underwater, the UV flux is unlikely to penetrate far enough to interfere with the evolution of simple lifeforms.

2.2.2. Detectable Earth-like Planets

Now that the intrinsic properties of local WDs have been discussed extensively and shown to be somewhat conducive to habitable planetary systems, the number likely to have transiting Earth-like planets within the HZ can be estimated. This is to demonstrate the relevance of the intrinsic properties of WDs to their planetary systems and to assess the extent to which other detection methods would be needed to support transit photometry in the search for habitable WD planets.

By injecting a sample of 1148 K2 WDs with artificial transits, van Sluijs & Van Eylen (2018) have estimated an upper bound of 28% on Earth-sized planets orbiting WDs. This implies an upper limit of 2395 planets orbiting the 8555 WDs observed within 100 pc (Jiménez-Esteban et al. 2018). To estimate the transit probability of such objects within

the HZ Eqn. (1) can be used.

$$p_{\mathrm{tra}} = \frac{R_\oplus + R_{\mathrm{WD}}}{a_{\mathrm{HZ}}} \tag{1}$$

where $R_\oplus$ is the Earth's radius, R_{WD} is the radius of the WD and a_{HZ} is the semi-major axis of the HZ van Sluijs & Van Eylen (2018); Vanderburg et al. (2015). Following Fulton et al. (2014), it can be assumed that $R_{\mathrm{WD}} \sim 0.012\,\mathrm{R}_\odot$ and from data that will be presented in Section 3, it is further assumed that $a_{\mathrm{HZ}} \sim 1.5 \times 10^{-2}\,\mathrm{AU}$. Plugging these values into Eqn. (1) and expressing the result as a percentage, a mere 0.656% transit probability is found. Therefore, there are likely to be at most 15 Earth-analogues transiting the WDs that have been found within 100 pc. This low transit probability is the price to pay for the high potential transit depth, owing to the small radii ($\sim 0.013\,\mathrm{R}_\odot$) of WDs. As direct imaging is the only other existing detection technique capable of probing exoplanet atmospheres, drastic improvements in imaging instrumentation may prove indispensable in improving the sample size of WD-orbiting, HZ Earth-analogues that can be examined for bio-signatures.

2.2.3. Montreal White Dwarf Database

Although the findings by Jiménez-Esteban et al. (2018) on the 100 pc sample have been informative on the deducing likely transit probabilities, their filtering out of WDs with $T_{\mathrm{eff}} \lesssim 6000\,\mathrm{K}$ is a severe limitation in constraining the planetary systems of WDs for habitability. As can be inferred from Fig. 3, the cooling age for which $T_{\mathrm{eff}} \approx 6000\,\mathrm{K}$ corresponds to that at which the effective temperatures and luminosities stabilise. As a consequence of the latter point, this is also the cooling age at which the HZs stabilise. Thus, a different dataset is required if it is taken to include systems likely to be habitable. Additionally, Jiménez-Esteban et al. (2018) do not explore pollution in their discussion, which is a crucial method for inferring the presence of planets. As a resolution to both of these points, the *Montreal White Dwarf Database* provides publicly accessible data on 56713 [9] WDs and allows for a quick and easy assessment of WD demographics, complete with both data on pollution and objects with $T_{\mathrm{eff}} < 6000\,\mathrm{K}$ (henceforth cited as Dufour et al. (2017)). Given that 1129 of the WDs in the database are polluted and that 32 have disks, a lower bound of $\geqslant 2\%$ can already be inferred on the percentage of WDs that host planets. From more detailed studies, the percentage has been inferred to lie between 25 and 50%, a similar value to that of Main Sequence (MS) systems found to have debris disks (Zuckerman et al. 2003; Zuckerman et al. 2010; Koester et al. 2014), and slightly lower than those found to host *at least* one terrestrial exoplanet (Cassan et al. 2012; Veras 2016). This small discrepancy is likely owing to the finite probability of a planet being tidally disrupted.

The most striking facet of the database's polluted subset is the dearth of DAZ (polluted hydrogen-rich) WDs: only 4 of the 1129 datapoints have hydrogen as their dominant atmospheric constituent. This is undoubtedly a selection effect. hydrogen-rich WDs have much higher opacities which makes the identification of metallic spectral features in their

---

[9]Accessed 01/10/2020.
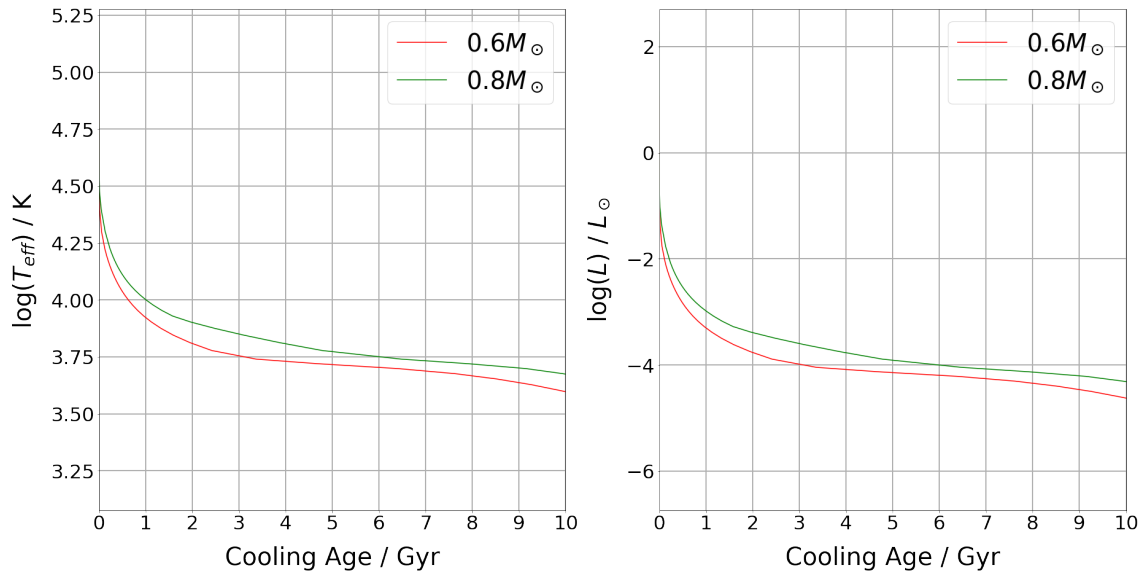
Fig. 3. The Effective Temperatures T_{eff} and Luminosities L plotted logarithmically for the theoretical cooling tracks of $0.6\,\text{M}_\odot$ and $0.8\,\text{M}_\odot$ White Dwarfs. Both models assume a thin Hydrogen layer as dominant constituent in the atmosphere.

atmospheres much harder (Dupuis et al. 1993; Farihi 2011). This is an important bias to bear in mind when analysing this pollution data at young cooling ages. Hydrogen-rich atmospheres are found in $\sim 80\%$ of WDs with $T_{\text{eff}} > 12\,000\,\text{K}$ (Eisenstein et al. 2006). This is because diffusion timescales for heavy elements in DA (hydrogen-rich) WDs are much shorter between $12\,000\,\text{K}$ and $25\,000\,\text{K}$ (Koester 2009). In contrast, the (polluted He-rich) DBZ WDs at these temperatures have very low hydrogen abundances ($\sim 10^{-5}$) and are thought to have ejected most of their primordial hydrogen in the thermal pulses of their AGB progenitors (Voss et al. 2007). The underabundance of hydrogen in DBZ WDs can be advantageous when reconstructing planetesimal compositions from pollution data: if an overabundance of hydrogen is deduced in conjunction with oxygen, the relative abundances could be compared to infer the presence of water on the polluting body. Given that life as it is known requires water as a solvent and that water on Earth may have originated from cometary bombardments (Robert 2001), the inference of water in WD planetary systems is arguably crucial to determine its habitability. However, its inference depends on the precise determination of hydrogen overabundance and its cross-correlation with oxygen abundances, which is beyond the scope of this thesis. Therefore, the following section will focus on the metals that have been detected in polluted WDs and what they can imply regarding the bulk compositions of WD planets.

2.3. Planetary Compositions

With data from the *Montreal White Dwarf Database*, the [Fe/Mg] ratios of 235 polluted WDs can be used to compare their bulk compositions to those of Solar System objects. This will be treated in Section 2.3.1. However, there are a select few heavily polluted WDs which exhibit more metallic spectral lines than others. These have been studied by Xu et al. (2013) and the implications of their study will be discussed in Section 2.3.2.

2.3.1. General Trends in White Dwarf Pollution

In order to allow for a fairer comparison, the 4 hydrogen-dominated WDs were excluded from the 1129 found polluted dataset. 990 of the remaining WDs in the polluted subset exhibited calcium lines. As previously discussed, the Ca II H and K spectral features are very prominent so the overabundance of calcium in the pollution data is undoubtedly a selection effect. Hydrogen features were the second most abundant with 931 datapoints. This too is likely a selection effect due to the element's strong spectral features. However, none of the data were found to exhibit oxygen spectral features. Therefore, identifying water as a potential pollutant is virtually impossible with this dataset. Magnesium and iron were found in 236 and 235 of the datapoints respectively. Given that iron is a crucial constituent of massive planets and that magnesium is found in an almost identical number of data-points, the [Fe/Mg] ratio can be effectively used as a metallicity tracer across this dataset and compared with solar system values to infer the compositional similarity of WD planetary systems.

It should be recalled that only $\sim 20\%$ of all WDs are thought to be helium-rich (Giammichele et al. 2012), and that their overabundance in the data-set is a result of selection bias due to their relatively transparent atmospheres. That said, there is not *much* reason to suppose that their planetary systems and habitable environments drastically differ, It can further be noted that bodies that pollute WDs are planet(esimal)s that have been tidally disrupted and accreted. Therefore, the observed pollutants betray the compositions of *former* planet(esimal)s rather than *actual* ones. Nevertheless, inferring general compositions of WD planetary systems can be a useful diagnostic to assess their general similarity to the Solar System. To illustrate this, a histogram of the [Fe/Mg] ratios of polluted WDs is plotted in Fig. 4.

To estimate [Fe/Mg] for the Solar System bodies in Fig 4, bulk compositions were obtained from Morgan & An-
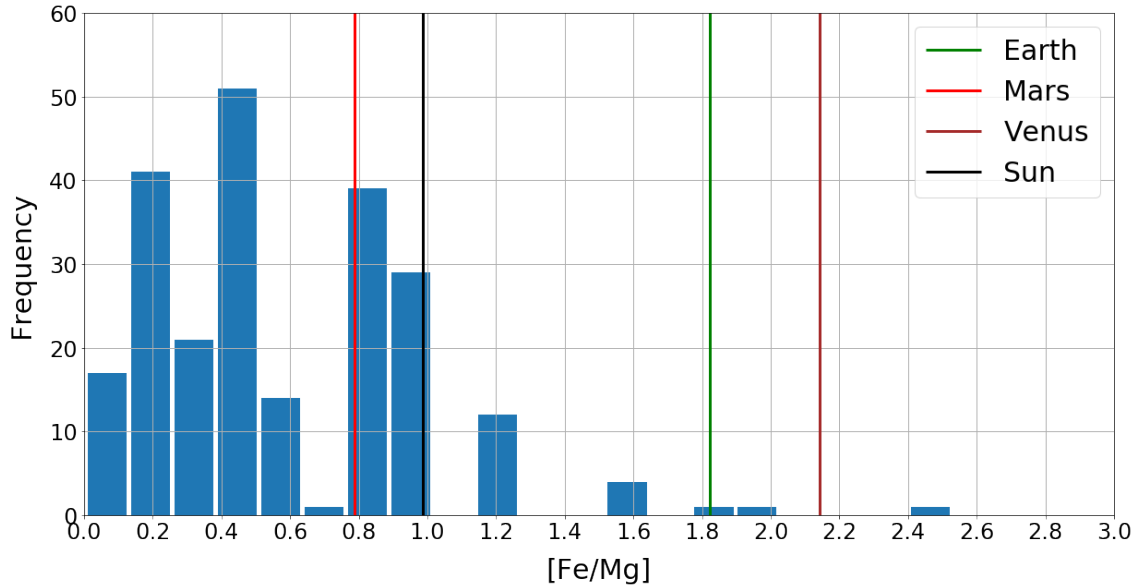
Fig. 4. The relative abundances of [Fe/Mg] for polluted WDs, compared with those of Solar System bodies. Error bars are not plotted as no data were available on the uncertainties of elemental abundances from Dufour et al. (2017).

ders (1980); Asplund et al. (2009); Allègre et al. (2001); Taylor (2013); **?**. A stark contrast in the [Fe/Mg] of polluted WDs and Solar System bodies is immediately manifest: only martian and solar metallicities are comparable to those found in any considerable number of polluted WD whilst the majority have even lower [Fe/Mg] values. Given that iron and magnesium spectral features are found in similar numbers of WDs, it is difficult to attribute this to a selection effect. This suggests that the planetesimals that pollute helium-rich WDs generally have greater abundances of magnesium with respect to iron than objects in the Solar System. Them generally being more abundant in lighter elements such magnesium than in heavier ones such as iron ([Fe/Mg] < 1) may in fact be the very reason they end up polluting the photospheres of their host WDs.

According to a simulation by Jorge (2020), increased [Fe/Mg] values for hypothetical planets forming at the distances of various terrestrial bodies in a solar protoplanetary disk result in the planets having larger cores. This makes intuitive sense as iron's greater relative mass would predispose it to sink to the bottom of any planet in the formation process. In most cases it can be assumed that WDs have inherited the planetary systems that survived the post-MS evolution of their progenitors and therefore that WD planet(esimal)s were also formed in a protoplanetary disk. Applying the finding of Jorge (2020) to Fig. 4, it may be reasoned that the majority of WD-polluting bodies have relatively small core sizes. This too would make intuitive sense as their low relative mass and therefore higher relative levity would predispose them to the dynamical instabilities required to propel them onto a WD atmosphere. The implication of this finding is that lower-mass bodies (ie. asteroids) are more likely to pollute WDs than higher mass ones. This says more about the phenomenon of WD pollution than it does about the actual compositions of WD planetary systems. Therefore, a more thorough analysis of polluted WDs is warranted in Section 2.3.2.

Finally, it should be noted that although most polluted WDs exhibit relatively low [Fe/Mg] ratios, there do appear to be some exhibiting terrestrial values. On their own, these data would not be sufficient to insinuate that Earth-like bodies are being accreted by WDs. However, as discussed earlier, the finding by Gänsicke et al. (2019) of a tidally disrupted giant planet, suggests that massive bodies too can be vulnerable to tidal disruption, albeit to a lesser degree than lighter bodies with lower [Fe/Mg] ratios. In fact, it is possible that the HZs themselves lie dangerously close to typical WD RLs. Kaltenegger et al. (2020) find that the HZ of WD 1856+534 is located at $\sim 2.9\,R_{\mathrm{Roche},\oplus}$ where $R_{\mathrm{Roche},\oplus}$ is the RL for an Earth-analogue with respect to WD 1856+534. For comparison, Earth orbits the Sun at $\sim 268\,R_{\mathrm{Roche},\oplus}$. Naturally, for a WD planetary system to provide habitable conditions for an Earth-analogue, the HZ should lie outside $R_{\mathrm{Roche},\oplus}$ and preferably far outside. The extent of this tidal vulnerability will be treated in more detail in Section 3.

2.3.2. Heavily Polluted White Dwarfs

As has been shown in the previous paragraphs; in most polluted WDs, only species with the strongest absorption lines can be detected and therefore only superficial conclusions can be sought on planetary compositions. However, a broader variety of species have been inferred in a select few WDs; especially GD 362 in which sixteen[10] metals have been found (Jura et al. 2007). GD 362 and eight[11] other polluted WDs exhibiting nine or more species in their spectral inventories perhaps represent the best studied objects of this class. In these cases, the abundance data have been

---

[10]N, O, Na, Mg, Al, Si, Ca, Sc, Ti, V, Cr, Mn, Fe, Co, Ni, Cu, Sr, C* and S* where * indicates that the species are in their excited states.
[11]GD 40, WD J0738+1835, PG 0845+517, PG 1225-079, NLTT 43806, WD 1929+012. G241-6 and HS 2253+8023.

sufficient to enable comparison with different classes of Solar System meteorites.

GD 362 is undoubtedly the best studied polluted WD. Coincidentally, its metallic spectral features are accompanied by a mid-infrared excess found using the *Spitzer Space Telescope*; a major corroboration of the aforementioned asteroid accretion model (Jura et al. 2007). In a follow-up study using the Cosmic Origins Spectrograph of the Hubble Space Telescope, Xu et al. (2013) report UV spectroscopic data to corroborate the findings of Jura et al. (2007) but also to determine constrain upper limits on *volatile* elements such as carbon and sulphur, defined as having a 50% condensation temperature lower than 1290 K in a solar-system composition gas (Lodders 2003). They compare these abundances with those of *intermediate* elements such as iron and magnesium, defined as having a condensation temperature between $1290 - 1360$ K and *refractory* elements such as calcium, titanium and aluminium, defined as having a 50% condensation temperature than 1360 K. What they find is that the asteroid ($m_{\min} \sim 10^{22}$ g (Jura et al. 2007)) responsible for polluting GD 362 exhibits similar relative abundances of the volatile, intermediate and refractory elements to mesosiderite meteorites. These are a rare class of stony-iron solar-system meteorites which have undergone extensive post-nebular processing and are thought to originate from the asteroid 16 Psyche (Davis et al. 1999). Though Xu et al. (2013) state unresolved issues such as the difficulty of reconciling its mid-infrared spectrum with that of the circumstellar disk around GD 362, this finding is important in that it suggests a congruence between the types of asteroid found in WD planetary systems and those in WD planetary systems. Beyond this, however, it is unclear how relevant this finding is for directly informing the habitability of the system. A space mission scheduled to arrive at 16 Psyche in 2026 may provide more information on whether its composition is at all indicative of the protoplanetary conditions that facilitated life on Earth or at least, the formation of the massive terrestrial planets needed for life (Elkins-Tanton et al. 2014).

The other polluted WD that Xu et al. (2013) study in great detail is PG 1225-079. Their findings for this, however, are very different; they conclude that in terms of the relative abundances of volatile, intermediate and refractory elements it has no solar-system analogue. However, they also report carbon and sulphur abundances higher than those found in GD 362 at $\log\left[\frac{C*}{He}\right] = -7.80$ and $\log\left[\frac{S*}{He}\right] \lesssim -9.50$ respectively[12]. They find $\left[\frac{C}{S}\right]$ to be the solar value at least, in stark contrast to most other polluted WDs. The closest single solar system analogue is carbonaceous chondrite and the best fit for the relative abundances is provided by a blend of 30% urelite and 70% mesosiderite. It should be noted that $2 - 6$ carbon aliphatic primary amino acids have been identified on the meteorite 2008 TC$_3$ which happened to be a complex amalgamation of chondritic and ureilitic material (Burton et al. 2011). Likewise, carbonaceous chondrites have been found to host amino acids (Ehrenfreund et al. 2001). Although the spectrum of of PG 1225-79 matches neither of these meteoritic species to any significant degree, its high relative carbon abundance is definitely

an important consideration in the assessment of the habitability of its planetary system. For one thing, it confirms the presence of carbonaceous matter in planet(esimals) beyond post-MS evolution. For another, it hints that organic matter may be present in the system, which perhaps is a pre-requisite for abiogenesis. Furthermore, the positive detection (albeit low relative abundance) of sulphur betrays the presence of another key element of which biological molecules are composed.

As for the elemental abundances of other polluted WDs cited by Xu et al. (2013), GD 40 and HS 2253+8023 are of particular note. The former, as shown in Jura et al. (2012) Appendix B, exhibits an abundance pattern closely matching both carbonaceous chondrites and bulk Earth. The authors attribute the origin of the polluting body to nebular condensation. The latter, as shown in Klein et al. (2011), had a composition similar to Bulk Earth (85%) in oxygen, magnesium, silicon and iron but an enhanced calcium abundance. This composition too can be explained by nebular condensation.

In summation, it can be seen that polluted WDs reveal a significant diversity in the compositional nature of their planetary systems. With some abundances consistent with primitive formation processes such as nebular condensation, others disclose post-nebular processing which could either arise from the violent dynamical environment of its WD progenitor's pre-MS protoplanetary disk, or the complex dynamical changes from its progenitor's post-MS evolution. Whatever the origin of the accreted material, the unequivocal presence of elements such as carbon and sulphur in the spectra indicate that the basic material needed for life to develop is indeed present in the planetary systems of WDs. Whilst being far from a remarkable discovery, this is an important finding, especially when considered in conjunction with post-MS evolution. As will be shown in Section 4, the circumstellar envelopes of AGB stars, proto-planetary nebulae and planetary nebulae: the three stages of stellar evolution that precede WDs, have been found to be abundant in carbonaceous material such as Polycyclic Aromatic Hydrocarbons (PAHs). Therefore, the possibility of post-MS evolution influencing the compositions of WD planetary systems should be explored or at least, borne in mind. Before this, however, it is crucial to establish the proximity of the HZ to the RL of an Earth-analogue with respect to a WD. If terrestrial planets orbiting in the HZ are likely to share the same fate as the planet(esimal)s discussed in this section then the compositional similarities between WD planetary systems and that of our Solar System are irrelevant to the question of whether WD planets are capable of hosting life.

---

[12]Those for GD 362 are reported as $\log\left[\frac{C*}{He}\right] = -6.70$ and $\log\left[\frac{S*}{He}\right] \lesssim -6.70$

3. Habitable Zones around White Dwarfs

This section explores to what extent white dwarfs can support Earth-like planets at the orbital distances required for water to be a liquid on their surfaces. To this end, Section 3.1 formulates two important variables which will be used throughout Section 3. The first of these, the Habitable Zone (HZ) distance, formulated in Section 3.1.1, is that at which a planet receives the necessary radiative flux from its stellar host to sustain liquid water on its surface, given sufficient atmospheric pressure. The second, the Roche Limit (RL), quantified in Section 3.1.2, is the orbital distance at which a given planet would be disintegrated by the tidal forces of its stellar host. Naturally, the stellar host here is assumed to be a White Dwarf (WD). An important consequence of this is that the HZ changes as the WD cools. In Section 3.2, the HZ distance is defined to be that at which a planet would receive the same radiative flux as the Earth does from the Sun. This is calculated for 83 WDs of different cooling ages[13] obtained from the *Montreal White Dwarf Database* (henceforth cited as Dufour et al. (2017)). Then, it is observed whether the HZ distances meet two criteria:

1. **Stable** for a sufficient amount of time for life to evolve $\sim 1\,\mathrm{Gyr}$: determined by plotting the cooling ages against HZ distances
2. **Far-enough** from the WD for an Earth-like planet to remain intact: determined by normalising all HZ distances to their corresponding RLs so that any value less than 1 can be excluded

In Section 3.3, the concept of the HZ is extended to include a range of orbital distances with inner and outer boundaries calculated for the same 83 WDs as in Section 3.2. The inner and outer boundaries will be defined at the beginning of Section 3.3. Throughout Sections 3.2 and 3.3, the HZ distances are compared with the corresponding RLs of the WDs. This is primarily to gauge whether a planet with the same density as Earth (henceforth referred to as 'Earth-like') could even exist within the HZ of a WD. As can be seen from Fig. 3 in Section 2.2.1, the luminosities of WDs ($\sim 10^{-4}\,\mathrm{L_\odot}$) do not scale down proportionally to their masses ($\sim 0.6\,\mathrm{M_\odot}$) from main-sequence values like those of the Sun[14]. In Section 3.1, it is explained that the HZ distance depends directly on the stellar host's luminosity and effective temperature whilst the RL depends directly on its mass. Therefore, there is credible reason to investigate the HZs of WDs overlap with the RLs of WDs. The Earth orbits the Sun in a HZ about 269 times as far away as its RL. In the case of WDs, however, the HZ should be much closer. If an Earth-like planet with liquid water on its surface is required to facilitate life, the HZ being within the planet's RL with respect to its host WD would preclude that planetary system from being habitable. Therefore, the importance of this investigation cannot be overstated.

Before proceeding to the main-body of this section, it should be noted that error bars for the quantities[15] cal-

culated here could not be plotted in light of difficulties encountered with the `pandas` package. Regardless of that, plotting them in figures here would make graphs extremely convoluted; especially as their values do not form a centerpiece of discussion at any point of discussion in this thesis. That said, if the reader wishes to review the uncertainties of all datapoints considered, they are referred to Appendix A wherein the errors for all quantities calculated in this section have been propagated and tabulated.

3.1. Key Parameters

As explained in the previous paragraph, two important variables are quantified here: the Habitable Zone (HZ) distance and Roche Limit (RL). The former is tackled in Section 3.1.1 and the latter in Section 3.1.2. This then facilitates their comparison throughout Sections 3.2 and 3.3.

3.1.1. Habitable Zone Orbital Distance

Since the late 1950s, the Habitable Zone (HZ) of a planetary system has typically been defined as the distance from a star or multiple stars at which a planet is capable of sustaining liquid water on its surface (Kasting et al. 1993). In this case, a single White Dwarf (WD) is assumed to be the star. This definition assumes the planet has an atmosphere supplying the necessary pressure for the liquid phase of water to be realised. This is principally because all known lifeforms require liquid water to metabolise and reproduce (Güdel et al. 2014). Importantly, water is also the solvent required to facilitate crucial biochemical reactions in *carbon-based* lifeforms. This is owing to water's versatility facilitated by its ability to form hydrogen bonds, stabilise macromolecules and to orient hydrophobic-hydrophilic molecules (Lammer et al. 2009).

Before mathematically formalising the above definition, it is important to introduce a formula for the effective radiative flux experienced by a given planet. This variable, defined as the power radiated through a given area, depends on the effective temperature of the host star, T_{eff}. In this case, the temperature dependence is given by a fourth-order polynomial fit (with a through d being constant), following the formalism of Ramirez & Kaltenegger (2018):

$$S_{\mathrm{eff}} = S_\odot + aT_* + bT_*^2 + cT_*^3 + dT_*^4 \tag{2}$$

where $T_* = T_{\mathrm{eff,\,WD}} - 5780\,\mathrm{K}$ normalises the temperature of the WD to that of the Sun and $S_\odot$ is the solar radiative flux at a given distance in the Solar System. This parameter and the coefficients a through d are those that change depending on whether the orbital distance is being calculated for the inner, outer HZ edge or Earth-insolation distance[16]. These values are determined by climate models and are explained directly before use in Section 3.3.

From the inverse-square law, it follows that the distance of a given HZ boundary of a WD, d_{HZ} in Astronomical Units

---

[13]Time elapsed since the progenitor became a WD.

[14]As demonstrated by the values in brackets being expressed in solar units

[15]HZ distances, RLs and the % extension of outer HZ boundaries facilitate by methane being invoked as a greenhouse gas.

[16]Distance at which the incident radiative flux is the same as that received by Earth from the Sun.

(AU) can be formulated in terms of luminosity, L_{WD} and effective flux, S_{eff} necessary to meet a given condition:

$$d_{\mathrm{HZ}} = \sqrt{\frac{L_{\mathrm{WD}}/L_{\odot}}{S_{\mathrm{eff}}}} \qquad (3)$$

where L_{WD} is in units of $L_{\odot}$, the Sun's luminosity; S_{eff} is the incident stellar flux normalised[17] to that received by Earth from the Sun and d_{HZ} is in Astronomical Units (AU). For the simplest case, $S_{\mathrm{eff}} = 1$. This corresponds to the Earth-insolation distance of WD planets and provides the most conservative HZ distance; that is, the exact distance from a WD that a planet would need to be to receive a flux equivalent to that of Earth from the Sun, assuming the planet is in radiative equilibrium. This is, as opposed to HZ boundaries which allow a range of orbital distances, modelling the interaction of the climate of a given planet with the distance-dependent flux it receives.

3.1.2. Roche Limit

The stellar Roche Limit (RL) is defined as the distance from the star at which a planet's self-gravity would be overcome by the star's tidal forces (Aggarwal & Oberbeck 1974). To echo the topic of Section 2.1.2, any objects that drift within their RLs with respect to the WD would be disintegrated and form a circumstellar disk, providing a source of metallic pollution for the WD's photosphere. Any objects outside their RLs with respect to the WD, such as the transiting planet found by Vanderburg et al. (2020) would remain intact. For a planet to be habitable, it naturally has to remain intact. Due to the low luminosities of WDs, their HZs are expected to be very close-in ($\sim 1.5 \times 10^{-2}$ AU) and therefore at comparable to their RLs. Therefore, it is important to investigate whether the HZ distances in fact coincide with the RLs for Earth-like planets around WDs: such a condition could preclude a WD planetary system from being habitable. The RLs are being treated for Earth-like planets here because Earth is the only sample of a habitable planet at the time of writing[18]. In this case, "Earth-like" signifies a planet with the Earth's density ($\rho_{\oplus} = 5515$ kg m^{-3}). Thus, the mass of the WD remains the only free parameter. Assuming that the Earth-like planet follows a circular orbit exhibiting synchronous rotation, it can be inferred from Newtonian mechanics that this distance is given by

$$R_{\mathrm{Roche}} = \left(\frac{9 M_{\mathrm{WD}}}{4\pi \rho_{\oplus}}\right)^{1/3} \qquad (4)$$

where M_{WD} is the mass of the WD and $\rho_{\oplus}$ is the Earth's density. In this case, R_{Roche} is calculated in SI units and converted to AU in order to be dimensionally consistent with d_{HZ}. Now this value can be compared with d_{HZ} to determine whether an Earth-like planet could remain intact in the HZ around a WD.

---

[17]As d_{HZ} is given in AU, (ie. the Earth's distance from the Sun) and L is in $L_{\odot}$, it follows that S_{eff} is given in terms of the radiative flux Earth receives.

[18]27th of February 2021

3.2. Earth-insolation Distances

Recalling the cooling tracks from Fig. 3 in Section 2.2.1 and reviewing them in conjunction with Eqn. (3), it can easily be deduced that the d_{HZ} is likely to have a similar form. As previously mentioned in Section 3.1.1, S_{eff} in Eqn. 3 is normalised to the Earth's incident radiative flux. Therefore, the Earth-insolation distance can simply obtained by setting $S_{\mathrm{eff}} = 1$. This provides the most-conservative estimate of d_{HZ}: technically not a Habitable *Zone*; rather a Habitable *Distance*. Therefore, a comparison between this HZ value and the RL reveals whether a perfect Earth-analogue in terms of both its density, $\rho_{\oplus}$ and incident stellar flux, $S_{\mathrm{eff}(\oplus)}$ would survive in orbit around a WD.

In order to examine the time evolution of WD HZs, data were obtained from the *Montreal White Dwarf Database* complete with values for L_{WD}, M_{WD}, $T_{\mathrm{eff, WD}}$ and t_{cool} where t_{cool} is the Cooling Age in Gyr; the time elapsed since fusion reactions in the WD's progenitor ceased and the commencement of the WD phase (Dufour et al. 2017). A filter was applied to the data, requiring that $T_{\mathrm{eff}} < 10\,000$ K in order to ensure compatibility with the climate models of Ramirez & Kaltenegger (2018). After this, 83 WDs were left in the dataset. Eqn. (3) was then applied to the L_{WD} values (initially assuming radiative equilibrium) to obtain d_{HZ} values for each WD. All calculations were performed in Python using the `pandas` package for data science. From this, Fig. 5 was obtained. As can be seen on the left hand plot of Fig. 5, the orbital distances are on the order of $\sim 10^{-2}$ AU, two orders of magnitude lower than those of the Solar System (1 AU). This is also slightly closer-in than the equivalent distances for MS M-dwarfs (~ 0.5 AU) and considerably closer-in than those around B-type MS stars (~ 18 AU) (Dobos 2017). However, this alone does not provide much information on the proximity of the HZs to their respective Roche limits. Therefore, Eqn. (4) was similarly applied to the M_{WD} to obtain a value for the Roche limit of each WD. Then, each d_{HZ} was normalised to its corresponding R_{Roche}. From this, it was possible to define an Exclusion Zone where $d_{\mathrm{HZ}}/R_{\mathrm{Roche}} < 1$, as illustrated on the right land plot of Fig. 5. The planetary systems corresponding to any data-points below this value could immediately be discounted as uninhabitable as an Earth-analogue would be destroyed by tidal forces if within that HZ.

It can immediately be seen from Fig. 5 that only one WD HZ (WD 1136-286) from the data-set can be completely excluded. However, all HZs with $t_{\mathrm{cool}} > 1$ Gyr appear to be within an order of magnitude of their corresponding Roche limits. This makes Earth-analogues orbiting WDs within their HZs far more vulnerable to tidal destruction than Earth itself with respect to the Sun (~ 268 R_{Roche}).

It can be further noticed that the HZs decay exponentially with time, with the profile of Fig. 5 smoothing out the intrinsic scatter in Fig. 5 resulting from the spread in M_{WD}. The most significant consequence of this is that beyond 2 Gyr, the HZs stabilise; declining at a sufficiently slow rate for any (pre-)biotic evolution to remain largely uninterrupted. Only beyond 8 Gyr do these HZs drift dangerously close to the exclusion boundary. Thus, it appears that any lifeforms living on an Earth-analogue orbiting a WD would
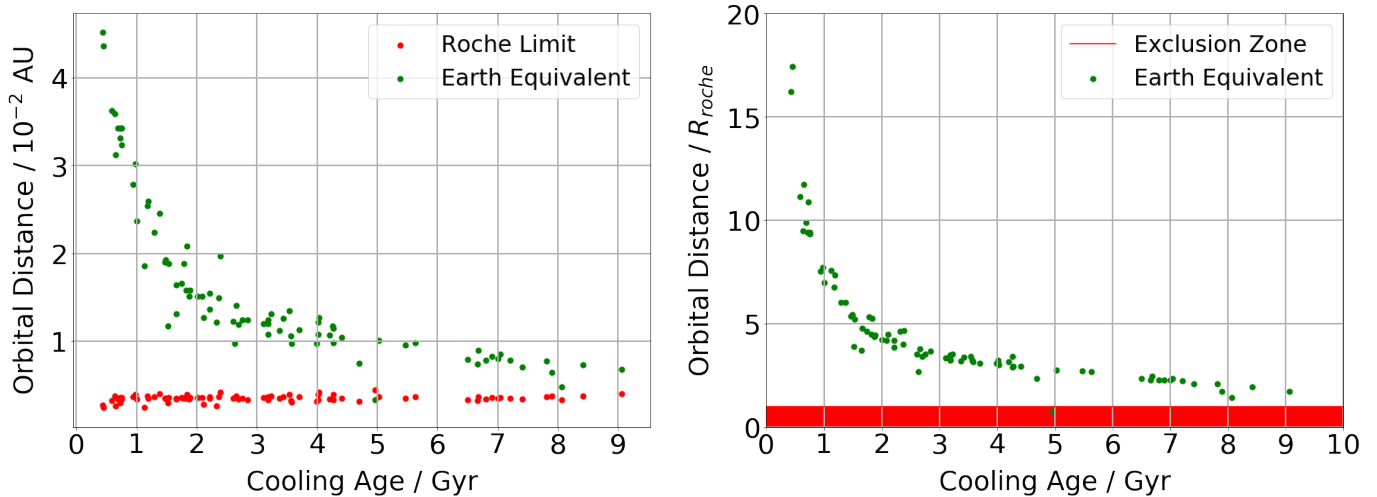
Fig. 5. Evolution of Earth-insolation distances for 83 WDs, each obtained by assuming Earth-equivalent flux ($S_{eff} = 1$). On the left hand plot, the true distances are given whilst on the right, all are normalised with respect to the corresponding Roche limits.

have at least 6 Gyr to be generated and evolve. Given that it has taken approximately 4 Gyr for life to evolve on Earth itself, the time constraints for life to evolve on a WD Earth-analogue are no more stringent. These findings corroborate those of Kozakis et al. (2018) who have argued that this maintenance of a continuous HZ, in combination with the absence of flare activity and the very high possible transit depths render WD planets to be excellent targets in the search for detectable life.

3.3. Implications of Climate Models

Now, instead of being modelled as a single distance for each WD, inner and outer HZ boundaries will be calculated so it can be seen how the range of distances defining the HZs vary with time. To achieve this, the parameter $S_{\odot}$ and the coefficients a through d in Eqn. 2 determined by Ramirez & Kaltenegger (2018) using climate models are used to define inner and outer HZ boundaries. In Section 3.3.1, the boundaries will only assume the presence of two greenhouse gases in the atmosphere of the hypothetical planet: water vapour (H_2O) and carbon dioxide (CO_2) in a similar manner to that of Kasting et al. (1993). These are the greenhouse gases that are most commonly used in defining the HZ and are therefore referred to as forming the *Classical Habitable Zone* by Ramirez & Kaltenegger (2018). In Section 3.3.2, the outer boundary of this zone will be extended to account for methane (CH_4) as a greenhouse gas. Extending the HZ by including methane was the primary purpose of Ramirez & Kaltenegger (2018). Here, that same extension will be applied to the 83 WDs from Dufour et al. (2017) to see by how much the HZs around WDs can be extended if an Earth-like planet has methane in its atmosphere. A bond albedo $\alpha \sim 0.31$ is assumed throughout in this Section; this is higher than the Earth's surface albedo (~ 0.2) as it accounts for the additional reflectivity and heating provided by clouds which are not specifically included in the radiative-convective climate models[19] of Ramirez &

Kaltenegger (2018). Finally, it should be noted that although Ramirez & Kaltenegger (2018) primarily intended their models to be used for main-sequence stars, they can also be used for WDs as Kozakis et al. (2018) have done. This is because the WDs cool down to 10^4 K very early on in their cooling tracks (see Fig. 3 in Section 2.2.1) and exhibit spectral energy distributions *broadly* resembling those of main-sequence stars: the main difference being the absence[20] of metallic spectral lines.

3.3.1. Classical Boundaries

The classical models of Ramirez & Kaltenegger (2018) assume the presence of three gases in the atmosphere of an Earth-analogue: molecular nitrogen, carbon dioxide and water. The latter two are crucially assumed to be responsible for the greenhouse effect; the mechanism of trapping radiation from the host star and therefore regulating heat on the planet. The inner edge of this classical HZ is therefore defined as the orbital distance at which an Earth-like planet would receive enough stellar flux to heat water to its critical point and trigger a runaway greenhouse effect. In other words, water would reach a temperature and pressure (647.096 K, 217.75 atm (Wagner & Pruß 2002)) above which it can only exist as a supercritical fluid, trapping even more heat than before and eventuating in the total desiccation of the planet as all water escapes into space. The outer edge of this classical HZ, meanwhile, is defined as the orbital distance at which an Earth-like planet would not receive enough stellar flux for sufficient carbon dioxide to function as a greenhouse gas. In other words, the surface temperature would be low enough for carbon dioxide to condense and also to scatter more radiation than it could absorb. This is also known as the maximum greenhouse limit of carbon dioxide (Kasting et al. 1993; Ramirez & Kaltenegger 2018). Keeping in mind these definitions of

---

[19]See Section 2 of Ramirez & Kaltenegger (2018) for more details than have been specified in this thesis.

[20]Unless it is a polluted WD, in which case the spectral energy distribution should still be more pristine that a main-sequence counterpart.

the HZ boundaries, the aim of this section is to model their time evolution in the WD dataset of Dufour et al. (2017).

For implementing these conditions to the dataset of WDs, the effective flux, S_{eff} received by each WD is modelled using the parameterisation of Ramirez & Kaltenegger (2018). Specifically, Ramirez & Kaltenegger (2018) ran a climate model that determined the effective fluxes, S_{eff} incident on an Earth-like planet necessary to reproduce surface temperatures that would either result in a runaway greenhouse effect (inner HZ edge) or result in the carbon dioxide reaching its maximum greenhouse limit (outer HZ edge). These fluxes varied depending on the effective temperature of the host star T_{eff}. They then fitted the profile $S_{\mathrm{eff, planet}}(T_{\mathrm{eff, star}})$ with a fourth-order polynomial[21] (Eqn. 2) of which the coefficients a through d varied depending on the HZ boundary in question. In this case, they used a single-column radiative-convective climate model which assumed the presence of carbon dioxide, molecular nitrogen and water vapour abundances[22] expected at the inner and outer HZ boundaries. This model did not include the specific effects of clouds and planetary rotation rates but did set a surface albedo $\alpha = 0.31$, higher than that of the Earth (~ 0.2) that would be expected from the reflectively and heating effects clouds. Now, in the context of Section 3 of this thesis, the models of Ramirez & Kaltenegger (2018) were applied by using their coefficients[23] in Eqn. 2 to find S_{eff} and then substituting this value into Eqn. 3 to calculate the corresponding HZ boundary. Using this method, the inner and outer HZ boundaries were calculated for all 83 WDs obtained from Dufour et al. (2017). These results of these calculations performed in Python are plotted in Fig. 6. As can be seen in Fig. 6, the Earth equivalent HZs run very close to inner HZ estimates (Leconte et. al) beyond $\sim 1.7\,\mathrm{Gyr}$ and only exhibit a very slight bifurcation at younger cooling ages. This implies that a very precarious balance between the orbital distances required to attain the insolation equivalent to that which Earth receives from the Sun and that required to trigger a runaway greenhouse effect. Though this inner edge is exactly in proportion with those Ramirez & Kaltenegger (2018) find for main-sequence stars, the distances are much smaller here ($\sim 10^{-2}\,\mathrm{AU}$). Since WD planetary systems should generally comprise planets inherited from the WD's progenitor, their masses have no reason to differ. Bearing these two considerations in mind, an Earth analogue orbiting in the Earth equivalent HZ would be much more vulnerable to experience a runaway greenhouse effect in the event of a dynamical perturbation (ie. by a massive planet such as WD 1856b). For the outlier, WD 1136-286, the inner boundary also lies below the exclusion boundary (as would be

expected) whilst its outer boundary lies just above. In general, the outer HZ boundaries (CO_2 Maximum Greenhouse) allow for fairly liberal HZs. Therefore, it seems that most systems would need to have an Earth-analogue closer to the outer edge of the HZ for it to be safe from a runaway greenhouse effect.

3.3.2. Methane Extension

In light of the vulnerability to tidal disruption that planets in WD HZs experience (mentioned in the previous paragraph), it is logical to see if there is a way to extent the classical outer HZ boundaries found in the previous section. This can be achieved by invoking methane (CH_4) as a greenhouse gas in addition to the two greenhouse gases used to determine the classical HZ boundaries: carbon dioxide and water vapour. This could permit a wider HZ than that shown in Fig. 6 by extending the outer HZ boundary. In fact, it has been hypothesised that methane was present in the early atmosphere of Earth, allowing the surface to be at least as warm as today in spite of the Sun being fainter and the insolation of Earth therefore being lower (Pavlov et al. 2000). Therefore, the aim of this section is to assess the maximum extension to the WD HZ boundaries shown in Fig. 6 that could be achieved by additionally invoking methane as a greenhouse gas.

Although Ramirez & Kaltenegger (2018) presented the revised coefficients for the classical HZ boundaries that were used here in Section 3.3.1, their article principally focused on models in which they additionally used methane as a greenhouse gas. Specifically, they modelled the effect of methane as a greenhouse gas by including it in the climate models mentioned in the previous paragraph, in various concentrations, with the maximum being equivalent to 10% of that of carbon dioxide. After applying their models to main-sequence stars, they found that the inner HZ boundaries are relatively unaffected[24] whilst for stars with $T_{\mathrm{eff}} \sim 4500\,\mathrm{K}$, the outer HZ begin to move outward and for stars with $T_{\mathrm{eff}} \sim 10\,000\,\mathrm{K}$, the HZ could increase by over 20%. They also note that for stars with $\sim 2600\,\mathrm{K}$, methane causes an anti-greenhouse effect as a greater proportion of the incident stellar flux would be at redder wavelengths whereby methane would absorb the starlight before reaching it could reach the planetary surface. Thus, the HZs would be narrower for cooler stars. The same pattern is to be expected here for WDs: the change in outer HZ boundary being larger for younger, hotter WDs and smaller for older, cooler ones. Similarly to those for the classical HZ boundaries, the coefficients for the methane ones were presented in Table 1 of Ramirez & Kaltenegger (2018). They are applied here to the WD dataset obtained from Dufour et al. (2017) using exactly the same method stated in Section 3.3.1. Given that the goal of this section is to assess the maximum extension of the HZ boundaries, only the coefficients corresponding to the maximum methane concentration are used; that is, 10% of the carbon dioxide (CO_2) abundance. As Ramirez & Kaltenegger (2018) noted that the inner boundaries remained unchanged, only the outer

---

[21]This is because Ramirez & Kaltenegger (2018) found that it provided the best parameterisation for the dependence of S_{eff} on T_{eff}.

[22]See Ramirez & Kaltenegger (2018) for the actual abundances.

[23]See Table 2 in Ramirez & Kaltenegger (2018): the values for $S_{\odot}, a, b, c$ and d used in this thesis are listed under the column Leconte et al. for the inner boundary and under the column CO_2 Maximum Greenhouse for the outer boundary. 'Leconte et. al.' in this case refers to the fact that Ramirez & Kaltenegger (2018) calculated their inner HZ boundary by rescaling that of Kopparapu et al. (2013) by a factor proportional to that found by Leconte et al. (2013).

[24]Due to higher water vapour concentrations which make the addition of methane as a greenhouse gas redundant.
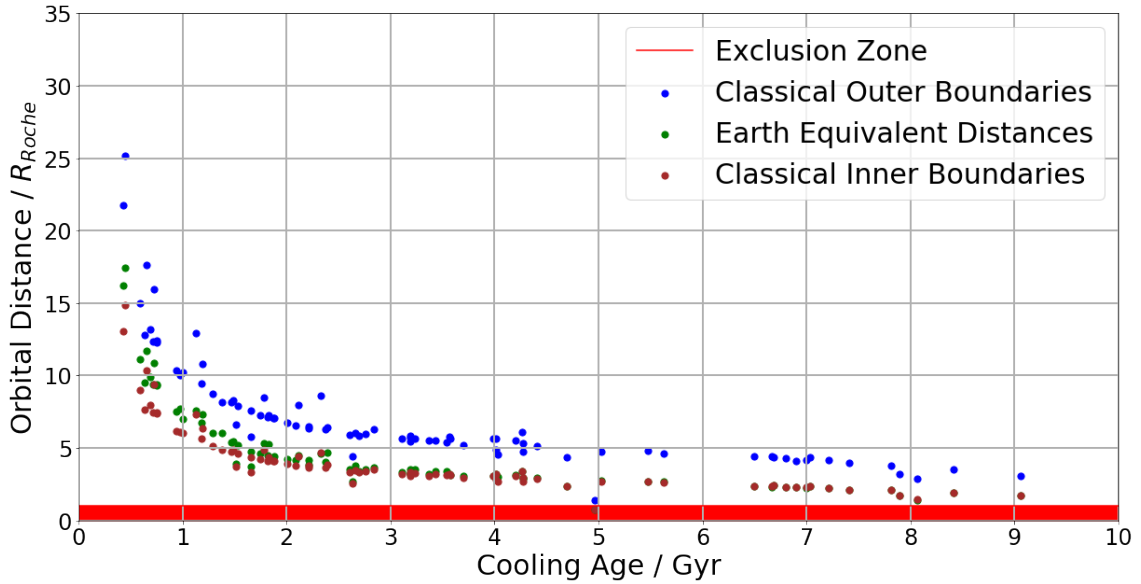
Fig. 6. Habitable zone evolution for 83 white dwarfs comparing the classical habitable zone boundaries to orbital distances equivalent to that of Earth in terms of the incident stellar flux.

boundaries are being changed here. The results are plotted in Fig. 7 alongside the classical boundaries obtained previously. The percentage changes with respect to the classical outer HZ boundaries are plotted in Fig. 8. As is expected, the outer HZ boundaries increase the most ($\sim 1\,\mathrm{R_{Roche}}$) at younger cooling ages, when the corresponding WDs are hotter: the maximum outer HZ boundary changes ($\sim 20\%$) occur at cooling ages $< 1\,\mathrm{Gyr}$. For all WDs older than $\sim 4.5\,\mathrm{Gyr}$, this value drops below 10%. It becomes negligble by $\sim 6.5\,\mathrm{Gyr}$, dropping below 5%. The anti-greenhouse effect found for HZs around main-sequence stars by Ramirez & Kaltenegger (2018) only applies for the older WDs in the here, with 6 of the 83 having their HZs shrunken. Very few WDs have had sufficient time to cool to these temperatures so the anti-greenhouse effect is not yet of *much* importance to the HZs of WDs.
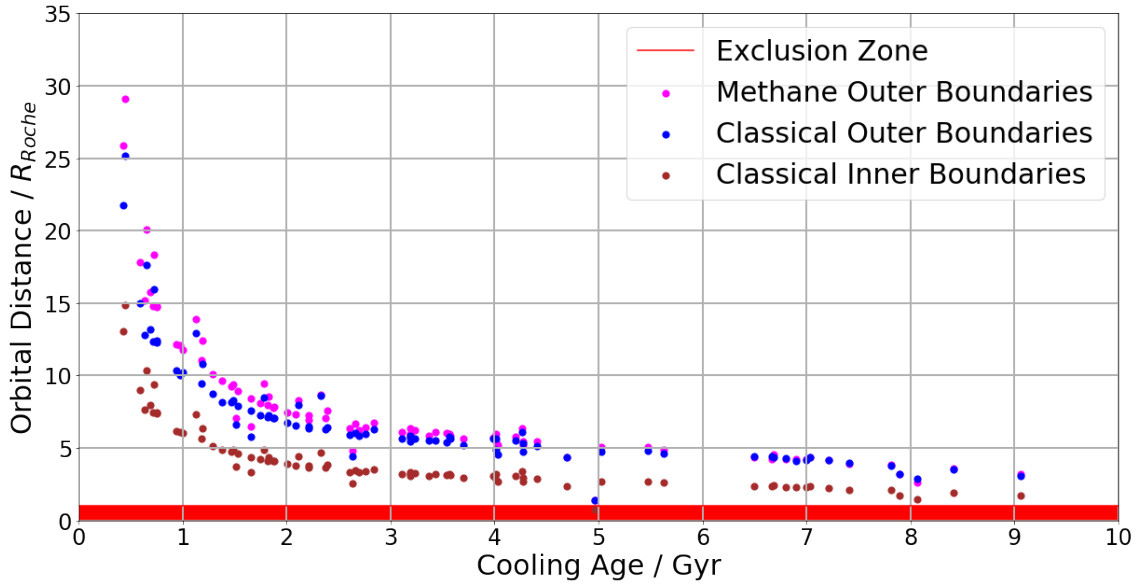
Fig. 7. The classical HZ boundaries plotted alongside the maximum methane extension to the outer boundaries. Here the methane abundance is assumed to be 10% that of carbon dioxide.
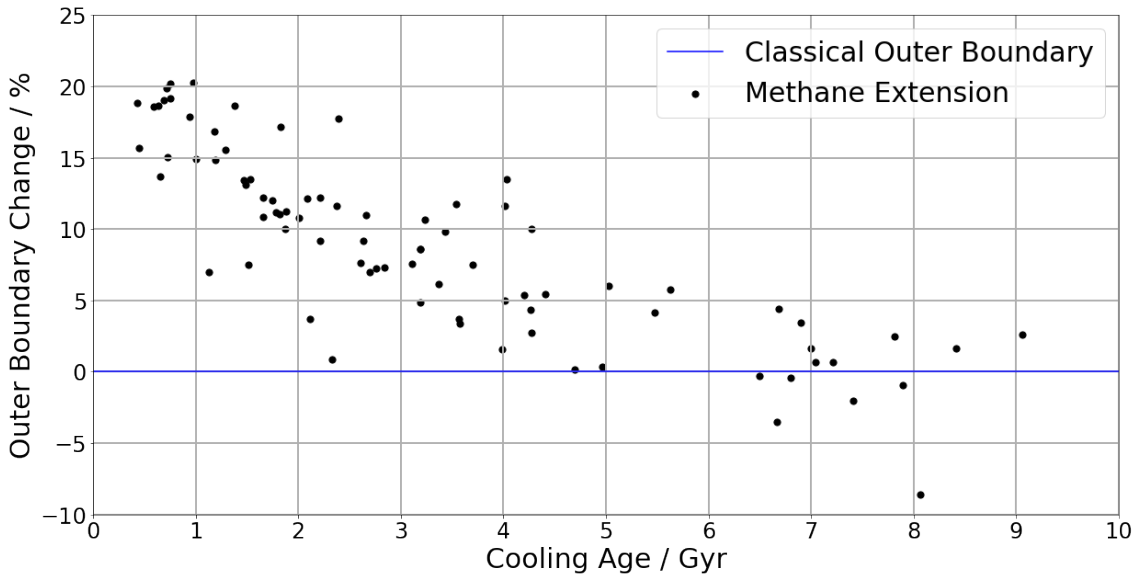
Fig. 8. The percentage change of the classical outer HZ boundary when methane is invoked as a(n) (anti-)greenhouse gas, when it is assumed to have an abundance 10% that of carbon dioxide.

4. The Prebiotic Chemistry of Circumstellar Envelopes

Before leaving behind its remnant core as a white dwarf, a main-sequence star undergoes considerable expansion and in the process loses up to 70% of its mass (Weinberger & Kerber 1997). As a result of this mass loss, a circumstellar envelope is formed wherein many of the atoms formerly fused in the stellar interior either coagulate and condense into dust grains or are synthesised into gas-phase molecules (Habing & Olofsson 2013). Given that these circumstellar envelopes eventually disperse into the interstellar medium (Van de Sande et al. 2019), the chemistries of any planets in the vicinity are bound to be affected too. Given that the fundamental atomic constituents of biological molecules: carbon, hydrogen, nitrogen, oxygen, phosphorous and sulphur are all present in circumstellar envelopes, this section treats the extent to which their molecular inventories may be considered prebiotic. To this end, Section 4.1 describes the main phases of stellar evolution with an emphasis on intermediate[25] mass stars; Section 4.2 discusses how the general compositions of these envelopes vary depending on the progenitor's mass, and Section 4.3 introduces a simple framework for defining and ranking the extent to which molecules can be considered prebiotic, allowing for a meaningful analysis of specific molecules that have been identified in circumstellar envelopes. This will provide the basis for assessing the prospect of abiogenesis in Section 5.

4.1. Stellar Evolution

After a $0.8\,\mathrm{M_\odot} < M < 8\,\mathrm{M_\odot}$ star runs out of hydrogen in its core, it fuses consecutively heavier elements[26] until the core is mostly comprised of carbon and oxygen or oxygen and neon if $M > 7\,\mathrm{M_\odot}$. These compositions reflect the heavier products of nuclear reactions[27]. Whilst consecutively heavier elements are being fused in the core, the outer layers of the star expand. In the process, the star leaves the Main Sequence (MS) of the Hertzsprung-Russell Diagram and progresses across the Sub Giant, Red Giant and Horizontal Branch until reaching the Asymptotic Giant Branch. This circumstellar environment in this evolutionary phase and those that immediately follow it will form the focus of this section as they are likely to be the most influential in that of the White Dwarf (WD) that is left behind. In particular, the circumstellar chemistry will be analysed in terms of its relevance to the origin of life in order to inform a conclusion and discussion on the likelihood of life evolving on an Earth-like planet orbiting in the Habitable Zone (HZ) around a WD. Before this, however, an outline will be given of the three phases of stellar evolution that immediately precede that of a WD: the Asymptotic Giant Branch (AGB), Protoplanetary Nebula (PPN) and Planetary Nebula (PN). This is to establish a physical timeline of stellar evolution that will be referred back to in discussing the chemical evolution of the Circumstellar Envelope (CSE).

4.1.1. Asymptotic Giant Branch

Upon the conclusion of the horizontal branch, all the He in a star's core is depleted and a heavier carbon and oxygen (or oxygen and Ne) remains. This increased mass causes the core to contract under its own self-gravity. In the process, its temperature increases and kinetic energy is liberated to the surrounding envelope. This permits He fusion to occur in a shell surrounding the core, using He ash generated in an outer H-burning shell present since the red-giant branch. The expansion of this new He-burning shell eventually results in it reaching the star's hydrogen envelope, eventuating in an instability at the interface whereupon the energy generated in He fusion precipitates rapid and cataclysmic hydrogen fusion (Habing & Olofsson 2013). This event is known as the He-shell flash or Thermal Pulse (TP) and divides the AGB phase into two sub-phases: the early-AGB (E-AGB) phase lasting $\sim 0.6 - 12\,\mathrm{Myr}$, where the He-shell is still expanding and the Thermally Pulsing AGB (TP-AGB) lasting $0.5 - 2.2\,\mathrm{Myr}$ in which the star experiences oscillatory changes in its volume and a series of rapid fusion reactions (Vassiliadis & Wood 1993). In the process of expansion, AGB stars can exhibit radii of up to $215\,\mathrm{R_\odot}$ wherein the gravity felt by the outermost shell is significantly reduced with effective temperatures of $\sim 3000\,\mathrm{K}$ (Vassiliadis & Wood 1993).

4.1.2. Protoplanetary Nebula

PPN are generally defined as the evolution phase wherein the central star has stopped significantly losing mass on the AGB but has not yet evolved to emit a sufficient number of photons above the Lyman limit ($912\,\text{Å}$) to ionise the CSE (Kwok 2007). As partially indicated in the conclusion of the previous paragraph, these objects exhibit strong infrared excess and carbon monoxide emission resulting from circumstellar dust and molecular excitations. Additionally, there should be evidence of the dust envelope being detached from the photosphere of the progenitor which observationally, is indicated by a double-peaked Spectral Energy Distribution (SED) corresponding to the initial emission from the central star and the absorption and re-emission by the envelope (Kwok 2007). Due to their spectral features being in the far infrared (far-IR) and their lack of line emission, PPN can only be identified by scattered light and were not discovered in any significant quantity until the advent of the Infrared Astronomical Satellite (IRAS) in 1983 (Kwok 1993). The timescale of this evolutionary phase is short at $\sim 10\,000\,\mathrm{yr}$ and is usually defined as the point at which the central star reaches $30\,000\,\mathrm{K}$ and is therefore able to emit the Lyman-continuum (Lyman-C) photons that can ionise the surrounding gas. If this transition does not take place within $10\,000\,\mathrm{yr}$, the envelope disperses too much for a PN to be formed (Volk & Kwok 1989).

---

[25]Here, intermediate mass is taken to signify $0.8\,\mathrm{M_\odot} < M < 8\,\mathrm{M_\odot}$: that is, it massive enough to become an asymptotic giant branch star but not massive enough to eventuate in a supernova.

[26]See Chapter 6.7, LeBlanc (2011) for the basic fusion reactions and their products or Iliadis (2015) for a more comprehensive treatment.

[27]eg. $^{12}\mathrm{C} + {}^{4}\mathrm{He} \rightarrow {}^{16}\mathrm{O} + \gamma$ and $^{12}\mathrm{C} + {}^{12}\mathrm{C} \rightarrow {}^{20}\mathrm{Ne} + {}^{4}\mathrm{He}$

4.1.3. Planetary Nebula

For cases in which the mass envelope of the AGB does not disperse within the $10\,000\,\mathrm{yr}$ timescale of the PPN, Lyman-C photons emitted by the $30\,000\,\mathrm{K}$ central star inaugurate an ionisation front. As a consequence, the free electrons of which former atoms are divested provide a pool of kinetic energy from which heavier atoms and ions can be collisionally excited. Then, spontaneous emission from the various excited species gives rise to their characteristic emission-line spectra responsible. The evolution of the central stars of PNe significantly influence that of their surrounding nebulae. When the remainder of the hydrogen envelope is just $\sim 1 - 10\%$ of the star's total mass, it shrinks but it still able to maintain temperatures for fusion reactions by virtue of its gravitational potential energy. In the process, the luminosity remains constant at $\sim 10^{-4}\,\mathrm{L_\odot}$. When the envelope mass is depleted to $< 10^{-4}\,\mathrm{M_\odot}$, the H-burning is no longer sufficient to maintain this luminosity and the star begins the cooling track to the WD phase (Kwok 2007). It was established by Paczynski (1971) that the envelope would need to have a mass $M < 4 \times 10^{-16}\,\mathrm{M_\odot}$, from which Iben Jr & Renzini (1984) were able to constrain a fading time for H-burning models given by $\sim 1.6 \times 10^4 (0.6\,\mathrm{M_\odot}/M_e)^{10}$ where M_e is the envelope mass. For typical core masses of $0.6\,\mathrm{M_\odot}$, this timescale is on the order of $\sim 10\,000\,\mathrm{yr}$.

4.2. Circumstellar Envelopes

There are in fact two classes of CSEs: those emanating from AGB stars with $(M < 1.5\,\mathrm{M_\odot}$ and $M > 4\,\mathrm{M_\odot})$ that are oxygen-rich and those emanating from AGB stars with $(1.5\,\mathrm{M_\odot} < M < 4\,\mathrm{M_\odot})$ that are carbon-rich (García-Hernández & Manchado 2016). There are two main reasons for the differing compositions: the synthesis and transport of carbon-rich and s-process[28] elements through the aforementioned convection zone induced by thermal pulsations is sufficiently great for stars with $1.5\,\mathrm{M_\odot} < M < 4\,\mathrm{M_\odot}$ that the envelope becomes C-enriched; for stars with $M < 1.5\,\mathrm{M_\odot}$, this convective mixing is insufficient whilst for those with $M > 4\,\mathrm{M_\odot}$, Hot Bottom Burning (HBB) is activated which converts carbon to N via the CN-cycle and eventually reconverts the carbon-rich envelope to an oxygen-rich one (Garcia-Hernandez et al. 2013; García-Hernández & Manchado 2016). The compositional differences of these envelopes will be discussed at length before being considered in the context of proto-biology. The chemical evolution of each type of envelope will be considered throughout the AGB and PN phases.

4.2.1. Carbon-rich Envelopes

Intuitively, it would seem that carbon-rich envelopes serve as better sources for life's chemical inventory. This is because hydrocarbon chains form the backbone for all complex biological molecules. The chemistry of these envelopes

is dominated by silicon carbide (SiC) and amorphous carbonaceous dust (García-Hernández & Manchado 2016). Importantly, the dust continuum emission also exhibits spectral features consistent with that of mixed aromatic and aliphatic structures resembling coal and kerogen (Kwok 2004). In this context, aromaticity signifies the formation of flat structure comprising cyclic hydrocarbons of which benzene (C_6H_6) rings form the units. Aliphatic compounds, by contrast, are hydrocarbons in which do not have a ring-like substructure. In general, organic compounds are limited to carbon-rich stars (Kwok 2004).

The most common solid-state condensate in carbon-rich AGB envelopes, principally found from its $11.3\,\mu m$ stretch mode is silicon carbide (Kwok et al. 1997). As the AGB evolves into a PN, the strength of silicon carbide feature declines suggesting that the circumstellar dust is increasingly dominated by amorphous carbon (Kwok 2004). This is likely due to the increase in mass loss rate which in turn increases the optical depth of the envelope into the PPN phase (Chan & Kwok 1990). Eventually, the Si budget is likely to be exceeded by that of carbon. Hence the silicon carbide spectral feature declines over time. In and of itself, this particular aspect of chemical evolution is unlikely to be important in the context of astrobiology. The main significance here is in the mass availability of reactive carbon which could be accreted by orbiting planets yet to facilitate life. Interestingly, the PN HU 2-1 exhibits a carbon abundance given by $\log[C] = 8.61$, very close to the solar value, $\log[C]_\odot = 8.67$. However, the C/O ratio is enhanced with respect to the solar one by a factor of 3 (Lutz 1981). Therefore, an undetected source of oxygen may be needed to facilitate the chemical evolution that gave rise to life on Earth. This could, of course, be supplied by volatile-rich asteroids and comets containing H_2O (Trigo-Rodríguez et al. 2019). In this scenario, the dynamical evolution that ensues due to planetary semi-major axis evolution and the presence of massive, Jupiter-like planets may facilitate a mechanism for delivery. Alternatively, volatiles such as H_2O may be outgassed from the mantle of terrestrial planets (assuming they are largely unchanged through stellar evolution) (Vulpius et al. 2020).

The aliphatic and aromatic structures are the most promising features of carbon-rich CSEs in the context of life and their presence detection through stretching and bending vibrational modes was unexpected (Kwok 2004). Infrared features at $3.3, 6.2, 7.7, 8.6, 11.3$ and $12.7\,\mu m$, collectively known as Aromatic Infrared Bands (AIBs) in PN NGC 7027 (Russell et al. 1977), provided the first indication of these modes being present (Duley & Williams 1981). These transitions emerge in PPN and have not been observed in stars of the AGB phase which is strongly indicative of photochemical processing during the transition between the two phases. Kwok (2004) argues that the formation of aromatic rings begins with the polymerisation of acetylene which by contrast is detected in AGB envelopes. The polymerisation proceeds with the formation of diacetylene (C_4H_2) and triacetylene (C_6H_2) of which benzene rings are constructed. In light of their detection of all three molecules in the PN, CRL 618, Cernicharo et al. (2001) suggest that the polymerisation is driven by the high UV flux from the central star and the shocks associated with high-velocity ($\sim 2000\,\mathrm{km\,s^{-1}}$) winds. They report these infrared bands as emanating from

---

[28]The slow neutron-capture process, constituting a seed nucleus successively capturing neutrons to form isotopes of higher masses, over a timescale of $\sim 10^4\,\mathrm{yr}$.

a region with $T_{\rm kin} \sim 200 - 250\,{\rm K}$ which they attribute to be a dense torus encircling the central star. This was the first detection of benzene outside of the solar system.

4.2.2. Oxygen-rich Envelopes

In contrast to carbon-rich AGB envelopes, oxygen-rich ones are rich in amorphous silicates together with weak crystalline features of pyroxenes and refractory oxides such as corundum and spinel (Waters et al. 1996). Despite their chemistries by definition being dominated by oxygen-rich silicates, carbonaceous species have been found oxygen-rich AGB and Post-AGB stars. This includes small molecules such as carbon monoxide, hydrogen cyanide (HNC) and cyanide (CN) but surprisingly also larger ones such as buckminsterfullerene (C_{60}) and the aforementioned aromatic features associated with Polycyclic Aromatic Hydrocarbons (PAHs) (Li et al. 2016; Gielen et al. 2011). Gielen et al. (2011) also report the detection of narrow but strong emission lines consistent with gas-phase carbon dioxide in IRAS 06338 and HD 52961. In light of their detection of larger carbonaceous molecules within their spectra of IRAS 06338, HD 52961 and EPLyr, they propose two possible formation mechanisms: the photodissociation of carbon monoxide molecules X-rays emitted within shocks (Woods & Nyman 2005), and the Fischer-Tropsch catalysis mechanism wherein hydrocarbons and H_2O are constructed from carbon monoxide and molecular hydrogen (Fischer & Tropsch 1926). However, they also allow for a scenario whereby strong pulsations permit the easy mixing of different layers of the stellar photosphere (Van Winckel et al. 1999, 2009). This latter scenario serves to elucidate the reality of an ill-defined boundary between carbon-rich and oxygen-rich envelopes. There are in fact transition objects characterised by features consistent with both (Perea-Calderón et al. 2009). This is by virtue of the observational distinction of the two envelope types, defined by the spectroscopically inferred C/O ratio.

In light of the detection of carbonaceous species in oxygen-rich envelopes, it can be concluded that any discussion of prebiotic chemistry from the AGB through to PN evolutionary phases should not be limited to carbon-rich ones. The main consideration to bear in mind when investigating oxygen-rich PNe in terms of their relevance to prebiotic chemistry is whether carbonaceous macromolecules could be delivered in sufficient quantities to an Earth-analogue. Otherwise, an endogenic source of carbon would need to be invoked to provide the necessary hydrocarbons for carbon-based lifeforms to emerge. That said, the definitive confirmations of simple carbonaceous molecules (and others relevant to life) do not appear to differ largely in the two cases. Therefore, the following section will introduce a formalism for assessing the relevance of molecules observed through the AGB and PN phases to the emergence of life without emphasis on the dominant chemistry of the source.

4.3. Prebiotic Molecules

Now that the overall compositions of carbon- and oxygen-rich envelopes have been considered, observational data of molecules present in AGB stars, PPNe and PNe will be examined. Specifically, this section aims to evaluate whether molecules relevant for life can be found in their concomitant CSEs. To this end, Section 4.3.1 introduces the concept of prebiotic chemistry and proposes a framework for formalising this loosely defined concept. Then, in Section 4.3.2, molecules that have been found in CSEs are tabulated and ranked according to this framework. Given that there is currently no central repository for such data, all the molecules that will be listed are those that have been found from specific papers. This list of prebiotic molecules will then serve to inform a discussion in Section 5.2 of what possible reactions between these molecules could result in the synthesis of more complex molecules vital to evolution of life such as amino acids and carbohydrates. Thus, it will be seen to what extent CSEs can supply the material needed for life to evolve in late stellar evolution.

4.3.1. Formal Definition

There is no formal definition of prebiotic chemistry. According to Cleaves (2012), it tends to be practically defined as "naturally occurring, mainly organic chemistry found in planetary or other Solar System environments which may have contributed to the origin of life on Earth, or elsewhere". What is clear, however, is that six elements: carbon, hydrogen, nitrogen, oxygen, phosphorous and sulphur are found in the vast majority of living organisms and that there are four types of *biological* molecule: carbohydrates, proteins, lipids and nucleic acids (Cockell 2020). From this, the definition of a prebiotic molecule can be constrained to any molecule that bridges the gap between the atoms of which biological molecules are comprised and the molecules themselves. Whilst this is still very general, it is a helpful starting point. For illustrative purposes, all molecules will be referred to by their chemical formulae in this section.

Next, a framework is necessary to rank the relevance of specific molecules to those of which life is constructed. Whilst a nucleotide may be considered an essential prebiotic molecule in the context of biochemistry, simple five-carbon sugars and α-amino acids are the most relevant molecules that have been detected in definitively exogenic material (eg. Furukawa et al. (2019)). In PNe and AGB stars by contrast, typical molecules include HCN, CO and various permutations of hydrocarbons. These alarming discrepancies in molecular complexity and structure yet arguable commonality in terms of fundamental atomic constituents call for a system which takes both of these facts into account. A crude yet workable framework that allows for this can be provided by enumerating the different interatomic bonds between[29] any of the six biological elements present in the molecule (without distinguishing double and triple bonds from single ones). For example, the OH group would be a level 1 prebiotic molecule in that a single bond binds oxygen and H; CH_4 would also be an level 1 molecule in that

---

[29]Bonds between two atoms of the same species do not count

only CH bonds are present; as would CO and CN given that only bonds between carbon and oxygenor carbon and N are present and no distinction is made for double or triple bonds. In contrast, the nucleotide dAMP contains OH, PO, CO, CH and NH bonds, and would therefore be a level 5 prebiotic molecule. An advantage of such a framework in the context of PNe is that organic macromolecules such as PAHs do not rank higher than Level 1 as CH bonds are the only bonds between different atomic species. In this regard, it is clear that PAHs are abiotic but could nevertheless be relevant to the emergence of life by virtue of the PAH world hypothesis (Trixler & Heckl 2009). Similarly, H_2O being classified as an level 1 molecule signifies that it is clearly abundant in the Universe and obviously not intrinsic to biology but nevertheless, an important solvent for all life on Earth. In other words, the presence of level 1 molecules in isolation does not mean much.

4.3.2. Prebiotic Molecules in Circumstellar Envelopes

Now that the loosely defined concept of a prebiotic molecule has been formalised, the number of different prebiotic molecules found in CSEs can be determined. Also, each molecule's level of prebioticity can be determined by applying the framework discussed above.

To date, there is no central publicly accessible database of AGB stars and PNe wherein the molecules detected have been included as a field, as Mass or Luminosity are in the *Montreal White Dwarf Database*. Therefore, all data collected in this thesis were obtained manually from tables listing molecules detected in AGB stars, PPNe and PNe in works by Bachiller et al. (1997); Willacy & Cherchneff (1998); Josselin & Bachiller (2003); Woods & Nyman (2005); Millar & Woods (2005); Ziurys (2008); Ziurys et al. (2009); Tenenbaum et al. (2009); Edwards et al. (2014); Schmidt & Ziurys (2018); Massalkhi et al. (2019); Massalkhi et al. (2020); Etmański et al. (2020) and Rao et al. (2020). The data were then tabulated in Google Sheets for simple calculations to be performed on the total number of Prebiotic Molecules found and their level or prebioticity. 80 different objects were sampled in total, all of which were found to have at least one level 1 or level 2 prebiotic molecule. Level 1 and 2 molecules that were found in at least one object are listed in Tables 1 and 2 respectively.

Molecule	Number
CCH	19
CS	57
CN	14
SO_2	22
SO	22
N_2H^+	22
NH_3	8
PN	3
CP	2
C_3N	2
C_5N	2
C_3H	2
C_4H	2
C_5H	2
C_6H	2
C_7H	2
C_8H	2

Table 1. Level 1 molecules that were present in at least two objects.

Molecule	Number
HCN	24
HNC	18
HC_3N	8
HCO^+	27
H_2CO	3
HC_5N	2
HC_5N	2
HC_7N	2

Table 2. Level 2 molecules that were present in at least two objects.

It is clear from Tables. 1 and 2 that simple prebiotic molecules are indeed abundant in evolved circumstellar envelopes. CS is by far the most common level 1 molecule in the dataset whilst HCO+ and HCN are the most common level 2 molecule. The presence of HCN in objects that have evolved into the PN phase (eg. Schmidt & Ziurys (2018)) also suggests that enough of it is able to survive dissociation reaction into CN and facilitate detection. CO is clearly missing from the Table 1. This is likely due to the fact that it is so abundant (Bujarrabal & Pardo 2007), that its presence was of little interest in most papers from which the molecular data were obtained. It is also evident that there is a great molecular diversity across AGB envelopes and PNe despite level 2 being the maximum detectable level of prebioticity. Now that a list of molecules commonly found in (post-)AGB objects has been established, potential routes for the synthesis of higher level prebiotic molecules can be discussed in Section 5. For this reason, Tables 1 and 2 will be referred back to throughout the next section.

5. Prospects for Abiogenesis

In light of the global compositions of circumstellar envelopes (CSEs) discussed in the previous section and the specific molecules present in Tables 1 and 2, initial constraints can be sought on the prospect of abiogenesis in late stellar evolution: that is, the prospect of life evolving in the planetary system of a star that has shed its mass envelope, leaving behind its remnant core as a white dwarf. There are two main considerations in this regard: firstly, whether the material synthesised in the circumstellar envelope can be delivered to a planet in the vicinity and secondly, how the molecules contained therein can evolve into the great diversity of molecules required to facilitate life. In line with those considerations, Subsection 5.1 models the maximum mass a hypothetical Earth-like planet could accrete from the circumstellar envelope of a given asymptotic giant branch star, and Subsection 5.2 explores how some of the molecules found in Tables 1 and 2 could be synthesised to make higher level prebiotic molecules more directly relevant for the emergence of life.

5.1. Planetary Accretion from the Circumstellar Envelope

In this section, a simple model is constructed that describes the mass of material that could be accreted by an Earth-like planet orbiting in the vicinity of a Circumstellar Envelope (CSE) at initial orbital distances corresponding to those of Saturn and the Kuiper Belt at the beginning[30] of the Asymptotic Giant Branch. The initial orbital distances of Saturn and the Kuiper Belt are chosen because Ramirez & Kaltenegger (2016) have found that these would be the least prone to atmospheric erosion from the ionising stellar winds during the Red Giant Branch (RGB) through to the Asymptotic Giant Branch (AGB) phases. Planets at closer orbital distances would need to acquire a secondary or even tertiary atmosphere to be habitable, which is beyond the scope of consideration in this thesis. To this end, Section 5.1.1 derives an equation that relates the mass loss rate of an AGB star to the accretion rate of a planet orbiting it at a given distance. Given that this accretion model would need to take account of the evolving orbital distances of planets in order to estimate the mass of material they could accrete, Section 5.1.2 presents a formula that relates the orbital distance of a planet to the mass loss by its host star. Then, Section 5.1.3 combines the formalism of the two preceding ones to estimate the total mass that Earth-mass planets beginning the AGB phase at the equivalent orbital distances of Saturn and the Kuiper Belt could accrete from CSEs throughout the AGB phase. These estimates build upon the work of Ramirez & Kaltenegger (2016) wherein AGB stars with Main-Sequence (MS) progenitors[31] of spectral classes G2 (ie. the Sun), F5, F1 and A5 are modelled. The aim of this accretion model is to determine how much material from an AGB CSE (containing prebiotic molecules) could be accreted by a planet that has not had most of its atmosphere eroded during the RGB and AGB phases of stellar evolution. This then motivates discussion of how the molecules CSEs contain could be synthesised to form higher level prebiotic.

5.1.1. Delivery of Envelope Material

Whilst the discussion of prebiotic chemistry in Sec. 4 addresses the origin of molecules that could facilitate abiogenesis, it does not determine how they could be transported to an orbiting planet. In fact, most of the discussion of AGB stars, PPNe and PNe in the context of astrobiology focuses on either the supply of complex organics to the Interstellar Medium (ISM) or to the Solar System. There appears to have been very little publicly-available research on whether material can be retained in the immediate vicinity. Therefore, a simple model amalgamating AGB mass-loss rates and Bondi-Hoyle-Lyttleton (BHL) accretion is invoked here to quantify this effect.

Following the formalism of Ramirez & Kaltenegger (2016) and Baud & Habing (1983), the mass loss rate of a star on the AGB phase can be quantified by

$$\dot{M}_{\text{AGB}} = -4 \times 10^{-13} \frac{M_i}{M_{\text{AGB}}} \frac{L_{\text{AGB}}}{g R_{\text{AGB}}} \tag{5}$$

where M_i is the initial stellar mass, g is the surface gravity and L_{AGB} is the luminosity of the AGB star whilst M_{AGB} and R_{AGB} are its mass and radius respectively. All values, including g are given in Solar units[32]. Typically $\dot{M}_{\text{AGB}}$ is expressed in $M_\odot \, \text{yr}^{-1}$. However, due to computing limitations, units of $M_\odot \, \text{kyr}^{-1}$ will be used in this thesis.

The BHL accretion rate modelling spherical gravitationally driven accretion onto a given mass, is approximated by

$$\dot{M}_{\text{BHL}} \approx \pi R_{\text{BHL}}^2 \rho v_o \tag{6}$$

where ρ is the ambient density, v_o is the velocity of the accretor relative to the medium or the local sound speed, c_s if $v_o < c_s$ and R_{BHL} is the Bondi radius in turn given by

$$R_{\text{BHL}} = \frac{2GM}{c_s^2} \tag{7}$$

with M being the mass of the accretor and c_s again being the local sound speed. As a simplification, it may be assumed that ρ solely comprises material ejected by the AGB star.

---

[30]The orbital distances of all planets increase as their star progresses along the red giant branch, horizontal branch and asymptotic giant branches. In terms of the stellar flux they receive, these starting orbital positions are equivalent to those that Saturn and the Kuiper Belt would have after migrating outward during the Sun's red giant phase.

[31]The spectral classes of stars actually change during stellar evolution. This is because the photosphere of the star cools as its radius expands. However, the spectral classes here are **not**

those of the AGB stars themselves. As in Ramirez & Kaltenegger (2016), they correspond to those that the AGB stars had whilst on the MS. This is because Ramirez & Kaltenegger (2016) model changing stellar parameters on earlier stages of phases of evolution as well. Given that many parameters used in this Section are obtained from Ramirez & Kaltenegger (2016), the same formalism is used.

[32]Here, g will be expressed in $R_\odot \, \text{s}^{-1}$ to maintain dimensional consistency with L_{AGB} and R_{AGB}.

From the definition of density and assuming that mass is ejected by the AGB star in spherically symmetric shells, it follows that

$$\rho = \frac{\mathrm{d}M}{\mathrm{d}t}\frac{\mathrm{d}t}{\mathrm{d}V} = \frac{\dot{M}_{\mathrm{AGB}}}{4\pi r^2 v_{\mathrm{shell}}} \tag{8}$$

where r is radial distance and v_{shell} is the radial velocity of the spherically symmetric shell of ejected material which has been obtained by differentiating r^3 in the $\mathrm{d}V$ term to obtain $3r^2\dot{r} = 3r^2 v_{\mathrm{shell}}$. Eqn. (8) can then be substituted into Eqn. (6) to obtain an equation linking the AGB mass-loss rate to the BHL accretion rate

$$\dot{M}_{\mathrm{BHL}} = \frac{1}{4r^2}\frac{v_{\mathrm{shell}}}{v_{\oplus}}R_{\mathrm{BHL}}^2\dot{M}_{\mathrm{AGB}} \tag{9}$$

where $v_{\oplus}$ is the orbital velocity ($\sim 10\,\mathrm{km\,s^{-1}}$) of an Earth-analogue and R_{BHL} of an Earth-analogue is simply given by

$$R_{\mathrm{BHL}} = \frac{2GM_{\oplus}}{c_s^2} \tag{10}$$

with $M_{\oplus}$ being the mass of the Earth.

Now whilst Eqn. (5) can be used to model the mass-loss rate for a given AGB star, c_s and v_{shell} both evolve with the orbital distance from an AGB star. This is owing to the fact that the expanding shell decelerates upon interacting with the surrounding medium and that the sound speed depends on the local temperature which decreases with distance from the star. The expanding shell is equivalent to a shock with velocity

$$v_s = v_s(r_s)\left(\frac{r}{r_s}\right)^{-1/2} \tag{11}$$

where $v_s(r_s)$ is the initial velocity at the radial position of the shock r_s (typically, $r_s = 1.2\,\mathrm{R_{AGB}}$) (Willson & Bowen 1984; Habing & Olofsson 2013). At the low densities found in the AGB atmosphere and circumstellar envelope (CSE), the sound speed can be treated as adiabatic so that

$$c_s = \sqrt{\frac{\gamma k T}{m_H \mu}} \tag{12}$$

where T is the local temperature and we can assume $\gamma \approx 5/3$ and $\mu \approx 1.4$. In the outer regions of the CSE (which are of interest here), the temperature is thought to follow a power-law with orbital distance $T(r) \propto r^{-\alpha}$ where $\alpha \approx 0.65$ (Habing & Olofsson 2013). Thus,

$$T = T_0\left(\frac{r}{r_0}\right)^{-0.65} \tag{13}$$

where for simplicity T_0 will be taken as the gas temperature at the start of excursion given by the photospheric temperature of the star [33]. Now that all the relevant equations have been defined, a simple model can be built to determine the radial evolution of accretion rates. By defining Eqns. (5), (9), (10), (11), (12) and (13) as functions in Python, a model could be constructed taking the following quantities as inputs:

- $v_{\mathrm{s}}(r, R_{\mathrm{AGB}})$ / $\mathrm{km\,s^{-1}}$: the shock (or shell) speed, dependent on orbital distance and the stellar radius
- $v_o \approx 10\,\mathrm{km\,s^{-1}}$: the likely orbital speed of the planet onto which material is being accreted (to be used if exceeding[34] the local sound speed)
- $R_{\mathrm{Bondi}}(c_s)$ / km: the Bondi radius, dependent on the local sound speed determined by Eqn. (12)
- $\dot{M}_{\mathrm{AGB}}(M_i, M_{\mathrm{AGB}}, L_{\mathrm{AGB}}, R_{\mathrm{AGB}})$ / $\mathrm{M_{\odot}\,kyr^{-1}}$: the AGB mass-loss rate, dependent on the AGB star's initial mass, and current mass, luminosity and radius
- r / AU: the orbital distance[35] of the accretor

Where necessary, the functions are defined to include unit conversions. Now, to illustrate the radial dependence of an Earth analogue's accretion rate for different spectral classes of AGB star, the maximum accretion rates can be plotted with respect to a range of orbital distances for a hypothetical Earth-mass planet. The maximum accretion rates refer to those that would be attained after each AGB star has reached its final mass, luminosity and radius. Here the same stars are modelled as in Ramirez & Kaltenegger (2016); namely, those of spectral classes G2, F5, F1 and A5. For this reason, the initial and final AGB masses for those spectral classes are obtained from Table A1, Ramirez & Kaltenegger (2016) and the final AGB radii are all approximated as 1 AU. The results are plotted in Fig. 9 with the accretion rate being expressed in mass units equivalent to Earth's atmosphere per thousand years, $M_{\oplus,\mathrm{atm}}/\mathrm{kyr}$. In this case the mass of Earth's atmosphere is assumed to be 5.136×10^{18} kg (Verniani 1966). This mass unit was mainly chosen in light of its numerical proximity to that of the mass accreted. The accretion rates in Fig. 9 exhibit functional forms as would be expected given the r^{-2} dependence of Eqn. 9. The earlier[36] spectral classes lose a greater proportion of their mass on the AGB and therefore have higher maximum mass loss rates. This is why their accretion rates are higher and decline faster at given orbital distances. The gaps between the spectral classes reflect the difference in their initial-final mass ratios, M_i/M_{AGB}.

5.1.2. Orbital Distance Evolution

Now that a model has been built to estimate the accretion rate at a given distance, the orbital distances of planets themselves have to be modelled. This is because the orbital distances of planets cannot be assumed to remain constant if their star is on the AGB branch; nor during the preceding RGB phase. Given that only the AGB is of interest in this thesis (owing to the compositions of their CSEs), initial orbital distances will be taken as those at the end of the RGB[37]. Following the formalism of Ramirez & Kaltenegger (2016), the orbital distance of a given planet in the AGB

---

[33] As indicated by the assumption of the power-law holding in the outer regions of the CSE, the behaviour is likely to be different in the inner regions. Therefore a different profile may be needed to model the shock along the beginning of its trajectory.

[34] In, this case v_o is approximately an order of magnitude above c_s. This can be verified by printing the values of c_s calculated in the code.

[35] If orbital distance evolution is accounted for, this is determined by Eqn. 14.

[36] Recall OBAFKGM: 'earlier' spectral classes correspond to letters that come 'earlier' in the sequence of letters.

[37] Assumed to be approximately the same as that at the beginning of the AGB.
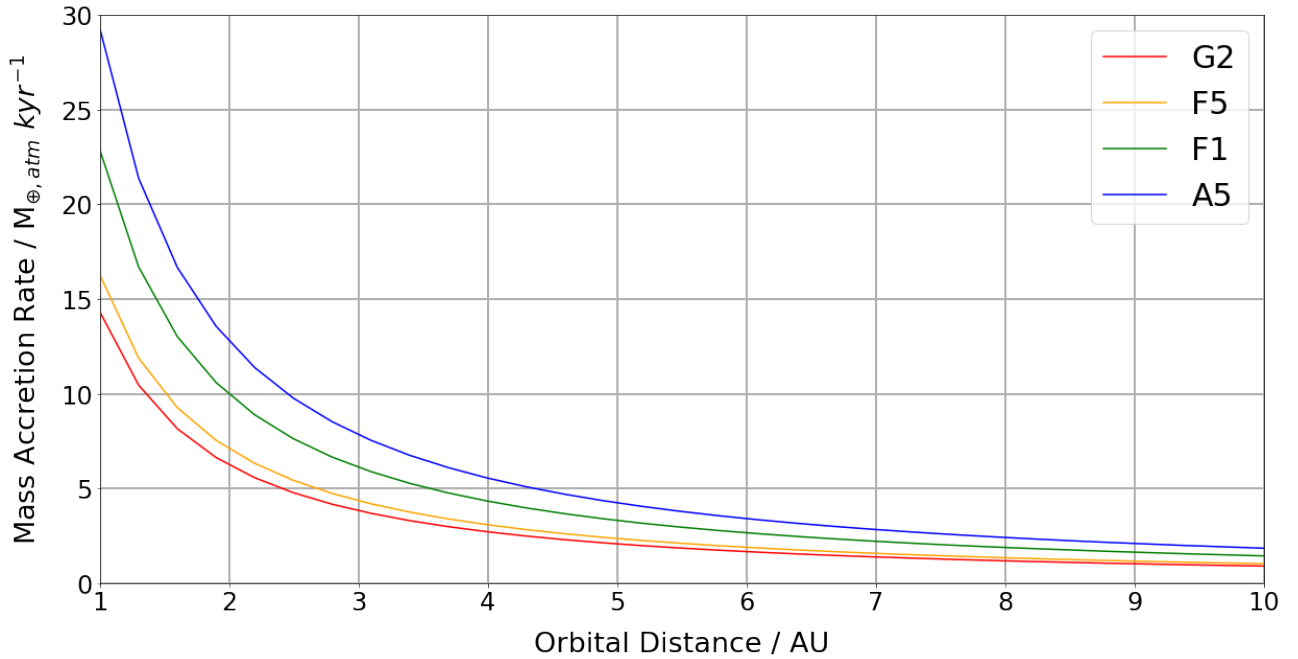
Fig. 9. The radial dependence of the accretion rates for a hypothetical Earth-mass planet. Each of the contours corresponds to an AGB of a different spectral class. These accretion rates correspond to each star's maximum luminosity, radius and mass loss rate. The units of the y-axis are Earth atmospheres per kiloyear. G2 (coloured in red) is the spectral class of the Sun.

phase is

$$D(t) = D_0 \frac{M_0}{M_{\mathrm{AGB}}} \tag{14}$$

where D_0 is the orbital distance at the end of the RGB phase, M_0 is the star's mass at the onset of the AGB and $M_{\mathrm{AGB}}(t)$ is the mass of the AGB star after losing a given quantity of mass[38]. Since directly modelling the atmospheric erosion of an orbiting planet is beyond the scope of this thesis, the results presented in Table A4 of Ramirez & Kaltenegger (2016) are used to inform the choice of initial orbital distances in this model. Specifically, those of Saturn and the Kuiper Belt are chosen, whereby more than 90% of a 1 bar atmosphere is retained for the MS spectral classes F5, F1 and A5. The G2 (solar) spectral class corresponds to 77.3% of a 1 bar atmosphere being retained. Given that the final orbital distances found using Eqn. 14 disagree with those found by Ramirez & Kaltenegger (2016) for this case, the G2 spectral class is omitted from further analysis anyway.

5.1.3. Masses Accreted from the Circumstellar Envelope

Now that the accretion rates have been determined as functions of orbital distance, it can be deduced what accretion rates would be present at the orbital distances an Earth-analogue would need to be at in order to experience negligible atmospheric erosion. As previously mentioned, these distances have already been determined by Ramirez & Kaltenegger (2016) and take account of orbital distance evolution. They find that an Earth-analogue (1 bar atmo-

sphere) would need to have initial orbital distances corresponding to the Kuiper belt for each of the aforementioned spectral classes to retain $\geqslant 97\%$ of the atmosphere. To estimate the total mass accretion, the r term in Eqn. 9 has to take account of orbital distance evolution given by Eqn. 14 and the changing mass loss rates. The time interval over which the orbital distance evolution and CSE accretion take place is determined by calculating the difference between the age of each spectral type at the beginning and end of the AGB. These values are presented in Table A1, Ramirez & Kaltenegger (2016). The values for the initial and final AGB luminosities and masses are also presented there. Because the mass loss rate and orbital distances are changing $M_{\mathrm{AGB}} = M_{\mathrm{AGB}}(t)$ in Eqns. 5 and 14. To simulate this, the number of steps is defined to be 20 000 for the G2, F1 and A5 spectral classes and 10 000 for the F5 spectral class. This quantity is used to define the number of time-, mass-, luminosity- and radius-steps for each case, implemented using `np.linspace` in Python. This number of steps is defined to ensure that timestep is 1 kyr in all cases. This timestep is chosen in consideration of the capacity of the computer being used to perform the calculations. F5 has a lower number of steps due to its shorter 10 Myr duration on the AGB, as opposed to the others which spend 20 Myr on the AGB. In all cases, the radii are assumed to vary between 0.8 1 AU whilst the masses and luminosities are assumed to vary between the values indicated by Ramirez & Kaltenegger (2016) in Table A1. In light of their atmospheric retention found by Ramirez & Kaltenegger (2016), the initial orbital distances are taken to be those equivalent (in terms of stellar flux received) to Saturn and the Kuiper belt at the beginning of the AGB phase (Table A2, Ramirez & Kaltenegger (2016)). Taking these values together with the initial AGB mass and the mass-grid as inputs, grids of orbital distances were determined for the Saturn and Kuiper belt analogues. The values for the final

---

[38]In Ramirez & Kaltenegger (2016), the same equation models the orbital distance through both the RGB and AGB.

orbital distances agree with those of Ramirez & Kaltenegger (2016) for the F5, F1 and A5 spectral classes but that of the Sun (G2) underestimates the final orbital distances for both the Saturn and Kuiper Belt analogues. Given that this would result in more of a 1 bar atmosphere being lost, the Sun is omitted as a model star in the estimation of total mass accretion. After the grids of orbital distances are calculated, they are used as inputs in all functions that take orbital distance as an input. This includes the mass accretion rates. Given that the timestep used in all calculations is defined to be 1 kyr and the accretion rates are calculated $M_{\oplus,\text{atm}}\,\text{kyr}^{-1}$, the total mass accreted in each case can be approximated calculated by summing all the values in the grid of mass accretion rates. The values obtained are presented in Table 3.

In Table 3, it can be seen that the planet with an initial orbital distance equivalent to Saturn accreted the more than the Kuiper Belt equivalent. This is obviously due to the decreasing accretion rates with orbital distance. As for spectral type, however, the F1 star appears to supply the most mass to its planets. This is due to the interplay of the orbital distance evolution and mass accretion rate. In the case of the A5 star, the higher overall mass loss rates are offset by the vast changes in orbital distance: 71.49 AU for the Saturn equivalent and 226.3 AU for the Kuiper Belt equivalent. Combining these two consideration, it can be seen that the Saturn equivalent orbital distance around the F1 star presents the ideal scenario. Compared to the Kuiper Belt equivalent, it trades 4.3% of its 1 bar atmosphere to accrete an extra mass of $14.9\,M_{\oplus,\text{atm}}$. That said, in all cases the mass accreted from the CSE exceeds the total mass of carbon on Earth (Clemente et al. 2015), $\sim 6.55 \times 10^{16}\,\text{kg} \sim 0.01\,M_{\oplus,\text{atm}}$ by at least two orders of magnitude. Therefore, even oxygen-rich CSEs such as that of the F5 star [39] are likely to be able to supply a sufficient mass of exogenic carbon for Earth-like masses to be attained (if not already present) and therefore, the basic abundance necessary for carbon-based lifeforms to evolve. That said, this alone does not say much regarding the presence of specific molecules necessary for life to evolve; a more detailed treatment is warranted on how basic prebiotic molecules found within CSEs could be synthesised into higher-level ones such as amino acids and simple sugars.

5.2. The Synthesis of Higher Level Prebiotic Molecules

In order to determine whether life is likely to evolve on the planet of a WD in light of the CSE of its progenitor, the three main types of prebiotic molecule found exogenically will be discussed: these are amino acids, carbohydrates and nucleobases. In this context, exogenic signifies that the molecules have either been found on meteorites or tentatively observed in the interstellar medium; that is, there is evidence to suggest they exist somewhere other than the Earth. Whilst these molecules alone are considerably simpler than those of which terrestrial lifeforms are comprised, they do represent the limitations to what is realistically de-

tectable in outer-space. Therefore, this subsection will focus on how amino acids, carbohydrates and nucleobases are relevant for life and how they may be constructed given the molecular inventory of CSEs established in Tables 1 and 2. Polycyclic Aromatic Hydrocarbons will also briefly be discussed as they have tentatively been detected in CSEs and they may serve as an important catalyst for the synthesis of prebiotic molecules. However, the construction of more complex molecules such as DNA, Lipids and Proteins themselves are beyond the scope of this thesis. The origin of life on Earth is a contentious topic, let alone the full set of variables governing the possibility of it arising on the planet of a White Dwarf. Instead, this subsection concerns the most basic molecular constraints for life and to what extent they can be accounted for by the molecules found in CSEs.

5.2.1. Amino Acids

In terms of biological molecules, amino acids form the sub-structure of proteins and are therefore essential to all known lifeforms. They comprise the NH_2 and COOH functional groups bonded to a side chain R which varies depending on the specific type of amino acid. Their significance in the context of astrobiology emanates from the fact that they have been found in exogenic material (as alluded to in Sec. 2): famously, in carbonaceous chondrites such as the Murchison meteorite (Cronin & Moore 1971; Furukawa et al. 2019). The detection of the simplest amino acid, glycine in the Interstellar Medium has (ISM) has been reported by Kuan et al. (2003). However, this claim is extremely controversial and it has been asserted its detection would be extremely difficult with existing instrumentation Lattelais et al. (2011). That said, given glycine's simplicity, modelling possible reactions for its formation from molecules found in CSEs presents a good first step for probing their prebiotic chemistries.

Of the high-frequency[40] molecules listed in Table 2, hydrogen cyanide (HCN) is arguably the most relevant for the synthesis of amino acids. This is by virtue of Strecker synthesis which permits the formation of an amino acid wherein hydrogen cyanide reacts with amine (NH_3) which happens to be found in eight objects (see Table. 1) and R-CHO (aldehyde):

$$HCN + R\text{-}CHO + NH_3 \rightarrow R\text{-}CH(NH_2)-COOH + NH_3 + H_2O$$
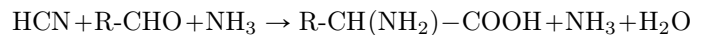
where $R\text{-}CH(NH_2)-COOH$ is an amino acid characterised by a functional group, R (Cockell 2020). The feasibility of this reaction in forming amino acids would be limited by the availability of aldehydes and amine. Given that amine is found in eight objects (see Table 1) and that formaldehyde (H_2CO) is found in three (see Table 2), it follows from taking $R = H_2$ that glycine (NH_2CH_2COOH) is indeed an amino acid that could be synthesised. That said, glycine is only one of the twenty-two amino acids required for the emergence of life (Cockell 2020). Aside from the chemistry of CSEs not being able to account for the full inventory of proteinogenic amino acids, there is not yet a clear consensus on whether the yields from Strecker synthesis could

---

[39]Its mass (also in Table A2, Ramirez & Kaltenegger (2016)) is $1.3\,M_\odot$. Following the arguments of Section 4.2, its envelope is likely to be O-rich.

[40]Found in larger numbers of objects.

Class	Saturn / $M_{\oplus,atm}$	r_i / AU	r_f / AU	Atm %	Kuiper Belt / $M_{\oplus,atm}$	r_i / AU	r_f / AU	Atm %
F5	15.4	20.4	36.7	92.0	3.9	64.3	115.7	99.0
F1	20.0	26.7	59	95.0	5.1	84.3	185.7	99.3
A5	7.6	43.0	115.0	98	1.9	135.3	361.6	100.0

Table 3. The total mass accretion of planets with orbital distances equivalent to those of Saturn and the Kuiper Belt. The corresponding percentages for initial orbital distance r_i, final orbital distance r_f and atmospheric retention, Atm (of a 1 bar atmosphere) are obtained from Tables A2 and A4 in Ramirez & Kaltenegger (2016).

have been sufficiently high for life to evolve the Early Earth, let alone whether the yields would be sufficient on a WD planet.

5.2.2. Carbohydrates

Carbohydrates, also known as sugars, are an important as an energy source for many living organisms and also for providing structural support. They consist of chains of monosaccharides, arranged in the generic form $C_m(H_2O)_n$ whereby each monosaccharide comprising this polymer has the form $(CH_2O)_n$ (with $n \geqslant 3$). These species have also been encountered in the context of exogenic material: common biological sugars such as ribose, arabinose, xylose and lyxose have been detected on the carbonaceous chondrites such as the Murchison meteorite (Furukawa et al. 2019). As for the ISM, the most sugar-like species that have been reported are glycolaldehyde[41] and dihydroxyacetone, which have been found in giant molecular clouds and in the vicinity of protostars (Jiménez-Serra et al. 2020). In CSEs, the most sugar-like species to have been detected is formaldehyde. However, the presence of more relevant molecules could be inferred by again, considering how they might be synthesised.

In a similar respect to that of hydrogen cyanide, the polymerisation of formaldehyde can lead to the formation of simple sugar-like species such as glycolaldehyde through the formose reaction (Cockell 2020). Again, the presence of formaldehyde suggests that this reaction could take place. However particularly high abundances are necessary for the polymerisation of formaldehyde into crucial sugars such as ribulose and ribose. Given that the abundance of formaldehyde on the Early Earth is poorly constrained, it is not known how important the formose reaction was in the emergence of life (Cockell 2020). In the context of CSEs, the low densities are unlikely to be able to facilitate such reactions. Therefore, although aldehyde itself may be formed in the circumstellar environment, further chemical evolution would likely need to take place on a planetary surface. A hydrothermal vent could be a likely site of such reactions (Kopetzki & Antonietti 2011).

5.2.3. Nucleobases

Nucleobases are the one of the monomers of which nucleic acids are composed, in addition to phosphate groups and nitrogenous bases. Nucleic acids, in turn carry genetic information and instructions for important biological processes such as protein synthesis. In terms of exogenic matter, uracil has been detected on the Murchison meteorite (Martins et al. 2008). Unlike amino acids and carbohydrates, however, nucleobases or their immediate precursors have not yet been detected in the ISM; rather its possible synthesis in the ISM has only been inferred using theoretical models (López-Tarifa et al. 2011). Therefore, this discussion will focus on how it may be synthesised from molecules present in CSEs.

It has been shown that HCN can also be a participant in the synthesis of nucleobases. Specifically, adenine may emanate from NH_3 and H_2O-catalyzed reaction pathways as modelled by Roy et al. (2007). Guanine synthesis meanwhile, may occur from the polymerisation of NH_4CN (Levy et al. 1999) which in turn can be constructed from reactions between CN^+, H^+ and NH_3^+ ions all found to exist within CSEs. In both cases of nucleotide synthesis, high concentrations of the reactants are needed. In the latter case, these can only be attained in frozen environments or an aqueous solution. If an Earth-analogue needs to be at orbital distances equivalent to Saturn or the Kuiper Belt to fully retain its atmosphere, it may well be conducive to such a reaction.

5.2.4. Catalysts: Polycyclic Aromatic Hydrocarbons

In addition to the ubiquity of hydrogen cyanide in CSEs, the aromatic spectral features indicating the presence of Polycyclic Aromatic Hydrocarbons (PAHs) may be relevant to the prospect of abiogenesis, Ehrenfreund et al. (2006) propose that PAHs provided essential catalytic surfaces for early self-assembly and synthesis of complex prebiotic molecules such as RNA. They invoke the stability and versatility of aromatic macro-molecules to suggest that PAHs effectively shielded the precarious reactants participating in proto-evolution.

---

[41]Glycolaldehyde is not a true sugar but often considered in the literature to be a sugar-like species (Carroll et al. 2010)

6. Discussion

Now that results have been obtained in each disparate section of this thesis, they need to be discussed in terms of their wider implications and synthesised to inform a tentative conclusion on the habitability of white dwarf planetary systems. Specifically, Section 6.1 reflects on the findings from Section 2 of this thesis on whether White Dwarfs could have Earth-like planets on which life could form; Section 6.2 discusses the results in Section 3 on whether White Dwarfs could sustain stable Habitable Zones (HZs) outside the Roche Limits (RLs) of Earth-like planets; Section 6.3 refers to Sections 4 and 5.2 to examine the extent to which the Circumstellar Envelopes (CSEs) of Asymptotic Giant Branch (AGB) are relevant in supplying nearby planets with the material needed for life to evolve into the White Dwarf (WD) phase, and Section 6.4 scrutinises the late circumstellar accretion model of Section 5.1 in terms of how this prebiotic material could be delivered. Considering all these points together will permit a tentative conclusion to be made on how conducive stellar environments after the AGB are to the evolution of carbon-based lifeforms.

6.1. Detectable Earth-like Planets around White Dwarfs

As has been found in Section 2, the spectroscopic data of polluted white dwarfs and circumstellar disks demonstrates that planets and planetesimals can exist well into the white dwarf phase. However, the low [Fe/Mg] ratios of polluted WDs shown in Fig. 4 and spectroscopic analyses of GD 362 and PG 1225-079 discussed in Section 2.3.2 are more consistent with the compositions of Solar System asteroids such as 16 Psyche, as opposed to Earth-like planets. As previously stated in Section 2.3.1, this is likely a consequence of lighter objects being more subject to dynamical perturbations from heavier planets. On the other hand, the transit detection of WD 1856b by Vanderburg et al. (2020) and the spectroscopic analysis of Gänsicke et al. (2019) reveal the presence of gas giants in the planetary systems of WDs. In the context of habitability, these may play a role in directing water contained within primitive planetesimals to Earth-like planets (O'Brien et al. 2014). That said, it seems that planets with physical parameters comparable to that of Earth (in terms of mass, density etc.) have yet to be discovered. From the finding of 2.2.2: that within 100 pc at most 15 Earth-radius planets are likely to transit their host WDs in the HZ, it follows that detecting Earth-analogues via transits alone would be extremely challenging. For Earth-radius planets at even larger orbital distances, the transit probabilities would be even lower owing to an increase in the denominator of Eqn. 1. In that regard, other detection methods may need to be utilised to increase the available sample of Earth-like planets. As the spectra of WDs do not exhibit many absorption lines, radial velocity measurements would not be a favourable alternative. Instead, direct imaging is likely to be the best bet. As Burleigh et al. (2005) have argued, WDs may in fact be excellent targets for direct imaging searches. This is owing to the fact that WDs are 10^4 times fainter than their main-sequence progenitors and therefore less likely to drown out the stellar flux reflected their planets. The advent of the

Extremely Large Telescope (ELT), planned for 2025 as of the 23rd of February 2021 (ESO 2021), may therefore be decisive in facilitating the detection of sub-Jovian planets. That said, Fossati et al. (2012) have indicated that finding them in the ~ 0.01 AU HZ is likely to be very challenging, even with the instrumentation of the ELT. They assert that similar obstacles would be encountered with microlensing. In spite of all these limitations, the fact that $R_\oplus/R_{WD} \sim 1$ for WDs signifies that the detection of (rare) transits is likely to be very rewarding as transit-depths could theoretically be as high as 100% for the case of perfect alignment. Kaltenegger et al. (2020) have shown with the instrumentation of the *James Webb Space Telescope* (JWST), the large transit signal could facilitate the detection of tentative biosignatures in transit spectroscopy, including those of methane (CH_4), ozone (O_3), molecular oxygen (O_2) and nitrous oxide (N_2O). Whether surface organisms could arise to produce them would principally depend on the habitable environment around a given WD.

6.2. Stable Habitable Zones around White Dwarfs

In general, Section 3 showed that WDs are capable of sustaining continuous HZs for periods of ~ 6 Gyr and for the vast majority of cases, outside the corresponding RLs for Earth-like planets. That said, the RLs being on the same order of magnitude as the HZs would still make Earth-like planets orbiting at these distances vulnerable to tidal disruption. To assuage this risk at cooling ages < 4 Gyr, methane can be invoked as a greenhouse gas as shown by Fig. 8. Given that it would only result in an anti-greenhouse effect after ~ 6.5 Gyr, its depletion in the atmosphere would not be necessitated on the timescales required for life to develop ~ 1 Gyr.

The one WD for which any HZ boundaries were within the RL was WD 1136-286. This is owing to it having a low luminosity ($10^{-4.94}$ L$_\odot$) with respect to its high mass (1.2 M$_\odot$). This is particularly odd given its relatively young cooling age of 4.94 Gyr: as indicated by Figs. 3, 6 and 7, a WD HZ would not be expected to coincide with an Earth-mass RL until at least ~ 8 Gyr into the WD phase. It appears that these parameters for WD 1136-286 were determined by Ruiz et al. (1995) wherein an erroneous argument was made for its young cooling age: that core crystallisation reduces the cooling timescales. This is in stark disagreement with most literature on the subject (eg. Tremblay et al. (2019)) and inconsistent with a well-established consensus in thermodynamics: that the latent heat of crystallisation slows and prolongs a given cooling process, thereby increasing cooling timescales rather than reducing them. In light of this, the wrong cooling track may have been applied to WD 1136-286.

Section 3 of this thesis did not account for the effects of tidal locking, tidal heating and Ultraviolet (UV) surface environments. Given the close-in ~ 0.01 AU distances of WD HZs, any planet orbiting in the HZ of a WD would be tidally locked. This follows from the fact that the HZ scales with luminosity whilst tidal effects scale with mass: for a WD, the latter is typically 10^{-4} L$_\odot$ whilst the former is ~ 0.6 M$_\odot$. Due to the relatively high mass with respect to this low

luminosity, frictional forces within a HZ planet would result in torques that induce a rotation rate synchronous to that of the host star (Barnes 2017). As a consequence, the day side surface temperatures may be above the boiling point of water whilst the night side could exhibit those below its freezing point (Hu & Yang 2014; Braam 2017). Such planets would need both atmospheric and/or ocean heat transport in order to facilitate habitable environments on large fractions of their surfaces. Furthermore, Barnes & Heller (2013) have modelled the effect of tidal heating on the HZs of WDs: they find that very low orbital eccentricities $10^{-4}-10^{-5}$ are needed to avoid a tidally-induced greenhouse effect. As for the UV surface environment, Kozakis et al. (2018) have shown that the atmospheric photochemistry of planets in a WD's continuous HZ would be very sensitive to changes in its WD's Spectral Energy Distribution. Namely, the ideal conditions for atmospheric shielding from harmful UVC radiation ($100 - 280\,\mathrm{nm}$) would occur at cooling ages of approximately $\sim 2.2\,\mathrm{Gyr}$ for a $0.6\,\mathrm{M_\odot}$ WD; whereby a 1 bar Earth-analogue would receive enough incident UV flux for the sufficient production of a shielding ozone (O_3) layer through the Chapman reactions, but not enough UV flux for its shielding effect to be offset by photolysis. This consideration is likely to be important in the context of surface organisms capable of producing detectable biosignatures. For a greater resilience to UV radiation, the habitability of non-Earth analogues could be considered: super-Earths with higher masses and thicker atmospheres. However, given that Earth is still the only available specimen for a habitable planets, those of other planet types remains an open question. That said, the circumstellar envelopes present in planetary systems directly before the WD phase are likely to impact the eventual habitability of all WD planets.

6.3. Prebiotic Molecules in Circumstellar Envelopes

In Sections 4 and 5.2, it was found that as far as spectroscopic observations of Asymptotic Giant Branch (AGB) stars, Protoplanetary Nebulae (PPNe) and Planetary Nebulae (PNe) go, the CSEs that permeate their circumstellar environments do possess the most basic molecules (ie. HCN) relevant for the synthesis of the more biologically relevant, amino acids, carbohydrates and nucleobases. Whilst it was shown that glycine could theoretically be synthesised in these environments through reactions such as Strecker synthesis, the exact physical conditions necessary for such reactions to proceed was not considered. In that regard, there seems to be a dearth of literature on whether CSEs could facilitate these conditions. At the time[42] of writing, the most relevant and publicly accessible research concerns the possible formation of glycine through the condensation of atomic carbon at low interstellar temperatures (Krasnokutski et al. 2020), and the possible Strecker synthesis of aminoacetonitrile in cometary environments (Danger et al. 2011). However, Lattelais et al. (2011) have indicated that considerable challenges remain in definitively identifying species such as glycine in the interstellar medium. The same limitations would certainly apply to their identification in CSEs.

There is still alot of debate regarding exactly how life arose on Earth: authors such as Harrison & Lane (2018) forward an endogenic model with biological evolution arising from the chemical gradients of alkaline hydrothermal vents, whilst others favour an exogenic origin for life, motivated by findings such as those of Martins et al. (2008) and Furukawa et al. (2019): evidence that important amino acids and nucleobases are not unique to the Earth and may have originated elsewhere. The planets of stars in late stellar evolution are subject to the exact same constrains. Whilst CSEs may indeed supply some of the necessary ingredients for life, the planets on which their material is deposited may already have large abundances of prebiotic molecules. Therefore the door remains open for both an endogenic and exogenic abiogenesis. Regardless of that, it is well established that the five of the six most atomic constituents most commonly found in biomolecules: carbon, nitrogen, oxygen, phosphorous and sulphur are synthesised in stars with the sixth, hydrogen, being inherited from the primordial Universe. AGB mass envelopes, especially carbon-rich ones, are one of the environments from which carbonaceous matter is distributed to the surrounding interstellar medium, traversing the orbits of any planets that already happen to be in the vicinity. These CSEs are are also the formation sites for organic macromolecules: Polycyclic Aromatic Hydrocarbons (PAHs) and Aliphatic[43] Hydrocarbons resembling terrestrial kerogen (Kwok 2019). As discussed in Section 5.2.4, PAHs have been invoked as a catalyst in the synthesis of biological molecules; shielding them from radiation and degradation before the emergence of cell membranes (Ehrenfreund et al. 2006). If this speculative hypothesis gathers traction, the abundance of PAHs in CSEs should make their planetary environments conducive to such processes. If not, the abundance of hydrocarbons in CSEs would retain their prebiotic relevance as a bulk source of material from which more important reactions could proceed, facilitating the construction of biological molecules in which hydrocarbon chains form the backbone. To that end, an elaborate model for the delivery of CSE material to orbiting planets is warranted.

6.4. The Planetary Circumstellar Envelope Accretion Model

Whilst the accretion model in Section 5.1 represents a crude estimate of how much material can be delivered to planets in the vicinity of CSEs, it is an important first step in linking the prebiotic chemistry of CSEs and the habitability of the exoplanets that survive into the WD phase. At the time[44] of writing, there is a noticeable lack of research on this specific topic. Therefore, the model had to be constructed by tying together the concepts of AGB Mass Loss rate and Bondi-Hoyle-Lyttleton, traditionally applied in rather disparate areas of astronomy. Given the constraints of this thesis, several key assumptions had to be made:

1. The expanding shell of mass emitted by the AGB star being spherically symmetric
2. The mass loss rate of the AGB star being a direct function of its changing mass, luminosity and radius

---

[42] 23rd of February 2021

[43] Those that are not arranged in rings.
[44] 23rd February 2021

3. The model Earth-like planets needing to retain at least 97% of a 1 bar atmosphere inherited from an earlier phase of stellar evolution to be suitable for life

4. The changing orbital distances of model planets being directly dependent on the ratio between the final and initial stellar masses

5. The absence of other stars or planets that could influence outward planetary migration

6. The absence of mass loss after the maximum values for AGB mass loss, luminosity and radius have been attained

7. The prebiotic molecules contained within the CSEs not being ionised before reaching the planets

Tacking the first of the assumptions, the morphologies of evolved AGB stars and PNe by no means have to be spherically symmetric. The inner region of AGB mass envelopes have been found to exhibit major departures from sphericity (Chapman et al. 1994; Szymczak et al. 1998, 1999; Colomer et al. 2000). By the time the PN phase is reached, the system can exhibit a wide variety of morphologies including bipolar, helical and quadrupolar forms (Kwok 2007). As a result, there may be a greater outflow of material in some regions compared to others. Thus, how much material a planet could accrete would not only have a radial dependence but an angular one too. Furthermore, studies such as that of Bujarrabal & Pardo (2007) have indicated that whilst some molecules such as carbon monoxide aptly probe the morphologies of young PNe, the intensities of others are very difficult to predict as a function of position. Thus, a more detailed model for a planet's accretion would have to take the changing morphology of the CSE and the variable abundances of molecules therein into account. A detailed model would also have to account for physical parameters other than the masses, luminosities and radii of AGB stars; metallicity for example, whereby higher values have been found to slow the expansion velocities of ejected shells (Lagadec 2010). The interactions between the Lyman-continuum photons emitted by the central star and molecules are also bound to have important implications: though material such as amorphous carbon dust is likely to scatter the UV radiation, important prebiotic species such as Hydrogen Cyanide (HCN) and Amine (NH_3) may experience too much photo-ionisation before being accreted by the planet. Also, the UV photons have been found to facilitate the dehydrogenation of PAHs into the PN phase (García-Hernández & Manchado 2016), which would affect their capacity to serve as the inert scaffolding in which the synthesis of prebiotic molecules could proceed. To determine the extent to which UV photons would inhibit the synthesis of more complex biological molecules, the time-evolution of UV flux from the central star would have to factored into the accretion model in order to determine whether sufficient abundances of prebiotic molecules could be delivered to planets before being ionised or dehydrogenated. Models of the self-shielding of molecules in PNe such as that of Redman et al. (2003) should also be factored in here.

As for the planetary side of the accretion model, the assumption of an atmosphere needing to be retained for the planet to be habitable, is a major limitation. Given that the final orbital distances of the planets modelled in Section 5.1 (see Table 3) are on the order of $\sim 30 - 100$ AU a major inward migration mechanism would be necessary to reach the 0.015 AU stable HZ distances in the WD phase. Whilst WD 1856b may yield observational evidence for inward migration Vanderburg et al. (2020), it is unclear whether an Earth-mass planet could migrate on such a vast scale. The follow-up studies of WD 1856b Muñoz & Petrovich (2020); Stephan et al. (2020); Lagos et al. (2021) and O'Connor et al. (2021) indicate that it only migrated from distances of 2.5 AU to its current ~ 0.02 AU position. Moreover, Lagos et al. (2021) have argued that it has likely retained an atmosphere and migrated inwards due to common-envelope evolution. That is, a mechanism by which the WD and giant planet temporarily come to share a mass envelope. After its ejection, the giant planet loses orbital energy and reaches an orbit closer to the WD than would otherwise be expected. Given that an Earth-mass planet would not be massive enough experience common envelope evolution, it would not be able to circumvent atmospheric loss induced by the AGB stellar winds, To reach the WD HZs from the distances at which an Earth-like planet could retain its atmosphere (as modelled in Section 5.1), the Zeipel-Lidov Kozai mechanism invoked by Muñoz & Petrovich (2020) to explain WD 1856b's migration could be used. However, this would only apply in the presence of a distant binary system. Otherwise, a different migration mechanism would have to be applied. Progress on this could be made by models such of those of Frewen & Hansen (2014) that consider planet-planet scattering in light of observations of WD pollution rates and circumstellar disk profiles. Physical intuition would suggest that a giant planet, brown dwarf or binary stellar companion, considerably more massive than the Earth, would need to be present at orbital distances of ~ 100 AU to provide such a planet-planet perturbation. To account for this, the accretion model of Section 5.1 would have to be extended to predict the dynamical excitation timescales of AGB planetary systems and the dynamical relaxation timescales of WD planetary systems. For the AGB case, the main obstacle in terms of comparison with observation would be high optical depths of CSEs. For WDs, a young population would have to be targeted (ie. not the 100 pc sample discussed in Section 2.2.1). In this case the shorter diffusion timescales of younger, hotter WDs (Farihi 2016), would present the main obstacle to observational corroboration.

The problem of planetary migration could be circumvented by allowing for the possibility of a secondary or even tertiary[45] atmosphere being accreted from the CSE. In this case, the CSE would need to be modelled in terms of both its amorphous dust and gas phase components. This would also depend highly on the parameters assumed for the planet: throughout this thesis, the Earth's physical parameters have been assumed for test planets. If exoplanet classes such as super-Earths are found to be habitable then they may be more conducive to habitability than Earth-analogues in CSE and WD planetary systems: having a higher mass would result in better atmospheric retention and greater accretion rates from CSEs. Given that complex migration models would be required to reconcile the orbital distances required for complete atmospheric retention with those of WD HZs, modelling the possible acquisition of an

---

[45]If as for Earth, the hypothetical planet is assumed to have had two atmospheres during its progenitors main-sequence lifetime.

Earth-analogue or super-Earth would naturally be the next step in developing the accretion model. As can be inferred from Fig. 9, the accretion rates would be higher at orbital distances closer to the central star. Therefore, planets that are close enough to have their atmosphere eroded would indeed be likely to accrete mass at least several times that of the Earth's atmosphere. The main focus of a further refinement of the model would therefore be how such an a secondary or tertiary atmosphere could form for a given type of planet, and how the material present in CSEs would interact with its surface.

7. Conclusion

This thesis has juxtaposed findings from very disparate fields in order to reach a conclusion on whether life is likely to arise on the planet of a White Dwarf (WD). Whilst the first half of the thesis focused on WD systems themselves, the second explored the circumstellar environments that precede WDs in greater detail. In Sec. 2, it was found that there is unequivocal evidence for planets orbiting WDs; that as a trade-off for the large transit depths, there are likely to be at most 15 Habitable Zone Earth-analogues transiting their host WDs within 100 pc and that the majority of planet(esimals) responsible for WD pollution are likely to have compositions most consistent with asteroid analogues, some of which are comparable to those found in the Solar System. Furthermore, it was found in Sec. 3, that although WD planets orbiting in the Habitable Zone (HZ) are vulnerable to tidal destruction, the vast majority of systems do not have their HZs within their Roche Limit (RL) and are therefore, in principle capable of sustaining life in a stable HZ for ~ 6 Gyr. In light of the history of life on Earth, this is a sufficient timescale for life to develop. In Sections 4 and 5, it was found that the circumstellar envelopes resulting from Asymptotic Giant Branch (AGB) mass loss are sufficiently rich in Prebiotic Molecules in order for some of the proposed reactions responsible for the abiotic synthesis of molecules such as amino acids and simple sugars to be possible. The feasibility of such reactions is likely to be limited by the physical and chemical environment of the given planet. In that regard, it was found using a simple accretion model that planets present at initial orbital distance equivalent to Saturn and the Kuiper-belt in terms of incident stellar flux are capable of accreting the equivalent mass of several terrestrial atmospheres. Among AGB stars of spectral classes F5, F1 and A5, The most favourable conditions were facilitated by the F1 star in that the orbital distances of the Saturn and Kuiper Belt evolved outward at a rate conducive to the maximum accretion of Circumstellar Envelope (CSE) material and 97% retention of a 1 bar atmosphere. However, there appears to be a disparity between the orbital distances at which an Earth-like planet could be sufficiently far from the stellar winds of an AGB star to retain its atmosphere, and the orbital distances at which it would need to be at to be habitable during the WD phase of stellar evolution that follows. Therefore, there either needs to be a mechanism to facilitate a 100 AU inward migration for such a planet, or one by which an Earth-like planet could acquire a secondary or tertiary atmosphere from the CSE of an AGB or post-AGB star. Therefore, this thesis concludes with the finding that although many of the conditions for habitable environments in late stellar evolution are met, further work is needed to obtain a more complete and precise picture for the possibility of life evolving in the planetary systems of white dwarfs.

References

Aggarwal, H. & Oberbeck, V. 1974, The Astrophysical Journal, 191, 577

Agol, E. 2011, The Astrophysical Journal Letters, 731, L31

Akeson, R. L., Chen, X., Ciardi, D., et al. 2013, Publications of the Astronomical Society of the Pacific, 125, 989–999

Allègre, C., Manhès, G., & Lewin, É. 2001, Earth and Planetary Science Letters, 185, 49

Anglada-Escudé, G., Amado, P. J., Barnes, J., et al. 2016, Nature, 536, 437

Asplund, M., Grevesse, N., Sauval, A. J., & Scott, P. 2009, Annual review of astronomy and astrophysics, 47

Bachiller, R., Forveille, T., Huggins, P., & Cox, P. 1997, Astronomy and Astrophysics, 324, 1123

Barnes, R. 2017, Celestial Mechanics and Dynamical Astronomy, 129, 509–536

Barnes, R. & Heller, R. 2013, Astrobiology, 13, 279–291

Barstow, M. A., Barstow, J. K., Casewell, S. L., Holberg, J. B., & Hubeny, I. 2014, Monthly Notices of the Royal Astronomical Society, 440, 1607

Batalha, N. E., Lewis, N. K., Line, M. R., Valenti, J., & Stevenson, K. 2018, ApJ, 856, L34

Baud, B. & Habing, H. 1983, Astronomy and Astrophysics, 127, 73

Bauer, E. B. & Bildsten, L. 2019, ApJ, 872, 96

Becklin, E. E., Farihi, J., Jura, M., et al. 2005, ApJ, 632, L119

Braam, M. 2017, Thesis: The Habitability of Exoplanets

Bujarrabal, V. & Pardo, J. 2007, Baltic Astronomy, 16, 126

Burleigh, M., Hogan, E., & Clarke, F. 2005, Proceedings of the International Astronomical Union, 1, 344

Burton, A. S., Glavin, D. P., Callahan, M. P., et al. 2011, Meteoritics & Planetary Science, 46, 1703

Bédard, A., Bergeron, P., Brassard, P., & Fontaine, G. 2020, The Astrophysical Journal, 901, 93

Campbell, B., Walker, G. A. H., & Yang, S. 1988, ApJ, 331, 902

Carroll, P. B., Drouin, B. J., & Weaver, S. L. W. 2010, The Astrophysical Journal, 723, 845

Cassan, A., Kubas, D., Beaulieu, J.-P., et al. 2012, Nature, 481, 167

Cernicharo, J., Heras, A. M., Tielens, A., et al. 2001, The Astrophysical Journal Letters, 546, L123

Chan, S. & Kwok, S. 1990, Astronomy and Astrophysics, 237, 354

Chapman, J. M., Sivagnanam, P., Cohen, R., & Le Squeren, A. 1994, Monthly Notices of the Royal Astronomical Society, 268, 475

Charbonneau, D., Brown, T. M., Latham, D. W., & Mayor, M. 1999, The Astrophysical Journal Letters, 529, L45

Chayer, P., Fontaine, G., & Wesemael, F. 1995, The Astrophysical Journal Supplement Series, 99, 189

Cleaves, H. J. 2012, Evolution: Education and Outreach, 5, 342

Clemente, J. B., ADORNA, H., & VILLAR, J. 2015, in Theory and Practice of Computation: Proceedings of Workshop on Computation: Theory and Practice WCTP2013, World Scientific, 49–61

Cockell, C. S. 2020, Astrobiology: understanding life in the universe (John Wiley & Sons)

Colomer, F., Reid, M., Menten, K., & Bujarrabal, V. 2000, Astronomy and Astrophysics, 355, 979

Cronin, J. R. & Moore, C. B. 1971, Science, 172, 1327

Danger, G., Borget, F., Chomat, M., et al. 2011, Astronomy & Astrophysics, 535, A47

Davis, D. R., Farinella, P., & Marzari, F. 1999, Icarus, 137, 140

Debes, J. H. & Sigurdsson, S. 2002, ApJ, 572, 556

Dobbie, P. D., Napiwotzki, R., Burleigh, M. R., et al. 2006, Monthly Notices of the Royal Astronomical Society, 369, 383

Dobos, V. 2017, arXiv preprint arXiv:1704.07691

Dufour, P., Blouin, S., Coutu, S., et al. 2017, in Astronomical Society of the Pacific Conference Series, Vol. 509, 20th European White Dwarf Workshop, ed. P. E. Tremblay, B. Gänsicke, & T. Marsh, 3

Duley, W. & Williams, D. 1981, Monthly Notices of the Royal Astronomical Society, 196, 269

Dupuis, J., Fontaine, G., & Wesemael, F. 1993, The Astrophysical Journal Supplement Series, 87, 345

Edwards, J. L., Cox, E. G., & Ziurys, L. M. 2014, ApJ, 791, 79

Ehrenfreund, P., Glavin, D. P., Botta, O., Cooper, G., & Bada, J. L. 2001, Proceedings of the National Academy of Sciences, 98, 2138

Ehrenfreund, P., Rasmussen, S., Cleaves, J., & Chen, L. 2006, Astrobiology, 6, 490

Eisenstein, D. J., Liebert, J., Koester, D., et al. 2006, The Astronomical Journal, 132, 676

Elkins-Tanton, L., Asphaug, E., Bell, J., et al. 2014, in Lunar and Planetary Science Conference No. 1777, 1253

ESO. 2021

Etmański, B., Schmidt, M. R., & Szczerba, R. 2020, Advances in Astronomy and Space Physics, 10, 7

Farihi, J. 2011, arXiv e-prints, arXiv:1109.4970

Farihi, J. 2016, New Astronomy Reviews, 71, 9

Farihi, J., Barstow, M. A., Redfield, S., Dufour, P., & Hambly, N. C. 2010, MNRAS, 404, 2123

Farihi, J., Jura, M., & Zuckerman, B. 2009, The Astrophysical Journal, 694, 805–819

Farihi, J., Zuckerman, B., & Becklin, E. E. 2008, ApJ, 674, 431

Fischer, F. & Tropsch, H. 1926, Berichte der deutschen chemischen Gesellschaft (A and B Series), 59, 830

Fontaine, G., Brassard, P., & Bergeron, P. 2001, Publications of the Astronomical Society of the Pacific, 113, 409

Fossati, L., Bagnulo, S., Haswell, C., et al. 2012, The Astrophysical Journal Letters, 757, L15

Frewen, S. F. N. & Hansen, B. M. S. 2014, MNRAS, 439, 2442

Frewen, S. F. N. & Hansen, B. M. S. 2014, Monthly Notices of the Royal Astronomical Society, 439, 2442

Fulton, B., Tonry, J., Flewelling, H., et al. 2014, The Astrophysical Journal, 796, 114

Furukawa, Y., Chikaraishi, Y., Ohkouchi, N., et al. 2019, Proceedings of the National Academy of Sciences, 116, 24440

Gaia Collaboration, Brown, A. G. A., Vallenari, A., et al. 2018, A&A, 616, A1

Gänsicke, B. T., Marsh, T. R., Southworth, J., & Rebassa-Mansergas, A. 2006, Science, 314, 1908–1910

Gänsicke, B. T., Schreiber, M. R., Toloza, O., et al. 2019, arXiv preprint arXiv:1912.01611

García-Hernández, D. & Manchado, A. 2016in , IOP Publishing, 032009

Garcia-Hernandez, D. A., Zamora, O., Yagüe, A., et al. 2013, Astronomy & Astrophysics, 555, L3

Giammichele, N., Bergeron, P., & Dufour, P. 2012, The Astrophysical Journal Supplement Series, 199, 29

Gielen, C., Cami, J., Bouwman, J., Peeters, E., & Min, M. 2011, Astronomy & Astrophysics, 536, A54

Güdel, M., Dvorak, R., Erkaev, N., et al. 2014, Protostars and Planets VI

Habing, H. J. & Olofsson, H. 2013, Asymptotic giant branch stars (Springer Science & Business Media)

Harrison, S. A. & Lane, N. 2018, Nature communications, 9, 1

Hatzes, A. P., Cochran, W. D., Endl, M., et al. 2003, The Astrophysical Journal, 599, 1383–1394

Holberg, J. B., Barstow, M. A., & Green, E. M. 1997, ApJ, 474, L127

Horne, K. & Marsh, T. 1986, Monthly Notices of the Royal Astronomical Society, 218, 761

Hu, Y. & Yang, J. 2014, Proceedings of the National Academy of Sciences, 111, 629

Iben Jr, I. & Renzini, A. 1984, Physics Reports, 105, 329

Iliadis, C. 2015, Nuclear physics of stars (John Wiley & Sons)

Jiménez-Serra, I., Martín-Pintado, J., Rivilla, V. M., et al. 2020, Astrobiology, 20, 1048

Jiménez-Esteban, F. M., Torres, S., Rebassa-Mansergas, A., et al. 2018, Monthly Notices of the Royal Astronomical Society, 480, 4505–4518

Jorge, D. 2020, Element gradients in the Solar neighborhood affecting terrestrial planet composition

Josselin, E. & Bachiller, R. 2003, Astronomy & Astrophysics, 397, 659

Jura, M., Farihi, J., Zuckerman, B., & Becklin, E. 2007, The Astronomical Journal, 133, 1927

Jura, M., Xu, S., Klein, B., Koester, D., & Zuckerman, B. 2012, The Astrophysical Journal, 750, 69

Kaltenegger, L., MacDonald, R. J., Kozakis, T., et al. 2020, ApJ, 901, L1

Kaplan, D. L., Boyles, J., Dunlap, B. H., et al. 2014, ApJ, 789, 119

Kasting, J. F., Whitmire, D. P., & Reynolds, R. T. 1993, Icarus, 101, 108

Kilic, M., Hambly, N., Bergeron, P., Genest-Beaulieu, C., & Rowell, N. 2018, Monthly Notices of the Royal Astronomical Society: Letters, 479, L113

Klein, B., Jura, M., Koester, D., & Zuckerman, B. 2011, The Astrophysical Journal, 741, 64

Koester, D. 2009, Astronomy & Astrophysics, 498, 517

Koester, D., Gänsicke, B. T., & Farihi, J. 2014, A&A, 566, A34

Kohler, S. 2018, Habitable Moons Instead of Habitable Planets?, AAS Nova Highlights

Kopetzki, D. & Antonietti, M. 2011, New Journal of Chemistry, 35, 1787

Kopparapu, R. K., Ramirez, R., Kasting, J. F., et al. 2013, The Astrophysical Journal, 765, 131

Kozakis, T. & Kaltenegger, L. 2019, The Astrophysical Journal, 875, 99

Kozakis, T., Kaltenegger, L., & Hoard, D. W. 2018, ApJ, 862, 69

Kozakis, T., Lin, Z., & Kaltenegger, L. 2020, ApJ, 894, L6

Krasnokutski, S. A., Jäger, C., & Henning, T. 2020, The Astrophysical Journal, 889, 67

Kuan, Y.-J., Charnley, S. B., Huang, H.-C., Tseng, W.-L., & Kisiel, Z. 2003, The Astrophysical Journal, 593, 848

Kwok, S. 1993, Annual review of astronomy and astrophysics, 31, 63

Kwok, S. 2004, Nature, 430, 985

Kwok, S. 2007, The origin and evolution of planetary nebulae (Cambridge University Press)

Kwok, S. 2019, arXiv preprint arXiv:1907.06127

Kwok, S., Volk, K., & Bidelman, W. P. 1997, The Astrophysical Journal Supplement Series, 112, 557

Lagadec, E. 2010, Memorie della Societa Astronomica Italiana, 81, 1083

Lagos, F., Schreiber, M., Zorotovic, M., et al. 2021, Monthly Notices of the Royal Astronomical Society, 501, 676

Lammer, H., Bredehöft, J., Coustenis, A., et al. 2009, The Astronomy and Astrophysics Review, 17, 181

Lattelais, M., Pauzat, F., Pilmé, J., Ellinger, Y., & Ceccarelli, C. 2011, Astronomy & Astrophysics, 532, A39

LeBlanc, F. 2011, An introduction to stellar astrophysics (John Wiley & Sons)

Leconte, J., Forget, F., Charnay, B., Wordsworth, R., & Pottier, A. 2013, Nature, 504, 268

Lee, E. J. & Connors, N. J. 2021, The Astrophysical Journal, 908, 32

Levy, M., Miller, S. L., & Oró, J. 1999, Journal of molecular evolution, 49, 165

Li, X., Millar, T. J., Heays, A. N., et al. 2016, A&A, 588, A4

Liebert, J., Bergeron, P., Eisenstein, D., et al. 2004, The Astrophysical Journal Letters, 606, L147

Lodders, K. 2003, ApJ, 591, 1220

Loeb, A. & Maoz, D. 2013, Monthly Notices of the Royal Astronomical Society: Letters, 432, L11

López-Tarifa, P., du Penhoat, M.-A. H., Vuilleumier, R., et al. 2011, Physical review letters, 107, 023202

Lutz, J. 1981, The Astrophysical Journal, 247, 144

Martins, Z., Botta, O., Fogel, M. L., et al. 2008, Earth and planetary science Letters, 270, 130

Massalkhi, S., Agúndez, M., & Cernicharo, J. 2019, Astronomy & Astrophysics, 628, A62

Massalkhi, S., Agúndez, M., Cernicharo, J., & Velilla-Prieto, L. 2020, A&A, 641, A57

Mayor, M. & Queloz, D. 1995, Nature, 378, 355

Mayor, M. & Queloz, D. 1995, Nature, 378, 355

McCook, G. P. & Sion, E. M. 1999, The Astrophysical Journal Supplement Series, 121, 1

Melis, C., Jura, M., Albert, L., Klein, B., & Zuckerman, B. 2010, The Astrophysical Journal, 722, 1078

Millar, T. J. & Woods, P. M. 2005, in ESA Special Publication, Vol. 577, ESA Special Publication, ed. A. Wilson, 229–234

Miller Bertolami, M. M., Melendez, B. E., Althaus, L. G., & Isern, J. 2014, J. Cosmology Astropart. Phys., 2014, 069

Morgan, J. W. & Anders, E. 1980, Proceedings of the National Academy of Sciences, 77, 6973–6977

Muñoz, D. J. & Petrovich, C. 2020, The Astrophysical Journal Letters, 904, L3

NASA. 2021, Nasa Exoplanet Archive

O'Brien, D. P., Walsh, K. J., Morbidelli, A., Raymond, S. N., & Mandell, A. M. 2014, Icarus, 239, 74

O'Connor, C. E., Liu, B., & Lai, D. 2021, Monthly Notices of the Royal Astronomical Society, 501, 507

Paczynski, B. 1971, Acta Astronomica, 21, 417

Parsons, S., Gänsicke, B. T., Marsh, T., et al. 2017, Monthly Notices of the Royal Astronomical Society, 470, 4473

Pavlov, A. A., Kasting, J. F., Brown, L. L., Rages, K. A., & Freedman, R. 2000, J. Geophys. Res., 105, 11981

Perea-Calderón, J., García-Hernández, D., García-Lario, P., Szczerba, R., & Bobrowsky, M. 2009, Astronomy & Astrophysics, 495, L5

Provencal, J. L., Shipman, H., Høg, E., & Thejll, P. 1998, The Astrophysical Journal, 494, 759

Quintana, E. V. & Barclay, T. 2016, in American Astronomical Society Meeting Abstracts, Vol. 228, American Astronomical Society Meeting Abstracts #228, 404.05

Ramirez, R. M. & Kaltenegger, L. 2016, The Astrophysical Journal, 823, 6

Ramirez, R. M. & Kaltenegger, L. 2018, The Astrophysical Journal, 858, 72

Rao, N. K., Lambert, D. L., Reddy, A. B. S., et al. 2020, PASP, 132, 074201

Redman, M. P., Viti, S., Cau, P., & Williams, D. A. 2003, Monthly Notices of the Royal Astronomical Society, 345, 1291–1296

Robert, F. 2001, Science, 293, 1056

Roy, D., Najafian, K., & von Ragué Schleyer, P. 2007, Proceedings of the National Academy of Sciences, 104, 17272

Ruiz, M. T., Bergeron, P., Leggett, S., & Anguita, C. 1995, The Astrophysical Journal Letters, 455, L159

Russell, R., Soifer, B., & Willner, S. 1977, The Astrophysical Journal, 217, L149

Schmidt, D. R. & Ziurys, L. M. 2016, ApJ, 817, 175

Schmidt, D. R. & Ziurys, L. M. 2018, IAU Symposium, 332, 218

Schmidt, D. R. & Ziurys, L. M. 2019, ApJ, 881, L38

Stephan, A. P., Naoz, S., & Gaudi, B. S. 2020, arXiv preprint arXiv:2010.10534

Stone, N., Metzger, B. D., & Loeb, A. 2015, Monthly Notices of the Royal Astronomical Society, 448, 188–206

Szymczak, M., Cohen, R., & Richards, A. 1998, Monthly Notices of the Royal Astronomical Society, 297, 1151

Szymczak, M., Cohen, R., & Richards, A. 1999, Monthly Notices of the Royal Astronomical Society, 304, 877

Taylor, G. J. 2013, Geochemistry, 73, 401

Tenenbaum, E., Milam, S., Woolf, N., & Ziurys, L. M. 2009, The Astrophysical Journal Letters, 704, L108

Torres, S. & García-Berro, E. 2016, Astronomy & Astrophysics, 588, A35

Tremblay, P.-E., Fontaine, G., Fusillo, N. P. G., et al. 2019, Nature, 565, 202

Trigo-Rodríguez, J. M., Rimola, A., Tanbakouei, S., Soto, V. C., & Lee, M. 2019, Space Sci. Rev., 215, 18

Trixler, F. & Heckl, W. M. 2009in , Citeseer, 273–274

Van de Sande, M., Walsh, C., Mangan, T. P., & Decin, L. 2019, Monthly Notices of the Royal Astronomical Society, 490, 2023

van Sluijs, L. & Van Eylen, V. 2018, Monthly Notices of the Royal Astronomical Society, 474, 4603

Van Winckel, H., Evans, T. L., Briquet, M., et al. 2009, Astronomy & Astrophysics, 505, 1221

Van Winckel, H., Waelkens, C., Fernie, J., & Waters, L. 1999, Astronomy and Astrophysics, 343, 202

Vanderbosch, Z., Hermes, J. J., Dennihy, E., et al. 2020, ApJ, 897, 171

Vanderburg, A., Johnson, J. A., Rappaport, S., et al. 2015, in AAS/Division for Extreme Solar Systems Abstracts, Vol. 47, AAS/Division for Extreme Solar Systems Abstracts, 502.02

Vanderburg, A., Rappaport, S. A., Xu, S., et al. 2020, Nature, 585, 363

Vassiliadis, E. & Wood, P. R. 1993, ApJ, 413, 641

Vauclair, G., Vauclair, S., & Greenstein, J. L. 1979, A&A, 80, 79

Veras, D. 2016, Royal Society Open Science, 3, 150571

Verniani, F. 1966, Journal of Geophysical Research, 71, 385

Villaver, E. & Livio, M. 2007, The Astrophysical Journal, 661, 1192

Volk, K. M. & Kwok, S. 1989, ApJ, 342, 345

Voss, B., Koester, D., Napiwotzki, R., Christlieb, N., & Reimers, D. 2007, Astronomy & Astrophysics, 470, 1079

Vulpius, S., Noack, L., Sohl, F., Ortenzi, G., & Jörg Hoffmann, E. 2020, in European Planetary Science Congress, EPSC2020–959

Wagner, W. & Pruß, A. 2002, Journal of physical and chemical reference data, 31, 387

Waters, L., Molster, F., De Jong, T., et al. 1996, Astronomy and Astrophysics, 315, L361

Wegner, G. 1972, ApJ, 172, 451

Wehrse, R. 1975, A&A, 39, 169

Weidemann, V. 1960, ApJ, 131, 638

Weinberger, R. & Kerber, F. 1997, Science, 276, 1382

Werner, K., Hammer, N., Nagel, T., Rauch, T., & Dreizler, S. 2004, arXiv preprint astro-ph/0410690

Willacy, K. & Cherchneff, I. 1998, Astronomy and Astrophysics, 330, 676

Willson, L. & Bowen, G. 1984, Nature, 312, 429

Wolszczan, A. & Frail, D. A. 1992, Nature, 355, 145

Woods, P. M. & Nyman, L.-Å. 2005, Astrochemistry: Recent Succes and Current Challanges, 1

Wright, J., Allen, V., Alvarado-Gómez, J., et al. 2019

Xu, S., Hallakoun, N., Gary, B., et al. 2019, AJ, 157, 255

Xu, S., Jura, M., Klein, B., Koester, D., & Zuckerman, B. 2013, The Astrophysical Journal, 766, 132

Young, P., Schneider, D., & Shectman, S. 1981, The Astrophysical Journal, 245, 1035

Ziurys, L. M. 2008, in Organic Matter in Space, ed. S. Kwok & S. Sanford, Vol. 251, 147–156

Ziurys, L. M., Halfen, D. T., & Woolf, N. J. 2009, in Astronomical Society of the Pacific Conference Series, Vol. 420, Bioastronomy 2007: Molecules, Microbes and Extraterrestrial Life, ed. K. J. Meech, J. V. Keane, M. J. Mumma, J. L. Siefert, & D. J. Werthimer, 59

Zuckerman, B., Koester, D., Reid, I. N., & Hünsch, M. 2003, The Astrophysical Journal, 596, 477

Zuckerman, B., Melis, C., Klein, B., Koester, D., & Jura, M. 2010, ApJ, 722, 725

Appendix A: Propagated Error Values for Habitable Zone Calculations

Appendix A.1: Roche Limits in 10^{-2} AU

Enumeration	Name	Roche Limit	Error
189	WD 0651-398A	0.361011	0.009864
190	WD 0651-398B	0.374323	0.009175
194	WD 0708-670	0.350864	0.006265
607	WD 1116-470	0.354993	0.008161
1136	WD 1817-598	0.284960	0.015831
1177	WD 2118-388	0.335590	0.011415
1818	WD 0839-327	0.326198	0.012081
1989	WD 1826-045	0.377957	0.032396
2038	WD 1811+327.2	0.352941	0.002477
2052	WD 1811+327.1	0.353970	0.002257
2114	WD 2316-064	0.319539	0.004281
2129	WD 2107-216	0.363363	0.002142
2155	WD 0651-479	0.354993	0.020402
2466	WD 1503-070	0.357625	0.002010
2505	WD 0213+396	0.406365	0.017126
2605	WD 0008+424	0.354379	0.002047
2678	WD 0243-026	0.371364	0.000932
2679	WD 0326-273	0.278481	0.013261
2680	WD 0548-001	0.371177	0.002239
2681	WD 0728+642	0.335818	0.002052
2690	WD 1829+547	0.391839	0.005024
2696	WD 0038-226	0.340982	0.005086
2701	WD 1821-131	0.352941	0.010320
2706	WD 0659-063	0.357021	0.001815
2708	WD 0000-345	0.374323	0.005505
2711	WD 0053-117	0.354584	0.002045
2712	WD 0141-675	0.352941	0.006192
2715	WD 0322-019	0.370429	0.001874
2718	WD 0423+044	0.372293	0.002040
2721	WD 0511+079	0.394170	0.001655
2723	WD 0644+025	0.420648	0.001308
2727	WD 1036-204	0.361798	0.015320
2730	WD 1444-174	0.400521	0.001603
2731	WD 1733-544	0.372479	0.003706
2745	WD 2105-820	0.391839	0.016745
20281	WD 2253-081	0.354788	0.001430
20549	WD 0011-721	0.344484	0.008666
20614	WD 0752-676	0.350864	0.004177
20619	WD 1241-798	0.337857	0.013514
20626	WD 1708-147	0.346637	0.010699
20637	WD 2359-434	0.398426	0.014577
20754	WD 0117-145	0.343179	0.002401
20761	WD 0851-246	0.337857	0.011262
20793	WD 1008+290	0.378496	0.010230
20841	WD 0856-007	0.318528	0.002534
20865	WD 2028-171	0.347064	0.002348
21072	WD 0025+054	0.353559	0.002262
21391	WD 0136+152	0.370616	0.003744
21553	WD 1242-105	0.250174	0.001643
21851	WD 1743-545	0.350864	0.010442
51479	WD 2159-754	0.421374	0.005792
51895	WD 0123-460	0.368735	0.011346
51964	WD 0148+641	0.369301	0.000943
51971	WD 0150+256	0.339872	0.000890
52130	WD 0233-242	0.262310	0.002616
52141	WD 0236+259	0.359823	0.000993
52414	WD 0344+014	0.309668	0.003217
52585	WD 0655-390	0.359027	0.007978
52799	WD 0802+387	0.362973	0.000976

Enumeration	Name	Roche Limits	Error
52842	WD 0810+489	0.360813	0.005727
52880	WD 0821-669	0.368735	0.007564
53297	WD 0928-713	0.376149	0.014537
53654	WD 1033+714	0.378496	0.002692
53855	WD 1124-293	0.346637	0.017118
53920	WD 1136-286	0.451086	0.002527
54218	WD 1237-230	0.245571	0.001279
54530	WD 1338+052	0.325471	0.002184
54551	WD 1339-340	0.354993	0.008161
54736	WD 1418-088	0.303932	0.002505
54917	WD 1447-190	0.266720	0.001807
55353	WD 1630+089	0.301689	0.001977
55391	WD 1647-327	0.346637	0.006419
55408	WD 1656-062	0.367977	0.001329
55614	WD 1756+143	0.352320	0.002071
55619	WD 1814+134	0.335133	0.002289
55712	WD 2035-369	0.364914	0.009654
55750	WD 2057-493	0.366834	0.005732
55789	WD 2119+040	0.327641	0.001198
55912	WD 2215+368	0.344050	0.003041
55914	WD 2216-657	0.364914	0.017377
55927	WD 2226-754A	0.337857	0.009010
55928	WD 2226-754B	0.340095	0.008891
56301	WD 2211-392	0.395160	0.006586

Appendix A.2.1: Earth-insolation Distances

Enumeration	Name	Earth-equivalent	Error
189	WD 0651-398A	1.883649	0.130141
190	WD 0651-398B	1.412538	0.113858
194	WD 0708-670	0.954993	0.043987
607	WD 1116-470	1.244515	0.071653
1136	WD 1817-598	1.273503	0.087986
1177	WD 2118-388	1.083927	0.074889
1818	WD 0839-327	3.630781	0.167234
1989	WD 1826-045	3.589219	0.413299
2038	WD 1811+327.2	1.883649	0.433804
2052	WD 1811+327.1	2.600160	0.568876
2114	WD 2316-064	0.749894	0.086350
2129	WD 2107-216	0.977237	0.033759
2155	WD 0651-479	0.803526	0.083273
2466	WD 1503-070	1.659587	0.229322
2505	WD 0213+396	2.454709	0.141330
2605	WD 0008+424	1.905461	0.021941
2678	WD 0243-026	1.548817	0.071338
2679	WD 0326-273	4.518559	0.468281
2680	WD 0548-001	1.258925	0.043490
2681	WD 0728+642	1.083927	0.037444
2690	WD 1829+547	1.216186	0.056018
2696	WD 0038-226	1.071519	0.037016
2701	WD 1821-131	1.364583	0.078566
2706	WD 0659-063	1.584893	0.073000
2708	WD 0000-345	1.318257	0.060719
2711	WD 0053-117	1.927525	0.088782
2712	WD 0141-675	1.584893	0.073000
2715	WD 0322-019	0.988553	0.045533
2718	WD 0423+044	0.776247	0.035754
2721	WD 0511+079	1.348963	0.077667
2723	WD 0644+025	1.273503	0.043993
2727	WD 1036-204	0.851138	0.039203
2730	WD 1444-174	0.683912	0.023626
2731	WD 1733-544	1.496236	0.017229
2745	WD 2105-820	3.019952	0.173874
20281	WD 2253-081	1.318257	0.182157
20549	WD 0011-721	1.640590	0.094457
20614	WD 0752-676	1.230269	0.056666
20619	WD 1241-798	1.244515	0.100314
20626	WD 1708-147	3.427678	0.315758
20637	WD 2359-434	2.089296	0.096233
20754	WD 0117-145	1.174898	0.040587
20761	WD 0851-246	0.484172	0.033451
20793	WD 1008+290	0.645654	0.022304
20841	WD 0856-007	0.977237	0.045012
20865	WD 2028-171	1.188502	0.054742
21072	WD 0025+054	1.244515	0.028661
21391	WD 0136+152	2.238721	0.077337
21553	WD 1242-105	4.365158	0.251324
21851	WD 1743-545	0.785236	0.054252
51479	WD 2159-754	1.972423	0.158987
51895	WD 0123-460	1.202264	0.096909
51964	WD 0148+641	2.786121	0.288740
51971	WD 0150+256	2.371374	0.245757
52130	WD 0233-242	1.216186	0.070022
52141	WD 0236+259	1.202264	0.013844
52414	WD 0344+014	0.977237	0.056264
52585	WD 0655-390	1.513561	0.087143
52799	WD 0802+387	0.831764	0.038311

Enumeration	Name	Earth-equivalent	Error
52842	WD 0810+489	1.513561	0.087143
52880	WD 0821-669	0.901571	0.041526
53297	WD 0928-713	2.540973	0.058519
53654	WD 1033+714	0.732825	0.033754
53855	WD 1124-293	3.235937	0.260833
53920	WD 1136-286	0.338844	0.011705
54218	WD 1237-230	1.862087	0.171535
54530	WD 1338+052	0.741310	0.034145
54551	WD 1339-340	1.047129	0.048231
54736	WD 1418-088	3.311311	0.495687
54917	WD 1447-190	3.126079	0.251978
55353	WD 1630+089	1.174898	0.040587
55391	WD 1647-327	1.513561	0.052286
55408	WD 1656-062	1.135011	0.039209
55614	WD 1756+143	1.122018	0.038760
55619	WD 1814+134	0.988553	0.034150
55712	WD 2035-369	3.427678	0.276288
55750	WD 2057-493	1.011579	0.034945
55789	WD 2119+040	1.059254	0.048789
55912	WD 2215+368	0.785236	0.036168
55914	WD 2216-657	3.427678	0.513106
55927	WD 2226-754A	0.794328	0.036587
55928	WD 2226-754B	0.707946	0.032608
56301	WD 2211-392	1.148154	0.079326

Appendix A.2.2: Inner Boundaries

Enumeration	Name	Leconte et al.	Error
189	WD 0651-398A	1.883649	0.131662
190	WD 0651-398B	1.412538	0.114950
194	WD 0708-670	0.954993	0.044216
607	WD 1116-470	1.244515	0.072263
1136	WD 1817-598	1.273503	0.088533
1177	WD 2118-388	1.083927	0.075206
1818	WD 0839-327	3.630781	0.169088
1989	WD 1826-045	3.589219	0.414054
2038	WD 1811+327.2	1.883649	0.433826
2052	WD 1811+327.1	2.600160	0.568916
2114	WD 2316-064	0.749894	0.086371
2129	WD 2107-216	0.977237	0.033807
2155	WD 0651-479	0.803526	0.083297
2466	WD 1503-070	1.659587	0.229352
2505	WD 0213+396	2.454709	0.141435
2605	WD 0008+424	1.905461	0.022021
2678	WD 0243-026	1.548817	0.071347
2679	WD 0326-273	4.518559	0.469399
2680	WD 0548-001	1.258925	0.043590
2681	WD 0728+642	1.083927	0.037456
2690	WD 1829+547	1.216186	0.056034
2696	WD 0038-226	1.071519	0.037200
2701	WD 1821-131	1.364583	0.079128
2706	WD 0659-063	1.584893	0.073071
2708	WD 0000-345	1.318257	0.061094
2711	WD 0053-117	1.927525	0.088905
2712	WD 0141-675	1.584893	0.073636
2715	WD 0322-019	0.988553	0.045555
2718	WD 0423+044	0.776247	0.035789
2721	WD 0511+079	1.348963	0.077705
2723	WD 0644+025	1.273503	0.044091
2727	WD 1036-204	0.851138	0.040842
2730	WD 1444-174	0.683912	0.023658
2731	WD 1733-544	1.496236	0.018368
2745	WD 2105-820	3.019952	0.175761
20281	WD 2253-081	1.318257	0.182163
20549	WD 0011-721	1.640590	0.095286
20614	WD 0752-676	1.230269	0.056991
20619	WD 1241-798	1.244515	0.100844
20626	WD 1708-147	3.427678	0.323251
20637	WD 2359-434	2.089296	0.097045
20754	WD 0117-145	1.174898	0.040639
20761	WD 0851-246	0.484172	0.033570
20793	WD 1008+290	0.645654	0.023330
20841	WD 0856-007	0.977237	0.045093
20865	WD 2028-171	1.188502	0.054791
21072	WD 0025+054	1.244515	0.028685
21391	WD 0136+152	2.238721	0.077396
21553	WD 1242-105	4.365158	0.251537
21851	WD 1743-545	0.785236	0.054572
51479	WD 2159-754	1.972423	0.159504
51895	WD 0123-460	1.202264	0.097459
51964	WD 0148+641	2.786121	0.288766
51971	WD 0150+256	2.371374	0.245767
52130	WD 0233-242	1.216186	0.070125
52141	WD 0236+259	1.202264	0.013875
52414	WD 0344+014	0.977237	0.056273
52585	WD 0655-390	1.513561	0.088018
52799	WD 0802+387	0.831764	0.038316

Enumeration	Name	Leconte et al.	Error
52842	WD 0810+489	1.513561	0.087165
52880	WD 0821-669	0.901571	0.041861
53297	WD 0928-713	2.540973	0.060365
53654	WD 1033+714	0.732825	0.033769
53855	WD 1124-293	3.235937	0.261929
53920	WD 1136-286	0.338844	0.011829
54218	WD 1237-230	1.862087	0.171543
54530	WD 1338+052	0.741310	0.034170
54551	WD 1339-340	1.047129	0.048414
54736	WD 1418-088	3.311311	0.495776
54917	WD 1447-190	3.126079	0.252089
55353	WD 1630+089	1.174898	0.040588
55391	WD 1647-327	1.513561	0.054610
55408	WD 1656-062	1.135011	0.039219
55614	WD 1756+143	1.122018	0.038789
55619	WD 1814+134	0.988553	0.034158
55712	WD 2035-369	3.427678	0.277689
55750	WD 2057-493	1.011579	0.035115
55789	WD 2119+040	1.059254	0.048792
55912	WD 2215+368	0.785236	0.036177
55914	WD 2216-657	3.427678	0.530749
55927	WD 2226-754A	0.794328	0.036712
55928	WD 2226-754B	0.707946	0.032769
56301	WD 2211-392	1.148154	0.079900

Appendix A.2.3: Outer Boundaries

Enumeration	Name	CO_2 Maximum Greenhouse	Error
189	WD 0651-398A	1.883649	0.133063
190	WD 0651-398B	1.412538	0.116156
194	WD 0708-670	0.954993	0.044546
607	WD 1116-470	1.244515	0.073015
1136	WD 1817-598	1.273503	0.089329
1177	WD 2118-388	1.083927	0.075653
1818	WD 0839-327	3.630781	0.169694
1989	WD 1826-045	3.589219	0.414296
2038	WD 1811+327.2	1.883649	0.433849
2052	WD 1811+327.1	2.600160	0.568948
2114	WD 2316-064	0.749894	0.086404
2129	WD 2107-216	0.977237	0.033867
2155	WD 0651-479	0.803526	0.083333
2466	WD 1503-070	1.659587	0.229383
2505	WD 0213+396	2.454709	0.141469
2605	WD 0008+424	1.905461	0.022096
2678	WD 0243-026	1.548817	0.071355
2679	WD 0326-273	4.518559	0.469735
2680	WD 0548-001	1.258925	0.043709
2681	WD 0728+642	1.083927	0.037472
2690	WD 1829+547	1.216186	0.056053
2696	WD 0038-226	1.071519	0.037456
2701	WD 1821-131	1.364583	0.079807
2706	WD 0659-063	1.584893	0.073148
2708	WD 0000-345	1.318257	0.061516
2711	WD 0053-117	1.927525	0.089023
2712	WD 0141-675	1.584893	0.074336
2715	WD 0322-019	0.988553	0.045585
2718	WD 0423+044	0.776247	0.035842
2721	WD 0511+079	1.348963	0.077746
2723	WD 0644+025	1.273503	0.044181
2727	WD 1036-204	0.851138	0.043301
2730	WD 1444-174	0.683912	0.023707
2731	WD 1733-544	1.496236	0.019515
2745	WD 2105-820	3.019952	0.176099
20281	WD 2253-081	1.318257	0.182170
20549	WD 0011-721	1.640590	0.096206
20614	WD 0752-676	1.230269	0.057409
20619	WD 1241-798	1.244515	0.101535
20626	WD 1708-147	3.427678	0.325341
20637	WD 2359-434	2.089296	0.097450
20754	WD 0117-145	1.174898	0.040715
20761	WD 0851-246	0.484172	0.033784
20793	WD 1008+290	0.645654	0.024910
20841	WD 0856-007	0.977237	0.045218
20865	WD 2028-171	1.188502	0.054856
21072	WD 0025+054	1.244515	0.028715
21391	WD 0136+152	2.238721	0.077438
21553	WD 1242-105	4.365158	0.251687
21851	WD 1743-545	0.785236	0.055072
51479	WD 2159-754	1.972423	0.159724
51895	WD 0123-460	1.202264	0.098140
51964	WD 0148+641	2.786121	0.288777
51971	WD 0150+256	2.371374	0.245774
52130	WD 0233-242	1.216186	0.070286
52141	WD 0236+259	1.202264	0.013915
52414	WD 0344+014	0.977237	0.056285
52585	WD 0655-390	1.513561	0.088993
52799	WD 0802+387	0.831764	0.038322

Enumeration	Name	CO_2 Maximum Greenhouse	Error
52842	WD 0810+489	1.513561	0.087187
52880	WD 0821-669	0.901571	0.042336
53297	WD 0928-713	2.540973	0.061348
53654	WD 1033+714	0.732825	0.033792
53855	WD 1124-293	3.235937	0.262222
53920	WD 1136-286	0.338844	0.012023
54218	WD 1237-230	1.862087	0.171554
54530	WD 1338+052	0.741310	0.034213
54551	WD 1339-340	1.047129	0.048668
54736	WD 1418-088	3.311311	0.495845
54917	WD 1447-190	3.126079	0.252191
55353	WD 1630+089	1.174898	0.040591
55391	WD 1647-327	1.513561	0.057213
55408	WD 1656-062	1.135011	0.039231
55614	WD 1756+143	1.122018	0.038829
55619	WD 1814+134	0.988553	0.034170
55712	WD 2035-369	3.427678	0.277977
55750	WD 2057-493	1.011579	0.035345
55789	WD 2119+040	1.059254	0.048796
55912	WD 2215+368	0.785236	0.036191
55914	WD 2216-657	3.427678	0.533944
55927	WD 2226-754A	0.794328	0.036913
55928	WD 2226-754B	0.707946	0.033034
56301	WD 2211-392	1.148154	0.080568

Appendix A.2.4: Methane Outer Boundaries

Enumeration	Name	0.1 CH_4/CO_2	Error
189	WD 0651-398A	1.883649	0.150200
190	WD 0651-398B	1.412538	0.127929
194	WD 0708-670	0.954993	0.046727
607	WD 1116-470	1.244515	0.079300
1136	WD 1817-598	1.273503	0.094446
1177	WD 2118-388	1.083927	0.078758
1818	WD 0839-327	3.630781	0.193609
1989	WD 1826-045	3.589219	0.424694
2038	WD 1811+327.2	1.883649	0.434094
2052	WD 1811+327.1	2.600160	0.569458
2114	WD 2316-064	0.749894	0.086589
2129	WD 2107-216	0.977237	0.034400
2155	WD 0651-479	0.803526	0.083550
2466	WD 1503-070	1.659587	0.229736
2505	WD 0213+396	2.454709	0.142931
2605	WD 0008+424	1.905461	0.023042
2678	WD 0243-026	1.548817	0.071450
2679	WD 0326-273	4.518559	0.485130
2680	WD 0548-001	1.258925	0.044819
2681	WD 0728+642	1.083927	0.037588
2690	WD 1829+547	1.216186	0.056249
2696	WD 0038-226	1.071519	0.039263
2701	WD 1821-131	1.364583	0.085724
2706	WD 0659-063	1.584893	0.073955
2708	WD 0000-345	1.318257	0.065616
2711	WD 0053-117	1.927525	0.090493
2712	WD 0141-675	1.584893	0.081241
2715	WD 0322-019	0.988553	0.045807
2718	WD 0423+044	0.776247	0.036170
2721	WD 0511+079	1.348963	0.078193
2723	WD 0644+025	1.273503	0.045348
2727	WD 1036-204	0.851138	0.055301
2730	WD 1444-174	0.683912	0.024014
2731	WD 1733-544	1.496236	0.029224
2745	WD 2105-820	3.019952	0.201228
20281	WD 2253-081	1.318257	0.182250
20549	WD 0011-721	1.640590	0.105172
20614	WD 0752-676	1.230269	0.060748
20619	WD 1241-798	1.244515	0.106954
20626	WD 1708-147	3.427678	0.416181
20637	WD 2359-434	2.089296	0.107745
20754	WD 0117-145	1.174898	0.041231
20761	WD 0851-246	0.484172	0.034582
20793	WD 1008+290	0.645654	0.032027
20841	WD 0856-007	0.977237	0.045962
20865	WD 2028-171	1.188502	0.055368
21072	WD 0025+054	1.244515	0.028962
21391	WD 0136+152	2.238721	0.078194
21553	WD 1242-105	4.365158	0.254423
21851	WD 1743-545	0.785236	0.057850
51479	WD 2159-754	1.972423	0.166619
51895	WD 0123-460	1.202264	0.103915
51964	WD 0148+641	2.786121	0.289134
51971	WD 0150+256	2.371374	0.245891
52130	WD 0233-242	1.216186	0.071208
52141	WD 0236+259	1.202264	0.014239
52414	WD 0344+014	0.977237	0.056364
52585	WD 0655-390	1.513561	0.098354
52799	WD 0802+387	0.831764	0.038367

Enumeration	Name	0.1 CH_4/CO_2	Error
52842	WD 0810+489	1.513561	0.087442
52880	WD 0821-669	0.901571	0.045483
53297	WD 0928-713	2.540973	0.081803
53654	WD 1033+714	0.732825	0.033932
53855	WD 1124-293	3.235937	0.277222
53920	WD 1136-286	0.338844	0.013060
54218	WD 1237-230	1.862087	0.171638
54530	WD 1338+052	0.741310	0.034415
54551	WD 1339-340	1.047129	0.050482
54736	WD 1418-088	3.311311	0.496977
54917	WD 1447-190	3.126079	0.253554
55353	WD 1630+089	1.174898	0.040608
55391	WD 1647-327	1.513561	0.077895
55408	WD 1656-062	1.135011	0.039335
55614	WD 1756+143	1.122018	0.039127
55619	WD 1814+134	0.988553	0.034246
55712	WD 2035-369	3.427678	0.297264
55750	WD 2057-493	1.011579	0.037035
55789	WD 2119+040	1.059254	0.048821
55912	WD 2215+368	0.785236	0.036267
55914	WD 2216-657	3.427678	0.741249
55927	WD 2226-754A	0.794328	0.037991
55928	WD 2226-754B	0.707946	0.034343
56301	WD 2211-392	1.148154	0.086720

Appendix A.3: Habitable Zones in R_{Roche}

Appendix A.3.1: Earth-insolation Distances

Enumeration	Name	Earth-equivalent	Error
189	WD 0651-398A	5.217712	1.620118
190	WD 0651-398B	3.773581	1.223448
194	WD 0708-670	2.721828	0.688128
607	WD 1116-470	3.505748	0.995061
1136	WD 1817-598	4.469061	1.577810
1177	WD 2118-388	3.229917	1.037118
1818	WD 0839-327	11.130616	3.208573
1989	WD 1826-045	9.496364	4.256069
2038	WD 1811+327.2	5.337015	2.599940
2052	WD 1811+327.1	7.345715	3.485631
2114	WD 2316-064	2.346803	0.841408
2129	WD 2107-216	2.689428	0.540836
2155	WD 0651-479	2.263501	0.908525
2466	WD 1503-070	4.640575	1.759758
2505	WD 0213+396	6.040649	1.907550
2605	WD 0008+424	5.376893	0.707057
2678	WD 0243-026	4.170620	0.919147
2679	WD 0326-273	16.225721	6.310409
2680	WD 0548-001	3.391711	0.683227
2681	WD 0728+642	3.227723	0.650808
2690	WD 1829+547	3.103786	0.753143
2696	WD 0038-226	3.142454	0.698874
2701	WD 1821-131	3.866325	1.139187
2706	WD 0659-063	4.439213	1.003937
2708	WD 0000-345	3.521711	0.868128
2711	WD 0053-117	5.436016	1.237539
2712	WD 0141-675	4.490538	1.132505
2715	WD 0322-019	2.668670	0.603368
2718	WD 0423+044	2.085041	0.473359
2721	WD 0511+079	3.422288	0.850582
2723	WD 0644+025	3.027477	0.587470
2727	WD 1036-204	2.352523	0.699476
2730	WD 1444-174	1.707556	0.335249
2731	WD 1733-544	4.016968	0.588527
2745	WD 2105-820	7.707115	2.440979
20281	WD 2253-081	3.715613	1.401185
20549	WD 0011-721	4.762461	1.369837
20614	WD 0752-676	3.506394	0.844195
20619	WD 1241-798	3.683551	1.279232
20626	WD 1708-147	9.888387	3.467768
20637	WD 2359-434	5.243872	1.507514
20754	WD 0117-145	3.423573	0.697791
20761	WD 0851-246	1.433068	0.458634
20793	WD 1008+290	1.705840	0.423282
20841	WD 0856-007	3.067976	0.713035
20865	WD 2028-171	3.424446	0.787064
21072	WD 0025+054	3.519966	0.603847
21391	WD 0136+152	6.040535	1.276341
21553	WD 1242-105	17.448496	4.419093
21851	WD 1743-545	2.238003	0.703644
51479	WD 2159-754	4.680937	1.437823
51895	WD 0123-460	3.260510	1.088123
51964	WD 0148+641	7.544300	2.458416
51971	WD 0150+256	6.977247	2.274353
52130	WD 0233-242	4.636441	1.204998
52141	WD 0236+259	3.341266	0.399199
52414	WD 0344+014	3.155754	0.822706
52585	WD 0655-390	4.215731	1.190877
52799	WD 0802+387	2.291533	0.505947

Enumeration	Name	Earth-equivalent	Error
52842	WD 0810+489	4.194861	1.136862
52880	WD 0821-669	2.445038	0.630862
53297	WD 0928-713	6.755233	1.677657
53654	WD 1033+714	1.936147	0.446459
53855	WD 1124-293	9.335239	3.365709
53920	WD 1136-286	0.751175	0.150511
54218	WD 1237-230	7.582684	2.365607
54530	WD 1338+052	2.277653	0.523223
54551	WD 1339-340	2.949719	0.775100
54736	WD 1418-088	10.894891	4.329767
54917	WD 1447-190	11.720469	3.464585
55353	WD 1630+089	3.894395	0.789509
55391	WD 1647-327	4.366419	1.005827
55408	WD 1656-062	3.084460	0.602513
55614	WD 1756+143	3.184655	0.640297
55619	WD 1814+134	2.949738	0.600006
55712	WD 2035-369	9.393119	3.073431
55750	WD 2057-493	2.757592	0.617664
55789	WD 2119+040	3.232970	0.720851
55912	WD 2215+368	2.282331	0.534759
55914	WD 2216-657	9.393119	4.172428
55927	WD 2226-754A	2.351076	0.634035
55928	WD 2226-754B	2.081613	0.559345
56301	WD 2211-392	2.905539	0.850865

Appendix A.3.2: Inner Boundaries

Enumeration	Name	Leconte et al.	Error
189	WD 0651-398A	4.623667	1.441664
190	WD 0651-398B	3.478475	1.131912
194	WD 0708-670	2.693511	0.682246
607	WD 1116-470	3.329632	0.947943
1136	WD 1817-598	4.437606	1.569401
1177	WD 2118-388	3.175784	1.021186
1818	WD 0839-327	9.008815	2.604897
1989	WD 1826-045	7.676748	3.442358
2038	WD 1811+327.2	4.904983	2.389532
2052	WD 1811+327.1	6.354824	3.015545
2114	WD 2316-064	2.381353	0.853887
2129	WD 2107-216	2.537085	0.510514
2155	WD 0651-479	2.277882	0.914380
2466	WD 1503-070	4.213441	1.597884
2505	WD 0213+396	4.885297	1.543039
2605	WD 0008+424	4.771918	0.628262
2678	WD 0243-026	3.774989	0.832000
2679	WD 0326-273	13.076318	5.089722
2680	WD 0548-001	3.174462	0.640094
2681	WD 0728+642	3.177372	0.640740
2690	WD 1829+547	2.834109	0.687786
2696	WD 0038-226	3.080443	0.686273
2701	WD 1821-131	3.648307	1.077498
2706	WD 0659-063	4.076543	0.922318
2708	WD 0000-345	3.260446	0.805602
2711	WD 0053-117	4.849902	1.104786
2712	WD 0141-675	4.134871	1.046092
2715	WD 0322-019	2.606678	0.589480
2718	WD 0423+044	2.087317	0.474082
2721	WD 0511+079	3.119176	0.775425
2723	WD 0644+025	2.683664	0.521282
2727	WD 1036-204	2.380752	0.715536
2730	WD 1444-174	1.707968	0.335538
2731	WD 1733-544	3.666522	0.546625
2745	WD 2105-820	6.084255	1.932985
20281	WD 2253-081	3.361885	1.267814
20549	WD 0011-721	4.394791	1.267939
20614	WD 0752-676	3.364412	0.811856
20619	WD 1241-798	3.547585	1.234188
20626	WD 1708-147	7.947570	2.811804
20637	WD 2359-434	4.346154	1.252372
20754	WD 0117-145	3.382973	0.689888
20761	WD 0851-246	1.496080	0.479374
20793	WD 1008+290	1.739863	0.437261
20841	WD 0856-007	3.088148	0.718277
20865	WD 2028-171	3.306781	0.760317
21072	WD 0025+054	3.391965	0.582074
21391	WD 0136+152	5.158274	1.090245
21553	WD 1242-105	14.870887	3.767710
21851	WD 1743-545	2.264857	0.713552
51479	WD 2159-754	3.840591	1.181335
51895	WD 0123-460	3.096714	1.035581
51964	WD 0148+641	6.176637	2.012832
51971	WD 0150+256	6.028946	1.965274
52130	WD 0233-242	4.687133	1.218933
52141	WD 0236+259	3.208537	0.383686
52414	WD 0344+014	3.139741	0.818582
52585	WD 0655-390	3.896618	1.104711
52799	WD 0802+387	2.279655	0.503354

Enumeration	Name	Leconte et al.	Error
52842	WD 0810+489	3.798027	1.029415
52880	WD 0821-669	2.414852	0.624806
53297	WD 0928-713	5.631757	1.406857
53654	WD 1033+714	1.948648	0.449429
53855	WD 1124-293	7.484422	2.701935
53920	WD 1136-286	0.761453	0.153262
54218	WD 1237-230	7.322142	2.284375
54530	WD 1338+052	2.347855	0.539524
54551	WD 1339-340	2.888573	0.759993
54736	WD 1418-088	9.392971	3.733204
54917	WD 1447-190	10.345893	3.058883
55353	WD 1630+089	3.741511	0.758528
55391	WD 1647-327	4.077847	0.952846
55408	WD 1656-062	2.964774	0.579199
55614	WD 1756+143	3.099322	0.623339
55619	WD 1814+134	2.947570	0.599624
55712	WD 2035-369	7.452379	2.443072
55750	WD 2057-493	2.687995	0.603080
55789	WD 2119+040	3.210524	0.715863
55912	WD 2215+368	2.322552	0.544238
55914	WD 2216-657	7.421821	3.339499
55927	WD 2226-754A	2.390974	0.645494
55928	WD 2226-754B	2.133691	0.574241
56301	WD 2211-392	2.713515	0.796947

Appendix A.3.3: Outer Boundaries

Enumeration	Name	CO$_2$ Maximum Greenhouse	Error
189	WD 0651-398A	7.898309	2.472101
190	WD 0651-398B	6.021348	1.967259
194	WD 0708-670	4.843049	1.230003
607	WD 1116-470	5.839314	1.668637
1136	WD 1817-598	7.999810	2.836266
1177	WD 2118-388	5.683639	1.831237
1818	WD 0839-327	15.016248	4.346282
1989	WD 1826-045	12.790948	5.736598
2038	WD 1811+327.2	8.481028	4.131760
2052	WD 1811+327.1	10.783172	5.117064
2114	WD 2316-064	4.378891	1.570418
2129	WD 2107-216	4.434973	0.893076
2155	WD 0651-479	4.153843	1.667656
2466	WD 1503-070	7.253494	2.750960
2505	WD 0213+396	8.140974	2.571535
2605	WD 0008+424	8.155203	1.074913
2678	WD 0243-026	6.491805	1.430859
2679	WD 0326-273	21.765774	8.474014
2680	WD 0548-001	5.529489	1.116251
2681	WD 0728+642	5.691191	1.147884
2690	WD 1829+547	4.888688	1.186545
2696	WD 0038-226	5.501580	1.228610
2701	WD 1821-131	6.378261	1.889135
2706	WD 0659-063	7.046451	1.595018
2708	WD 0000-345	5.653562	1.400562
2711	WD 0053-117	8.301709	1.892214
2712	WD 0141-675	7.154609	1.816297
2715	WD 0322-019	4.644471	1.050623
2718	WD 0423+044	3.788305	0.860987
2721	WD 0511+079	5.376874	1.337014
2723	WD 0644+025	4.584768	0.891398
2727	WD 1036-204	4.365401	1.332836
2730	WD 1444-174	3.097536	0.609089
2731	WD 1733-544	6.323675	0.958885
2745	WD 2105-820	10.047261	3.193813
20281	WD 2253-081	5.780666	2.180011
20549	WD 0011-721	7.610720	2.203149
20614	WD 0752-676	5.931558	1.435489
20619	WD 1241-798	6.267370	2.185379
20626	WD 1708-147	13.216823	4.687409
20637	WD 2359-434	7.293763	2.104194
20754	WD 0117-145	6.076069	1.240047
20761	WD 0851-246	2.884422	0.926207
20793	WD 1008+290	3.217974	0.824254
20841	WD 0856-007	5.632579	1.311642
20865	WD 2028-171	5.850756	1.345936
21072	WD 0025+054	5.994360	1.029086
21391	WD 0136+152	8.723339	1.844140
21553	WD 1242-105	25.136100	6.370219
21851	WD 1743-545	4.152895	1.312578
51479	WD 2159-754	6.427607	1.978246
51895	WD 0123-460	5.430836	1.820738
51964	WD 0148+641	10.330935	3.366689
51971	WD 0150+256	10.227023	3.333782
52130	WD 0233-242	8.585198	2.234846
52141	WD 0236+259	5.659209	0.677531
52414	WD 0344+014	5.668988	1.478133
52585	WD 0655-390	6.752308	1.921973
52799	WD 0802+387	4.115690	0.908831

Enumeration	Name	CO_2 Maximum Greenhouse	Error
52842	WD 0810+489	6.532062	1.770624
52880	WD 0821-669	4.335680	1.126203
53297	WD 0928-713	9.465843	2.371958
53654	WD 1033+714	3.553810	0.819883
53855	WD 1124-293	12.435853	4.490997
53920	WD 1136-286	1.398646	0.283492
54218	WD 1237-230	12.955216	4.041910
54530	WD 1338+052	4.405340	1.012877
54551	WD 1339-340	5.155393	1.358773
54736	WD 1418-088	15.924080	6.329390
54917	WD 1447-190	17.653216	5.220347
55353	WD 1630+089	6.601023	1.338276
55391	WD 1647-327	7.096395	1.684083
55408	WD 1656-062	5.232012	1.022277
55614	WD 1756+143	5.509416	1.108542
55619	WD 1814+134	5.341185	1.086716
55712	WD 2035-369	12.333105	4.044673
55750	WD 2057-493	4.783038	1.075554
55789	WD 2119+040	5.788148	1.290653
55912	WD 2215+368	4.284295	1.004093
55914	WD 2216-657	12.260918	5.529568
55927	WD 2226-754A	4.407311	1.191906
55928	WD 2226-754B	3.971107	1.071507
56301	WD 2211-392	4.722142	1.391541

Appendix A.3.4: Methane Outer Boundaries

Enumeration	Name	0.1 CH_4/CO_2	Error
189	WD 0651-398A	8.963056	2.932728
190	WD 0651-398B	6.681061	2.266410
194	WD 0708-670	5.043908	1.303500
607	WD 1116-470	6.340964	1.867175
1136	WD 1817-598	8.294491	2.987375
1177	WD 2118-388	5.966503	1.948716
1818	WD 0839-327	17.806945	5.352795
1989	WD 1826-045	15.177741	6.855893
2038	WD 1811+327.2	9.428068	4.594395
2052	WD 1811+327.1	12.383218	5.878908
2114	WD 2316-064	4.384775	1.574031
2129	WD 2107-216	4.841843	0.981544
2155	WD 0651-479	4.221633	1.696291
2466	WD 1503-070	8.122831	3.082939
2505	WD 0213+396	9.657897	3.059782
2605	WD 0008+424	9.247370	1.236156
2678	WD 0243-026	7.282892	1.606237
2679	WD 0326-273	25.869365	10.184220
2680	WD 0548-001	6.072228	1.239008
2681	WD 0728+642	5.966053	1.204901
2690	WD 1829+547	5.456286	1.326122
2696	WD 0038-226	5.795687	1.315990
2701	WD 1821-131	6.961958	2.112363
2706	WD 0659-063	7.837288	1.782829
2708	WD 0000-345	6.255245	1.588396
2711	WD 0053-117	9.387499	2.155344
2712	WD 0141-675	7.943992	2.083741
2715	WD 0322-019	4.912255	1.113641
2718	WD 0423+044	3.882317	0.885960
2721	WD 0511+079	6.007785	1.497894
2723	WD 0644+025	5.201957	1.023584
2727	WD 1036-204	4.393515	1.439295
2730	WD 1444-174	3.178483	0.628615
2731	WD 1733-544	7.059531	1.212147
2745	WD 2105-820	12.081504	3.995454
20281	WD 2253-081	6.486480	2.446705
20549	WD 0011-721	8.438667	2.521219
20614	WD 0752-676	6.385114	1.580655
20619	WD 1241-798	6.723630	2.386087
20626	WD 1708-147	15.731397	6.138914
20637	WD 2359-434	8.547550	2.537848
20754	WD 0117-145	6.339919	1.300697
20761	WD 0851-246	2.637144	0.853549
20793	WD 1008+290	3.188511	0.882649
20841	WD 0856-007	5.722405	1.341877
20865	WD 2028-171	6.260993	1.446155
21072	WD 0025+054	6.427327	1.107115
21391	WD 0136+152	10.079630	2.138896
21553	WD 1242-105	29.070978	7.403296
21851	WD 1743-545	4.179640	1.344223
51479	WD 2159-754	7.569673	2.372338
51895	WD 0123-460	5.897395	2.018960
51964	WD 0148+641	12.179512	3.971509
51971	WD 0150+256	11.751175	3.831513
52130	WD 0233-242	8.657078	2.266129
52141	WD 0236+259	6.087544	0.735639
52414	WD 0344+014	5.861974	1.529368
52585	WD 0655-390	7.478943	2.208557
52799	WD 0802+387	4.256444	0.940430

Enumeration	Name	0.1 CH_4/CO_2	Error
52842	WD 0810+489	7.326844	1.988337
52880	WD 0821-669	4.526753	1.205861
53297	WD 0928-713	11.061905	2.944229
53654	WD 1033+714	3.611192	0.834613
53855	WD 1124-293	14.821786	5.446933
53920	WD 1136-286	1.403284	0.294841
54218	WD 1237-230	13.863597	4.326322
54530	WD 1338+052	4.249891	0.979650
54551	WD 1339-340	5.437237	1.450816
54736	WD 1418-088	18.316925	7.288354
54917	WD 1447-190	20.072736	5.950618
55353	WD 1630+089	7.097510	1.439193
55391	WD 1647-327	7.805037	2.064775
55408	WD 1656-062	5.623104	1.100007
55614	WD 1756+143	5.849849	1.180897
55619	WD 1814+134	5.488740	1.117775
55712	WD 2035-369	14.786388	4.974466
55750	WD 2057-493	5.070039	1.158763
55789	WD 2119+040	6.000583	1.338343
55912	WD 2215+368	4.265623	1.000604
55914	WD 2216-657	14.735518	7.569426
55927	WD 2226-754A	4.393873	1.199253
55928	WD 2226-754B	3.889792	1.062810
56301	WD 2211-392	5.193693	1.577009

Appendix A.4: Methane Extension

Enumeration	Name	Methane Extension %	Error %
189	WD 0651-398A	13.480698	11.519077
190	WD 0651-398B	10.956237	13.015913
194	WD 0708-670	4.147378	6.911060
607	WD 1116-470	8.590921	9.085868
1136	WD 1817-598	3.683598	10.411342
1177	WD 2118-388	4.976809	10.344835
1818	WD 0839-327	18.584519	7.911026
1989	WD 1826-045	18.660016	18.303269
2038	WD 1811+327.2	11.166569	34.545988
2052	WD 1811+327.1	14.838359	33.494574
2114	WD 2316-064	0.134363	16.323218
2129	WD 2107-216	9.174122	5.184588
2155	WD 0651-479	1.631980	14.807417
2466	WD 1503-070	11.985082	20.834981
2505	WD 0213+396	18.633189	9.059987
2605	WD 0008+424	13.392271	1.802486
2678	WD 0243-026	12.185931	6.951583
2679	WD 0326-273	18.853413	16.575395
2680	WD 0548-001	9.815371	5.239754
2681	WD 0728+642	4.829611	5.019395
2690	WD 1829+547	11.610435	6.940783
2696	WD 0038-226	5.345862	5.211000
2701	WD 1821-131	9.151348	9.028263
2706	WD 0659-063	11.223202	6.964555
2708	WD 0000-345	10.642549	7.235457
2711	WD 0053-117	13.079111	7.062535
2712	WD 0141-675	11.033214	7.393242
2715	WD 0322-019	5.765643	6.734505
2718	WD 0423+044	2.481654	6.643472
2721	WD 0511+079	11.733789	8.696024
2723	WD 0644+025	13.461729	5.345820
2727	WD 1036-204	0.644003	8.285137
2730	WD 1444-174	2.613260	5.000581
2731	WD 1733-544	11.636537	2.545311
2745	WD 2105-820	20.246748	9.979743
20281	WD 2253-081	12.209909	20.843900
20549	WD 0011-721	10.878689	9.236814
20614	WD 0752-676	7.646497	7.082022
20619	WD 1241-798	7.279928	12.325489
20626	WD 1708-147	19.025554	17.384074
20637	WD 2359-434	17.189846	7.676023
20754	WD 0117-145	4.342444	5.043782
20761	WD 0851-246	-8.572866	9.575401
20793	WD 1008+290	-0.915556	6.248402
20841	WD 0856-007	1.594759	6.651907
20865	WD 2028-171	7.011700	6.801523
21072	WD 0025+054	7.222902	3.402618
21391	WD 0136+152	15.547848	5.342468
21553	WD 1242-105	15.654287	8.916230
21851	WD 1743-545	0.644003	10.206250
51479	WD 2159-754	17.768132	12.907965
51895	WD 0123-460	8.590921	12.458691
51964	WD 0148+641	17.893610	16.141703
51971	WD 0150+256	14.903183	15.866858
52130	WD 0233-242	0.837255	8.261880
52141	WD 0236+259	7.568814	1.723471
52414	WD 0344+014	3.404240	8.293461
52585	WD 0655-390	10.761281	9.315327
52799	WD 0802+387	3.419936	6.634038

Enumeration	Name	Methane Extension %	Error %
52842	WD 0810+489	12.167397	8.698639
52880	WD 0821-669	4.406976	7.059512
53297	WD 0928-713	16.861273	4.488724
53654	WD 1033+714	1.614644	6.588416
53855	WD 1124-293	19.185919	13.127833
53920	WD 1136-286	0.331602	5.248210
54218	WD 1237-230	7.011700	13.512654
54530	WD 1338+052	-3.528648	6.433079
54551	WD 1339-340	5.466976	6.893340
54736	WD 1418-088	15.026584	22.963650
54917	WD 1447-190	13.705832	12.302856
55353	WD 1630+089	7.521359	5.080751
55391	WD 1647-327	9.985945	6.816981
55408	WD 1656-062	7.474973	5.087952
55614	WD 1756+143	6.179109	5.072588
55619	WD 1814+134	2.762587	4.962835
55712	WD 2035-369	19.891853	13.284609
55750	WD 2057-493	6.000379	5.226153
55789	WD 2119+040	3.670169	6.639281
55912	WD 2215+368	-0.435829	6.510674
55914	WD 2216-657	20.182827	30.463447
55927	WD 2226-754A	-0.304899	6.658171
55928	WD 2226-754B	-2.047662	6.660485
56301	WD 2211-392	9.985945	10.896924

Appendix B: Code

Appendix B.1: Histogram in Introduction

```python
"""Initialisation"""
import matplotlib.pyplot as plt
import pylab
import numpy as np


#Importing Data
radius, year = np.genfromtxt(r"C:\Users\Gebruiker\Desktop\Thesis\Data\exoplanet.csv", delimite

#Configuration and Important Parameters
bins_all = 31
Rjup = 11.2089 #Earth Radii
Gas = 2*0.0892147 #Jupiter Radii
Rock = 1.7*0.0892147

#Lists for each Planet Type
terr = []
giant = []
intermediate = []
unknown = []

#Values for Scaling
x = 30
ux = 0.5*x
mx = 0.8*x
bx = 2*x
plt.figure(figsize=(10, 12))
plt.xticks(fontsize = mx)
plt.yticks(fontsize = mx)

"""Plotting"""

#Sorting the planets
for i in range(len(radius)):
    if radius[i] >= Gas:
        giant.append(year[i])
    elif radius[i] <= Rock:
        terr.append(year[i])
    elif radius[i] <= Gas and radius[i] >= Rock:
        intermediate.append(year[i])
    else:
        unknown.append(year[i])

#Final Configurations and Plotting
bins_all = 31
pylab.xlabel('Year', fontsize = x, labelpad = ux)
pylab.ylabel('Numer of Exoplanets', fontsize = x, labelpad = ux)
pylab.xlim(1989, 2021)
#pylab.ylim(0, 10)
hist = pylab.hist([terr, intermediate, giant, unknown], label = ['Terrestrial', 'Intermediate'
pylab.legend(loc = 'best', fontsize = x)
pylab.show()
```

Appendix B.2: Estimation of Earth-transits within $100\,\text{pc}$

```python
Rsun = 696342e3 #m
AU = 1.495978707e11 #m
```

```python
Rwd = 0.012*Rsun #m

Re = 6.3781e6 #m
a = 1.5e-2*AU #m

prob = ((Rwd + Re)/(a))

N = 2395*prob


print("p_tra = {:}".format(prob))
print("{} transits within 100 pc".format(N))
```

Appendix B.3: Cooling Tracks for $0.6\,\mathrm{M_\odot}$ *and* $0.8\,\mathrm{M_\odot}$ *White Dwarfs*

```python
"""Initialisation"""
import numpy as np
import pandas as pd

#Importing the files
dat6 = pd.read_table(r"C:\Users\Gebruiker\Desktop\Thesis\Data\0.6.txt", delimiter = ' ')
dat8 = pd.read_table(r"C:\Users\Gebruiker\Desktop\Thesis\Data\0.8.txt", delimiter = ' ')

#Magnitude to Luminosity conversion
def Lbol(M):
    Msun = 4.83
    x = Msun - M
    d = 0.4*x
    return (10**d)

#Applying funtions
dat6['t_cool'] = dat6.apply(lambda x: x['Age']/1e9, axis=1) #Gyr
dat8['t_cool'] = dat8.apply(lambda x: x['Age']/1e9, axis=1) #Gyr

dat6['L'] = dat6.apply(lambda x: Lbol(x['Mbol']), axis=1) #Gyr
dat8['L'] = dat8.apply(lambda x: Lbol(x['Mbol']), axis=1) #Gyr

dat6['logL'] = dat6.apply(lambda x: np.log10(x['L']), axis=1)
dat8['logL'] = dat8.apply(lambda x: np.log10(x['L']), axis=1)

dat6['logT'] = dat6.apply(lambda x: np.log10(x['Teff']), axis=1)
dat8['logT'] = dat8.apply(lambda x: np.log10(x['Teff']), axis=1)

"""Plotting"""
%matplotlib inline
import matplotlib.pyplot as plt
from matplotlib import ticker

#Configuration
fig, ax = plt.subplots(1, 2, figsize = (30, 15))
x = 40
ux = 0.5*x
mx = 0.8*x
bx = 2*x

M = 10
xticks = ticker.MaxNLocator(M)
ax[0].xaxis.set_major_locator(xticks)
ax[1].xaxis.set_major_locator(xticks)

ax[0].tick_params(labelsize = mx)
```

```
ax[1].tick_params(labelsize = mx)

#Plotting
ax[0].plot(dat6['t_cool'], dat6['logT'], color = 'red', label = '$0.6 M_\odot$')
ax[0].plot(dat8['t_cool'], dat8['logT'], color = 'green', label = '$0.8 M_\odot$')

ax[1].plot(dat6['t_cool'], dat8['logL'], color = 'red', label = '$0.6 M_\odot$')
ax[1].plot(dat8['t_cool'], dat8['logL'], color = 'green', label = '$0.8 M_\odot$')

ax[0].set_ylabel("log($T_{eff})$ / K", fontsize = x, labelpad = ux)

ax[1].set_ylabel("log($L$) / $L_\odot$", fontsize = x, labelpad = ux)
ax[1].set_xlabel("Cooling Age / Gyr", fontsize = x, labelpad = ux)

ax[0].set_xlim([0, 10])
ax[1].set_xlim([0, 10])

ax[0].set_xlabel("Cooling Age / Gyr", fontsize = x, labelpad = ux)


ax[0].legend(fontsize = x)
ax[1].legend(fontsize = x)

ax[0].grid(linewidth = 2)
ax[1].grid(linewidth = 2)

plt.show()
```

Appendix B.4: [Fe/Mg] in Polluted White Dwarfs

```
#Importing the packages
import pandas as pd
import numpy as np

"""Importing the Data"""
#Reading the file
dat = pd.read_csv(r'C:\Users\Gebruiker\Desktop\Thesis\Data\DZHeComps.csv')


#Only two H-rich WDs had pollution
#Therefore, only He-rich pollted WDs were analysed
#All metal quantities were presented in ratios to He
#Uncertainties for the metal ratios were not available

#Extracting the columns of interest from the file
DZ = dat[['logcahe', 'logmghe', 'logfehe']]
DZ = DZ.convert_objects(convert_numeric = True)

"""Filtering"""
#Converting Logarithmic Values to actual ones
DZ['cahe'] = DZ['logcahe'].map(lambda x: 10**x)
DZ['mghe'] = DZ['logmghe'].map(lambda x: 10**x)
DZ['fehe'] = DZ['logfehe'].map(lambda x: 10**x)

#Dropping the logarithmic values and rows that had NaNs in any of the three entries
DZ = DZ.drop(columns = ['logcahe', 'logmghe', 'logfehe'])
DZ = DZ.dropna(subset = ['cahe', 'mghe', 'fehe'])


"""Calculationg Metal Ratios"""
#Originally, the comparison was intended for [Mg/Ca] and [Fe/Ca] ratios
```

```python
#This was owing to the high frequency of datapoints with Ca in their spectra
DZ['Mg/Ca'] = DZ.apply(lambda x: x['mghe']/x['cahe'], axis = 1)
DZ['Fe/Ca'] = DZ.apply(lambda x: x['fehe']/x['cahe'], axis = 1)

#However, in light of (Jorge, 2020) it was found that [Fe/Mg] was a more useful quantity
#Therefore, the [Fe/Mg] ratios for the polluted WDs were calculating by dividing out Ca
FeMg = DZ.apply(lambda x: x['Fe/Ca']/x['Mg/Ca'], axis = 1)

"""Solar System Values"""
#For a comparison with [Fe/Mg] values in the Solar System
#Mercury was not included as its [Fe/Mg] was vastly greater than those of the pollted WDs


#Earth's values, taken from Allegre, 2001
MgEarth = 15.8
FeEarth = 28.8
Earth = FeEarth/MgEarth

#Mars's values, taken from Taylor, 2013
MgMars = 18.3/1.74
FeMars = 14.4/1.74
Mars = FeMars/MgMars

#The Sun's (photospheric) values, taken from Lodders, 2003
MgSun = 7.50
FeSun = 7.60
Sun = MgSun/FeSun

#Venus's values, taken from Morgan & Anders, 1980
MgVenus = 31.17
FeVenus = 14.54
Venus = MgVenus/FeVenus


"""Plotting the values"""
#Importing the necessary package
%matplotlib inline
import matplotlib.pyplot as plt


#Some values for ticks, labelsizes etc.
x = 30
ux = 0.5*x
mx = 0.8*x
bx = 2*x
g = 0.5*x

#Specifying the figure size
plt.figure(figsize = (20, 10))

#Plotting the pollution data
plt.hist(FeMg, bins = 500, rwidth = 0.9)

#Plotting the Solar System values
plt.vlines(Earth, 0, 60, color = 'g', label = 'Earth')
plt.vlines(Mars, 0, 60, color = 'r' , label = 'Mars')
plt.vlines(Venus, 0, 60, color = 'purple' , label = 'Venus')
plt.vlines(Sun, 0, 60, color = 'black' , label = 'Sun')

#Adjusting the appearance
plt.xlim([0,3])
plt.ylim([0,60])
plt.xlabel('[Fe/Mg]', fontsize = x, labelpad = g)
plt.ylabel('Frequency', fontsize = x, labelpad = g)
```

```
plt.rc('xtick', labelsize = mx)
plt.rc('ytick', labelsize = mx)
plt.legend(fontsize = x)

#Showing the plot
plt.show()
```

Appendix B.5: Habitable Zones

Appendix B.5.1: Initialisation

```
import numpy as np
import pandas as pd
import matplotlib.pyplot as plt

"""Opening File"""
dat = pd.read_csv(r"C:\Users\Gebruiker\Desktop\Thesis\Data\HabZone.csv")
dat.shape

"""Filtering"""
#Climate Models only apply to T < 10 000K
dat = dat[dat['teff'] <= 1e4]

#Converting logarithmic luminosities to actual ones
dat['L'] = dat['logL'].map(lambda x: 10**x)

#Dropping NaNs
dat = dat.dropna(axis = 0)

#Making the masses readable
dat['mass'] = pd.to_numeric(dat['mass'])

"""Constants and Units"""
#Earth's density
rho_e = 5515 #kg m^-3

#Solar Mass
Ms = 1.98847e30 #kg

#Astronomical Unit
AU = 149597870700 #m

"""Functions"""
#Earth-insolation distance
def simp_hab(L):
    #Input units = Lsun
    Seff = 1
    #Output units = AU
    return np.sqrt(L/Seff)

#Habitable Zone distance
def d_hab(L, Te, m):
    #Input Units
        #L = Lsun
        #Te= K
        #m = N/A
    T = Te - 5780
    Ssun, a, b, c, d = m
    Seff = Ssun + a*T + b*(T**2) + c*(T**3) + d*(T**4)
    #Output units = AU
    return np.sqrt(L/Seff)
```

```python
#Radiative Flux (Seff)
def Se(Te, m):
    #Input units:
        #Te = K
        #m = N/A
    T = Te - 5780
    Ssun, a, b, c, d = m
    S_eff = Ssun + a*T + b*(T**2) + c*(T**3) + d*(T**4)
    #Output units = Searth
    return S_eff


#Roche Limit
def Roche(M):
    #Input units = Msun
    Mr = M*Ms
    n = 9*Mr
    d = 4*np.pi*rho_e
    x = (n/d)**(1/3)
    #Output units = AU
    return (x/AU)
```

Appendix B.5.2: Coefficients

```python
"""Coefficients to calculate the outer edge of the Mechane–HZ expansion for host stars Teff =
meth10ppm = [0.341, 5.5923e-5, 1.8197e-9, -1.0257e-12, 2.0424e-17] #10 ppm CH4
meth1pcnt = [0.3248, 3.4781e-9, 3.2218e-9, -1.2967e-12, 1.2453e-16] #1% CH4
methCH4CO2 = [0.3050, 2.2160e-5, 4.1913e-9, - 1.3177e-12, 1.1796e-16] #0.1 CH4/CO2

"""Revised coefficients for the classical HZ (N2–CO2–H20) and the empirical HZ for host stars
leconte = [1.105, 1.1921e-4, 9.5932e-9, -2.6189e-12, 1.3710e-16]
CO2_max = [0.3587, 5.8087e-5, 1.5393e-9, -8.5347e-13, 1.0319e-16]
```

Appendix B.5.3: Habitable Zone Calculations

```python
"""Roche Limits"""
#Calculating the Roche Limits of an Earth–like planet around each White Dwarf
dat['Roche Limits'] = dat.apply(lambda x: Roche(x['mass']), axis = 1)
dat['Roche Limits / $10^{-2}$ AU'] = dat.apply(lambda x: x['Roche Limits']/1e-2, axis = 1)

"""Earth–insolation Distances"""
#In Astronomical Units
dat['Radiative Equilibrium / $10^{-2}$ AU'] = dat.apply(lambda x:
simp_hab(x['L'])/1e-2, axis = 1)

#In terms of the corresponding Roche Limits
dat['Radiative Equilibrium'] = dat.apply(lambda x:  simp_hab(x['L'])/x['Roche Limits'], axis =

"""Classical HZs"""
#Inner Edge
dat['Leconte et al.'] = dat.apply(lambda x: d_hab(x['L'], x['teff'], leconte), axis=1)

#Outer Edge
dat['CO$_2$ Maximum Greenhouse'] = dat.apply(lambda x: d_hab(x['L'], x['teff'], CO2_max), axis

"""Methane Outer Edges"""
#The outer edges of the Habitable Zones when methane is present as a green house gas
#Methane is assumed to have 10% the abundance of CO2
```

```python
dat['0.1 CH$_4$/CO$_2$'] = dat.apply(lambda x: d_hab(x['L'], x['teff'], methCH4CO2), axis=1)
dat['Methane Extension'] = dat.apply(lambda x: x['0.1 CH$_4$/CO$_2$'] - x['CO$_2$ Maximum Gree

"""Creating Copies that will be in 10^-2 Astronomial Units"""
#Inner Edge
dat['Leconte et al. / $10^{-2}$ AU'] = dat.apply(lambda x:  simp_hab(x['L'])/1e-2, axis = 1)

#Classical Outer Edge
dat['CO$_2$ Maximum Greenhouse / $10^{-2}$ AU'] = dat.apply(lambda x:
x['CO$_2$ Maximum Greenhouse']/1e-2, axis = 1)

#Methane Outer Edge
dat['0.1 CH$_4$/CO$_2$ / $10^{-2}$ AU'] = dat.apply(lambda x:  x['0.1 CH$_4$/CO$_2$']/1e-2, a

#Methane Extension
dat['Methane Extension / $10^{-2}$ AU'] = dat.apply(lambda x:  x['Methane Extension']/1e-2, a

"""Normalised Habitable Zones"""
#Habitable Zone Distances for the WDs in terms of their corresponding Roche Limits
dat['Leconte et al.'] = dat.apply(lambda x: x['Leconte et al.']/x['Roche Limits'], axis=1)
dat['CO$_2$ Maximum Greenhouse'] = dat.apply(lambda x: x['CO$_2$ Maximum Greenhouse']/x['Roche
dat['0.1 CH$_4$/CO$_2$'] = dat.apply(lambda x: x['0.1 CH$_4$/CO$_2$']/x['Roche Limits'], axis=
dat['Methane Extension'] = dat.apply(lambda x:  x['Methane Extension']/x['Roche Limits'], axis

"""Methane Extension"""
#Percentage Change of Methane Extension
dat['Methane Extension %'] = dat.apply(lambda x: (x['Methane Extension']/ x['CO$_2$ Maximum G
```

Appendix B.5.4: Error Propagation

```python
"""Habitable Zones"""
#Temperature Uncertainty
errTeff = dat['Dteff']

#Luminosity Uncertainty / lsun
dat['errL'] = dat.apply(lambda x: x['DlogL']*x['L']*2.303, axis = 1)


#Function for Propagation in Effective Flux
def errS(T, Ter, S, m):
    #Unpacking the constants
    Ssun, a, b, c, d = m


    #Each term in Polynomial
    Tc = T - 5780

    T0 = Ssun
    T1 = a*Tc
    T2 = b*Tc**2
    T3 = c*Tc**3
    T4 = d*Tc**4
    polyT = T0 + T1 + T2 + T3 + T4

    #Errors for each term in Polynomial
    Terr1 = 1*(Ter/Tc)
    Terr2 = 2*(Ter/Tc)
    Terr3 = 3*(Ter/Tc)
    Terr4 = 4*(Ter/Tc)

    #Errors in their units
    Tu1 = (Terr1*T1)
```

```
        Tu2 = (Terr2*T2)
        Tu3 = (Terr3*T3)
        Tu4 = (Terr4*T4)


        #Total Error of Effective Flux (4th-order Polynomial)
        Serr = np.sqrt(Tu1**2 + Tu2**2 + Tu3**2 + Tu4**2)
        return Serr

#Calculation for Effective Fluxes
dat['Seff Inner'] = dat.apply(lambda x: Se(x['teff'], leconte), axis = 1)
dat['Seff Outer'] = dat.apply(lambda x: Se(x['teff'], CO2_max), axis = 1)
dat['Seff CH4'] = dat.apply(lambda x: Se(x['teff'], methCH4CO2), axis = 1)


#Calculation for Effective Flux Errors
dat['S Error / Inner'] = dat.apply(lambda x: errS(x['teff'], x['Dteff'], x['Seff Inner'], leco
dat['S Error / Outer'] = dat.apply(lambda x: errS(x['teff'], x['Dteff'], x['Seff Outer'], CO2_
dat['S Error / CH4'] = dat.apply(lambda x: errS(x['teff'], x['Dteff'], x['Seff CH4'], methCH4C


#Propagation in Habitable Zone
def errHZ(L, Ler, S, Ser, HZ):
        #Luminosity Relative Error
        errLum = Ler/L

        #Flux Relative Error
        errSef = Ser/S

        #Luminosity-Flux Quotient
        Arg = L/S

        #Luminosity-Flux Quotient Error
        errArg = Arg*np.sqrt((errLum**2) + (errSef**2))

        #Relative HZ Error
        errPow = 0.5*(errArg/Arg)

        #HZ error in AU
        HZerr = errPow*HZ
        return HZerr #10^-2 AU

#Calculation for Habitable Zone Errors
dat['radeqm error / $10^{-2}$ AU error'] = dat.apply(lambda x: errHZ(x['L'], x['errL'], 1, 0,
dat['Leconte et al. / $10^{-2}$ AU error'] = dat.apply(lambda x: errHZ(x['L'], x['errL'], x['S
dat['CO$_2$ Maximum Greenhouse / $10^{-2}$ AU error'] = dat.apply(lambda x: errHZ(x['L'], x['e
dat['0.1 CH$_4$/CO$_2$ / $10^{-2}$ AU error'] = dat.apply(lambda x: errHZ(x['L'], x['errL'], x

"""Roche Limits"""
errM = dat['Dmass']

#Propagation in Roche Limits
#Constants assumed to have negligible error
def errRoche(M, Mer, R):
        term = (1/3)*(Mer/M)
        RocheErr = R*term
        return RocheErr #AU


dat['Roche Lim Error'] = dat.apply(lambda x: errRoche(x['mass'], x['Dmass'], x['Roche Limits /

"""Habitable Zones Normalised"""
```

```python
#Propagation in normalising HZs
def errNorm(HZ, dHZ, R, dR, nHZ):
    HZterm = (dHZ/HZ)
    Roterm = (dR/R)
    sumterm = np.sqrt(HZterm + Roterm)
    return nHZ*(sumterm)

dat['radeqm error'] = dat.apply(lambda x: errNorm(x['Radiative Equilibrium / $10^{-2}$ AU'], x
dat['Leconte et al. error'] = dat.apply(lambda x: errNorm(x['Leconte et al. / $10^{-2}$ AU'],
dat['CO$_2$ Maximum Greenhouse error'] = dat.apply(lambda x: errNorm(x['CO$_2$ Maximum Greenho
dat['0.1 CH$_4$/CO$_2$ error'] = dat.apply(lambda x: errNorm(x['0.1 CH$_4$/CO$_2$ / $10^{-2}$


"""Methane Extension Error"""
def errMeth(MZ, dMZ, CZ, dCZ):
    diffval = (MZ - CZ)
    differr = np.sqrt(dCZ**2 + dMZ**2)

    diffrac = (diffval/CZ)

    relCZ = dCZ/CZ
    reldiff = differr/diffval

    frac = np.sqrt((reldiff)**2 + (relCZ)**2)
    perc = abs(diffrac*frac*100)
    return perc

dat['Methane Extension Error %'] = dat.apply(lambda x: errMeth(x['0.1 CH$_4$/CO$_2$ / $10^{-2}
```

Appendix B.5.5: Generating LaTeX Tables of Errors

```python
#Errors for Roche Limits
print(dat[['wdname', 'Roche Limits / $10^{-2}$ AU', 'Roche Lim Error']].to_latex(index = True)


#Errors for Habitable Zones in 10^-2 AU
print(dat[['wdname', 'Radiative Equilibrium / $10^{-2}$ AU', 'radeqm error / $10^{-2}$ AU erro
print(dat[['wdname', 'Leconte et al. / $10^{-2}$ AU', 'Leconte et al. / $10^{-2}$ AU error']].
print(dat[['wdname', 'CO$_2$ Maximum Greenhouse / $10^{-2}$ AU', 'CO$_2$ Maximum Greenhouse /
print(dat[['wdname', '0.1 CH$_4$/CO$_2$ / $10^{-2}$ AU', '0.1 CH$_4$/CO$_2$ / $10^{-2}$ AU err


#Errors for Habitable Zones normalised to Roche Limits
print(dat[['wdname', 'Radiative Equilibrium', 'radeqm error']].to_latex(index = True))
print(dat[['wdname', 'Leconte et al.', 'Leconte et al. error']].to_latex(index = True))
print(dat[['wdname', 'CO$_2$ Maximum Greenhouse', 'CO$_2$ Maximum Greenhouse error']].to_latex
print(dat[['wdname', '0.1 CH$_4$/CO$_2$', '0.1 CH$_4$/CO$_2$ error']].to_latex(index = True))

#Errors for Methane Extension (%)
print(dat[['wdname', 'Methane Extension %', 'Methane Extension Error %']].to_latex(index = Tru
```

Appendix B.5.6: Plot of Earth-equivalent Distances

```python
"""Moving Columns into Arrays"""
tcool = dat[['age']]
rad_eqm = dat[['Radiative Equilibrium']]
radeqm_au = dat[['Radiative Equilibrium / $10^{-2}$ AU']]
roche_lims = dat[['Roche Limits / $10^{-2}$ AU']]
```

```
"""Creation of Subplots"""
fig, ax = plt.subplots(1, 2, figsize = (30, 10))

"""Axes"""
#Some Scaling
x = 30
ux = 0.5*x
mx = 0.8*x
bx = 2*x
b = 1.7*x
a = 35

#Labels
ax[0].set_ylabel("Habitable Zone Boundary / $R_{roche}$", labelpad = x, fontsize = 1.2*x)
ax[1].set_ylabel("Habitable Zone Boundary / AU", labelpad = x, fontsize = 1.2*x)

#Tick parameters
from matplotlib import ticker
ax[0].tick_params(labelsize = 1.2*x)
ax[1].tick_params(labelsize = 1.2*x)

M = 10
xticks = ticker.MaxNLocator(M)
ax[0].xaxis.set_major_locator(xticks)
ax[1].xaxis.set_major_locator(xticks)

#Labels
x_coordinates = [0, 10]
y_coordinates = [1, 1]


"""Plotting"""
#In 10^-2 AU
ax[0].scatter(tcool, roche_lims, color = 'red', s = b, label = 'Roche Limit')
ax[0].scatter(tcool, radeqm_au, color = 'green', s = b, label = 'Earth Equivalent')
ax[0].set_xlabel('Cooling Age / Gyr', fontsize = a, labelpad = x*0.5)
ax[0].set_ylabel('Orbital Distance / $10^{-2}$ AU', fontsize = a, labelpad = x*0.5)
ax[0].legend(fontsize = x)
ax[0].grid(linewidth = 2)

#In terms of Roche Limits
ax[1].plot(x_coordinates, y_coordinates, label = 'Exclusion Zone', c = 'red')
ax[1].fill_between(x_coordinates, 0, y_coordinates, color = 'red')
ax[1].scatter(tcool, rad_eqm, label = 'Earth Equivalent', s = b, c = 'green')
ax[1].set_xlim([0, 10])
ax[1].set_ylim([0, 20])
ax[1].set_ylabel('Orbital Distance / $R_{roche}$', fontsize = a, labelpad = x*0.5)
ax[1].set_xlabel('Cooling Age / Gyr', fontsize = a, labelpad = x*0.5)
ax[1].legend(fontsize = x)
ax[1].grid(linewidth = 2)

plt.show()
```

Appendix B.5.7: Plot of Classical Habitable Zones

```
"""Configuration"""
#Renaming and sorting the Zones for the Plot
dat[['Classical Outer Boundaries', 'Classical Inner Boundaries']] = dat[['CO$_2$ Maximum Green
outer_boundaries = dat[['Classical Outer Boundaries']]
inner_boundaries = dat[['Classical Inner Boundaries']]
```

```python
plt.figure(figsize=(20, 10))

#Labels
plt.xlabel("Cooling Age / Gyr", fontsize = x)
plt.ylabel("Orbital Distance / $R_{Roche}$", fontsize = x)

#Ticks
plt.xticks(np.arange(0, 11, step = 1), fontsize = mx)
plt.yticks(fontsize = mx)


#Limits
plt.xlim([0, 10])
plt.ylim([0, 35])

x_coordinates = [0, 10]
y_coordinates = [1, 1]


"""Plotting"""
#Exclusion Zone
plt.plot(x_coordinates, y_coordinates, label = 'Exclusion Zone', color = 'red')
plt.fill_between(x_coordinates, 0, y_coordinates, color = 'red')

#Classical Boundaries
plt.scatter(tcool, outer_boundaries, label = 'Classical Outer Boundaries', color = 'blue', s =
plt.scatter(tcool, rad_eqm, label = 'Earth Equivalent Distances', color = 'green', s = x*1.7)
plt.scatter(tcool, inner_boundaries, label = 'Classical Inner Boundaries', color = 'brown', s

#Legend
plt.legend(fontsize = x)

#Grid
plt.grid(linewidth = 2)

#Show
plt.show()
```

Appendix B.5.8: Plot to compare with Methane Boundaries

```python
"""Configuration"""
#Renaming and sorting the Zones for the Plot
methane_extensions = dat[['Methane Extension %']]

plt.figure(figsize=(20, 10))

#Labels
plt.xlabel("Cooling Age / Gyr", fontsize = x)
plt.ylabel("Outer HZ Boundary Change / %", fontsize = x)

#Ticks
plt.xticks(np.arange(0, 11, step = 1), fontsize = mx)
plt.yticks(fontsize = mx)

#Limits
plt.plot()


"""Plotting"""
plt.scatter(tcool, methane_extensions, label = 'Methane Extension', color = 'black', s = x*1.7

x_coordinates = [0, 10]
```

```python
y_coordinates = [0, 0]

plt.plot(x_coordinates, y_coordinates, label = 'Classical Outer Boundary', color = 'blue')
plt.xlim([0, 10])
plt.ylim([-10, 25])

#Legend
plt.legend(fontsize = x)

#Grid
plt.grid(linewidth = 2)

#Show
plt.show()
```

Appendix B.5.9: Plot of the Methane Extension

```python
"""Configuration"""
#Renaming and sorting the Zones for the Plot
methane_extensions = dat[['Methane Extension %']]

plt.figure(figsize=(20, 10))

#Labels
plt.xlabel("Cooling Age / Gyr", fontsize = x)
plt.ylabel("Outer Boundary Change / %", fontsize = x)

#Ticks
plt.xticks(np.arange(0, 11, step = 1), fontsize = mx)
plt.yticks(fontsize = mx)

#Limits
plt.plot()




"""Plotting"""
plt.scatter(tcool, methane_extensions, label = 'Methane Extension', color = 'black', s = x*1.7

x_coordinates = [0, 10]
y_coordinates = [0, 0]

plt.plot(x_coordinates, y_coordinates, label = 'Classical Outer Boundary', color = 'blue')
plt.xlim([0, 10])

#Legend
plt.legend(fontsize = x)

#Grid
plt.grid(linewidth = 2)

#Show
plt.show()
```

Appendix B.6: Accretion Model

```python
import numpy as np
import matplotlib.pyplot as plt

"""Semi-major Axis Evolution"""
```

```python
def D(D0, Mi, Mf):
    #D0 = AGB Orbital Distance / AU
    #Mi = Initial AGB Mass / Msun
    #Mf = Final AGB Mass / Msun
    Mrat = Mi/Mf
    return (D0*Mrat) #AU


"""Effective Temperature Evolution"""
def Teff(L, R):
    #Takes Rsun and Lsun as inputs
    r = R*6.957e8 #m
    l = L*3.827e26 #W

    sig = 5.670374419e-7 #Wm^-2 K^-4
    Asig = 4*np.pi*(r**2)*sig
    return (l/Asig)**(1/4) #K


"""Shock Speed"""
def vs(r, Rs):
    #Takes AU and Rsun as input

    #Unit Conversions
    AU = 1.496e8 #km
    Rsun = 696340 #km

    r = r*AU # Converts from AU to km

    vsi = 20 # Initial shock speed in km/s
    rs = 1.2*Rs*Rsun # Typical distance of shock site in km

    #partial result
    rat = (r/rs)**(-0.5)

    return vsi*rat # Shock speed in km/s


"""Temperature Profile"""
def T(r, Rs, T):
    # Typically follows power law
    # Eqn 5.5 Habing & Olofsson, 2003 (Textbook)
    # Takes AU as input

    AU = 1.496e+8 #km
    r = r*AU #Converts from AU to km
    Rsun = 696340 #km

    #Initial Temperature
    T0 = T # Photospheric Temperature  K
    alpha = 0.65

    rs = 1.2*Rs*Rsun # Typical distance of shock site in km

    return T0*((r/rs)**(-0.65))

"""Speed of Sound"""
def cs(T):
    # Assumed to be adiabatic due to low density

    gam = 5/3 # mono-atomic gas adiabatic index
    mu = 1.4 #  typical mean molecular weight

    mp = 1.6726219e-27 #kg
```

```python
    k = 1.38064852e-23  #m^2 kg s^-2 K^-1

    return np.sqrt(gam*(k*T)/(mu*mp))/1e3  #kms^-1


"""Bondi Radius"""
def Rbondi(cs):
    Me = 5.9722e24  # Earth's mass in kg
    G = 6.67408e-11*1e-9  #km^3 kg^-1 s^-2
    return (2*G*Me)/(cs**2)  #km


"""Velocity Function"""
#Unecessary if local speed of sounds exceeds that of accretor
def vo(cs):
    vorb = 10  # typical orbital velocity in km s^-1
    if cs > vo:
        return cs
    else:
        return vorb


"""Gravitational Acceleration"""
def g(M, R):
    Msun = 1.989e30
    Rsun = 696340e3  #m
    yr = 3600*24*365  #s

    G = 6.67408e-11  #m^3 kg^-1 s^-2
    M = M*Msun  #kg
    R = R*Rsun  #m

    gsun = 274  #ms^-2

    g_si = - (G*M)/(R**2)  #m s^-2

    g_fi = g_si/gsun

    return g_fi  #gsun


"""AGB Mass Loss Rate"""
def Magb(Mi, Mf, Lf, Rf):
    #SI units
    Lsun = 3.827e26  #W
    Msun = 1.989e30  #kg
    Rsun = 696340e3  #m
    gsun = 274  #ms^-2
    yr = 3600*24*365  #s

    #Dimensionless Ratio
    Mrat = Mi/Mf

    #Conversions to avoid confusions
    L = Lf*Lsun  #W
    R = Rf*Rsun  #m

    #Surface Gravity / gsun
    g_f = g(Mf, Rf)
    gf = g_f*gsun  #ms^-2

    #Constant
    c = 4e-13
```

```python
    #Preliminary Calculations
    deno = gf*R
    term = L/deno

    #Answers
    ans = (-1)*c*Mrat*term #kg s^-1
    ans_kyr = ans*(3600*24*365) #kg kyr^-1
    ans_fin = ans_kyr/Msun #Msun kyr^-1

    return ans_fin #Msun kyr^-1


"""Mass Accretion Rate"""
def Mbondi(v_shell, v_acc, R_bondi, dM_loss, dist):
    v_acc = 10 # km s^-1
    Ma = dM_loss # Mass loss rate in Msun/kyr
    vs = v_shell # Shock velocity in km/s
    vo = v_acc # Velocity function in km/s
    r = dist # Distance, taking AU as input
    R = R_bondi # Bondi radius in km

    Msun = 1.989e+30 #kg
    Ma = Ma*Msun # Converts from Msun to kg

    #Mass of Earth's Atmosphere
    Matm = 5.136e18 #kg

    AU = 1.496e8 #km
    r = r*AU # Converts from AU to km

    result = ((1/4)*(r**(-2)))*(vs/vo)*(R**2)*(Ma) #kg/s
    result_kyr = result*(3600*24*365*1e3) #kg/kyr
    result_final = result_kyr/Matm #Matm / kyr

    #Convenient Unit Conversion
    #result_tonnes = (result*1e-3)/(3600*24*365*1e3)
    #result_fin = result_tonnes # Earth atmosphere
    return result_final # Jupiter mass / kyr

"""Radial Dependence of Accretion Rate"""
#Distance Grid / AU
r = np.linspace(1, 300, 1000) # Approximately to the orbit of Neptune

#Final Luminosity Values / Lsun
lfG2 = 2665
lfF5 = 4597
lfF1 = 5871
lfA5 = 7750

#Initial Mass (at start of AGB) / Msun
MiG2 = 0.80
MiF5 = 1.17
MiF1 = 1.41
MiA5 = 1.88

#Final Mass (at end of AGB) / Msun
MfG2 = 0.5
MfF5 = 0.65
MfF1 = 0.64
MfA5 = 0.7

#Radii
AU = 215.032 # Converstion to Rsun
```

```python
Rf = AU # Final Radius / Rsun

Rvals = np.linspace(Rf, Rf, 1000)

#Calculations for Effective Temperatures / K
Teff_fG2 = Teff(lfG2, Rf)
Teff_fF5 = Teff(lfF5, Rf)
Teff_fF1 = Teff(lfF1, Rf)
Teff_fA5 = Teff(lfA5, Rf)


#Calculation for Shock Speeds (same for all) / kms^-1
vsh = vs(r, Rf)

#Calculations of Temperature Profiles / K
TfG2 = T(r, Rf, Teff_fG2)
TfF5 = T(r, Rf, Teff_fF5)
TfF1 = T(r, Rf, Teff_fF1)
TfA5 = T(r, Rf, Teff_fA5)

#Calculations of Sound Speeds / kms^-1
csG2 = cs(TfG2)
csF5 = cs(TfF5)
csF1 = cs(TfF1)
csA5 = cs(TfA5)


#Calculation of Bondi Radii / km
RbG2 = Rbondi(csG2)
RbF5 = Rbondi(csF5)
RbF1 = Rbondi(csF1)
RbA5 = Rbondi(csA5)

#Calculation of Gravitational Accelerations / Rsun s^-2
gfG2 = g(MfG2, Rf)
gfF5 = g(MfG2, Rf)
gfF1 = g(MfG2, Rf)
gfA5 = g(MfG2, Rf)

#Calculation of Mass Loss Rates / Msun kyr^-1
MagbG2 = Magb(MiG2, MfG2, lfG2, Rf)
MagbF5 = Magb(MiF5, MfF5, lfF5, Rf)
MagbF1 = Magb(MiF1, MfF1, lfF1, Rf)
MagbA5 = Magb(MiA5, MfA5, lfA5, Rf)

#Approximate Orbital Speed of a planet
#Use if greater than local sound speed
vp = 10 #km s^-1

#Calculation of Accretion Rates / Matm kyr^-1
MbondiG2 = Mbondi(vsh, vp, RbG2, MagbG2, r)
MbondiF5 = Mbondi(vsh, vp, RbF5, MagbF5, r)
MbondiF1 = Mbondi(vsh, vp, RbF1, MagbF1, r)
MbondiA5 = Mbondi(vsh, vp, RbA5, MagbA5, r)


"""Plotting"""
#Configuration Parameters
x = 30
ux = 0.5*x
mx = 0.8*x
bx = 2*x
plt.figure(figsize=(20, 10))
```

```python
#Labels
plt.xlabel("Orbital Distance / AU", fontsize = 0.9*x, labelpad = 15)
plt.ylabel("Mass Accretion Rate / M$_{\oplus, atm}$ $kyr^{-1}$", fontsize = 0.9*x, labelpad =

#Ticks
plt.xticks(fontsize = mx)
plt.yticks(fontsize = mx)

#Commands for Plotting
plt.plot(r, MbondiG2, label = 'G2', color = 'red')
plt.plot(r, MbondiF5, label = 'F5', color = 'orange')
plt.plot(r, MbondiF1, label = 'F1', color = 'green')
plt.plot(r, MbondiA5, label = 'A5', color = 'blue')

#Appropriate Limits
plt.xlim([1, 10])
#plt.ylim([0, 30])

#Legend
plt.legend(fontsize = x)

#Grid
plt.grid(linewidth = 2)

#Show
plt.show()


"""Number of Timesteps"""
N1 = 1e4 #kyr
N2 = 2e4 #kyr

"""Time Values"""
Gyr = 1e6 #kyr

tiG2 = 12.67*Gyr #kyr
tiF5 = 5*Gyr #kyr
tiF1 = 3.18*Gyr #kyr
tiA5 = 1.63*Gyr #kyr

tfG2 = 12.69*Gyr #kyr
tfF5 = 5.01*Gyr #kyr
tfF1 = 3.2*Gyr #kyr
tfA5 = 1.65*Gyr #kyr


tG2 = np.linspace(tiG2, tfG2, N2) #Each step is 1 kyr
tF5 = np.linspace(tiF5, tfF5, N1) #Each step is 1 kyr
tF1 = np.linspace(tiF1, tfF1, N2) #Each step is 1 kyr
tA5 = np.linspace(tiA5, tfA5, N2) #Each Step is 1 kyr


"""Luminosity Values"""
ls = 1000 #number of luminosity values

#Iniital Values / lsun
liG2 = 50
liF5 = 61
liF1 = 69
liA5 = 65

#Final Values / Lsun
lfG2 = 2665
lfF5 = 4597
```

```python
    lfF1 = 5871
    lfA5 = 7750


    lG2 = np.linspace(liG2, lfG2, N2)
    lF5 = np.linspace(liF5, lfF5, N1)
    lF1 = np.linspace(liF1, lfF1, N2)
    lA5 = np.linspace(liA5, lfA5, N2)

    """Radius Values"""
    AU = 215.032 #Rsun

    Ri = 0.8e-1

    Rvals1 = np.linspace(Ri, 1, N1)*AU #Rsun
    Rvals2 = np.linspace(Ri, 1, N2)*AU #Rsun



    """Mass Grids"""
    #Initial Mass (at start of AGB) / Msun
    MiG2 = 0.80
    MiF5 = 1.17
    MiF1 = 1.41
    MiA5 = 1.88

    #Final Mass (at end of AGB) / Msun
    MfG2 = 0.5
    MfF5 = 0.65
    MfF1 = 0.64
    MfA5 = 0.7


    #Stellar Mass
    Mstep = 1e3

    MG2 = np.linspace(MiG2, MfG2, N2)
    MF5 = np.linspace(MiF5, MfF5, N1)
    MF1 = np.linspace(MiF1, MfF1, N2)
    MA5 = np.linspace(MiA5, MfA5, N2)

    """Temperature Values"""
    TG2 = Teff(lG2, Rvals2)
    TF5 = Teff(lF5, Rvals1)
    TF1 = Teff(lF1, Rvals2)
    TA5 = Teff(lA5, Rvals2)




    """Saturn Equivalent Orbital Distances / AU"""
    #Start of AGB / AU
    SiG2 = 11.86
    SiF5 = 20.41
    SiF1 = 26.79
    SiA5 = 43.01

    #Orbital Distance Grid / AU
    SG2 = D(SiG2, MiG2, MG2)
    SF5 = D(SiF5, MiF5, MF5)
    SF1 = D(SiF1, MiF1, MF1)
    SA5 = D(SiA5, MiA5, MA5)


    """Kupiter Equivalent Orbital Distances / AU"""
```

```
#Main Sequence / AU
KsG2 = 30
KsF5 = 57.9
KsF1 = 79
KsA5 = 133.56

#Start of AGB / AU
KiG2 = 37.4
KiF5 = 64.29
KiF1 = 84.318
KiA5 = 135.292

#End of AGB / AU
KfG2 = 110.2
KfF5 = 115.7
KfF1 = 185.7
KfA5 = 361.59

#Orbital Distance Grid / AU
KG2 = D(KiG2, MiG2, MG2)
KF5 = D(KiF5, MiF5, MF5)
KF1 = D(KiF1, MiF1, MF1)
KA5 = D(KiA5, MiA5, MA5)


"""Mass Loss Rates"""
MlG2 = Magb(MiG2, MG2, liG2, Ri)
MlF5 = Magb(MiF5, MF5, liF5, Ri)
MlF1 = Magb(MiF1, MF1, liF1, Ri)
MlA5 = Magb(MiA5, MA5, liA5, Ri)


"""Saturnian Calculations"""
#Shock Speeds / km s^-1
SvG2 = vs(SG2, Rvals2)
SvF5 = vs(SF5, Rvals1)
SvF1 = vs(SF1, Rvals2)
SvA5 = vs(SA5, Rvals2)

#Tmperature Profie / K
STG2 = T(SG2, Rvals2, TG2)
STF5 = T(SF5, Rvals1, TF5)
STF1 = T(SF1, Rvals2, TF1)
STA5 = T(SA5, Rvals2, TA5)

#Sound Speeds / km s^-1
ScsG2 = cs(STG2)
ScsF5 = cs(STF5)
ScsF1 = cs(STF1)
ScsA5 = cs(STA5)

#Bondi Radii
SRG2 = Rbondi(ScsG2)
SRF5 = Rbondi(ScsF5)
SRF1 = Rbondi(ScsF1)
SRA5 = Rbondi(ScsA5)


"""Kuiper Belt Calculations"""
#Shock Speeds / km s^-1
KvG2 = vs(KG2, Rvals2)
KvF5 = vs(KF5, Rvals1)
KvF1 = vs(KF1, Rvals2)
```

```python
KvA5 = vs(KA5, Rvals2)

#Tmperature Profie / K
KTG2 = T(KG2, Rvals2, TG2)
KTF5 = T(KF5, Rvals1, TF5)
KTF1 = T(KF1, Rvals2, TF1)
KTA5 = T(KA5, Rvals2, TA5)

#Sound Speeds / km s^-1
KcsG2 = cs(KTG2)
KcsF5 = cs(KTF5)
KcsF1 = cs(KTF1)
KcsA5 = cs(KTA5)

#Bondi Radii
KRG2 = Rbondi(KcsG2)
KRF5 = Rbondi(KcsF5)
KRF1 = Rbondi(KcsF1)
KRA5 = Rbondi(KcsA5)


"""Mass Loss Rates"""
MlG2 = Magb(MiG2, MG2, liG2, Rvals2)
MlF5 = Magb(MiF5, MF5, liF5, Rvals1)
MlF1 = Magb(MiF1, MF1, liF1, Rvals2)
MlA5 = Magb(MiA5, MA5, liA5, Rvals2)

"""Saturnian Accretion"""
#Accretion Rates
SMbG2 = Mbondi(SvG2, ScsG2, SRG2, MlG2, SG2)
SMbF5 = Mbondi(SvF5, ScsF5, SRF5, MlF5, SF5)
SMbF1 = Mbondi(SvF1, ScsF1, SRF1, MlF1, SF1)
SMbA5 = Mbondi(SvA5, ScsA5, SRA5, MlA5, SA5)

#Total Mass Accretion
SMG2 = (SMbG2).sum()
SMF5 = (SMbF5).sum()
SMF1 = (SMbF1).sum()
SMA5 = (SMbA5).sum()

print("SMG2 = {} Matm".format(SMG2))
print("SMF5 = {} Matm".format(SMF5))
print("SMF1 = {} Matm".format(SMF1))
print("SMA5 = {} Matm".format(SMA5))

"""Kuiper Accretion"""
#Accretion Rates
KMbG2 = Mbondi(KvG2, KcsG2, KRG2, MlG2, KG2)
KMbF5 = Mbondi(KvF5, KcsF5, KRF5, MlF5, KF5)
KMbF1 = Mbondi(KvF1, KcsF1, KRF1, MlF1, KF1)
KMbA5 = Mbondi(KvA5, KcsA5, KRA5, MlA5, KA5)

#Total Mass Accretion
KMG2 = (KMbG2).sum()
KMF5 = (KMbF5).sum()
KMF1 = (KMbF1).sum()
KMA5 = (KMbA5).sum()

print("")
print("KMG2 = {} Matm,".format(KMG2))
print("KMF5 = {} Matm".format(KMF5))
print("KMF1 = {} Matm".format(KMF1))
print("KMA5 = {} Matm".format(KMA5))
```